

Hexagonal Boron Nitride for Next-Generation Photonics and Electronics

Seokho Moon, Jiye Kim, Jeonghyeon Park, Semi Im, Jawon Kim, Inyong Hwang, and Jong Kyu Kim*

Hexagonal boron nitride (h-BN), an insulating 2D layered material, has recently attracted tremendous interest motivated by the extraordinary properties it shows across the fields of optoelectronics, quantum optics, and electronics, being exotic material platforms for various applications. At an early stage of h-BN research, it is explored as an ideal substrate and insulating layers for other 2D materials due to its atomically flat surface that is free of dangling bonds and charged impurities, and its high thermal conductivity. Recent discoveries of structural and optical properties of h-BN have expanded potential applications into emerging electronics and photonics fields. h-BN shows a very efficient deep-ultraviolet band-edge emission despite its indirect-bandgap nature, as well as stable room-temperature single-photon emission over a wide wavelength range, showing a great potential for next-generation photonics. In addition, h-BN is extensively being adopted as active media for low-energy electronics, including nonvolatile resistive switching memory, radio-frequency devices, and low-dielectric-constant materials for next-generation electronics.

Hexagonal boron nitride (h-BN), a member of 2D materials, has an analogous crystal structure to graphene, yet, is an insulator having an indirect bandgap of ≈ 6 eV.^[16] h-BN has been explored as the “ideal” substrate and excellent encapsulant^[17] for other 2D materials including graphene and transition metal dichalcogenides (TMDs) due to its excellent insulating property, atomically flat surface free of dangling bonds,^[18] and charged impurities, and high thermal conductivity.^[19,20] Encapsulating other 2D materials with h-BN effectively protects them from local electrical and chemical environment, enabling them to manifest their theoretically expected “intrinsic” properties. In addition, h-BN has been utilized as passive components in 2D vdW electronic devices, such as gate dielectrics and tunneling barriers.

Recently, h-BN is attracting intensive research interests, motivated by the variety

of outstanding properties, it shows across the fields of quantum optics,^[21] electronics, and optoelectronics.^[22] For example, despite its indirect-bandgap nature, h-BN showed deep-ultraviolet (DUV) emission with exceptionally high internal quantum efficiency (IQE) comparable to or even higher than single-crystalline direct-bandgap semiconductors. Defects in h-BN are efficient^[21,23] and stable sources for single-photon emission over a wide range of wavelengths, from near-infrared (NIR)^[24] to near-ultraviolet (NUV),^[25] at room temperature. The giant light-matter interaction and strong band-edge absorption offered by h-BN enable the realization of solar-blind DUV photodetection by using h-BN as the active layer where DUV photons are effectively absorbed and create electrical carriers. h-BN has also been adopted as active media for low energy electronic devices, including nonvolatile resistive switching (RS) memory and radio-frequency (RF) devices, in addition to passive components for field-effect transistors (FETs), effective diffusion barriers, and low- k interlayer dielectrics (ILDs).

This article aims to review the most recent discoveries of extraordinary properties of h-BN and advancements in emerging photonic and electronic applications. Although there are several well-written review articles on h-BN,^[26–29] this review article focuses on the most recent theoretical discoveries, such as the stacking sequences of h-BN and related optical properties, and the elucidation on how an indirect-bandgap h-BN exhibits strong emission as efficient as a direct-bandgap

1. Introduction

2D van der Waals (vdW) materials are layered materials, where covalently bonded atomically thin in-plane layers are weakly bound through vdW interactions. Since the advent of graphene,^[1–3] various 2D materials have attracted tremendous attention because of new physical phenomena they show, unprecedented in other conventional materials, being exotic material platforms for numerous applications. Furthermore, 2D materials offer huge flexibility in forming heterostructures with rotational or translational variants,^[4–9] giving rise to new electronic and photonic phenomena,^[10–12] for example, layer-number-dependent electronic structures^[13] and flat-band correlations,^[14] through diverse interlayer couplings.^[15] This gives a great potential for creating artificial 2D solids with new functionalities on demand, especially in the fields of photonics and electronics.

S. Moon, J. Kim, J. Park, S. Im, J. Kim, I. Hwang, J. K. Kim
 Department of Materials Science and Engineering
 Pohang University of Science and Technology (POSTECH)
 77 Cheongam-ro, Nam-gu, Pohang 37673, Republic of Korea
 E-mail: kimjk@postech.ac.kr

The ORCID identification number(s) for the author(s) of this article can be found under <https://doi.org/10.1002/adma.202204161>.

DOI: [10.1002/adma.202204161](https://doi.org/10.1002/adma.202204161)

semiconductor does. In Section 2, newly discovered structural, optical, and electrical properties, including the stacking sequences of h-BN and corresponding optical properties, and the combination of theory and experimental evidence elucidating the unique light absorption and emission properties, are discussed. Then, recent advancements in h-BN applications are discussed with special emphases on DUV light emitters, single-photon emitters (SPEs), and DUV photodetectors as next-generation photonics applications. For next-generation electronics applications, recent results on RS memory and RF devices in which h-BN layers are used as active components, as well as remarkable advancements in conventional applications such as dielectrics for FET, effective diffusion barrier, and low- k ILD are discussed.

2. Properties of h-BN

2.1. Structural Properties

Boron nitride (BN) is a crystalline material consisting of a 1:1 stoichiometry of two elements, boron (B) and nitrogen (N) atoms. Various forms of bulk BN have been used for diverse applications, including high-temperature insulators, lubricants, adhesives, and corrosion-resistant paints because of the thermal and chemical stability of h-BN. There are three crystalline forms of BN, cubic boron nitride (c-BN), wurtzite boron nitride (w-BN), and hexagonal boron nitride (h-BN) (Figure 1). c-BN has a zinc blende lattice with tetrahedral structure through sp^3 hybridization of B and N atoms. c-BN is one of the hardest materials exhibiting very high thermal conductivity, hardness, and chemical inertness. w-BN is another sp^3 -hybridized phase of BN, where B and N atoms are tetrahedrally coordinated, consisting of alternating close-packed all-B and all-N layers

(aa'bb'aa').^[30] Both c-BN and w-BN have been usually synthesized by compressing h-BN at high static pressures that cause a deformation of the hexagonal lattice of h-BN and hybridization change from sp^2 to sp^3 .^[31] Whereas w-BN is usually transformed by the application of a compressive pressure above 13.0 GPa at room temperature,^[32] the c-BN can be achieved by high static compressive pressures (11–12 GPa) at very high temperatures (3000–4000 K).^[31] Although the stability of the w-BN is still under debate, the possibility of stable and nonreversible phase transformation of h-BN into w-BN has been suggested.^[33,34]

h-BN consists of B and N atoms arranged in an sp^2 -hybridized honeycomb layered structure, isostructural to graphene. Each adjacent layer consists of highly polarized B–N covalent bonds along with the layer and is held together by weak vdW interactions. The length of the B–N bond in h-BN is 0.145 nm, and the interlayer distance between two adjacent layers is 0.334 nm.^[35] Considering the layered structure of h-BN, there are several polytypes with high-symmetry stacking sequences where consecutive layers are rotated or translated (Figure 2). The h-BN with AA stacking sequence consists of the monolayers periodically aligned without translation or rotation along the c -axis. In the AA' stacking sequence, the adjacent layers in the AA stacking sequence are aligned in a way that B and N atoms alternate along the c -axis. In the AB or Bernal stacking, isostructural to graphite, one layer in the AA stacking sequence is shifted by the interatomic distance of ≈ 0.145 nm such that half of the B atoms are aligned with half of the N atoms of adjacent layers, and the remaining half of the atoms are aligned with the empty hexagon centers in the adjacent layers.^[36] In addition to AA, AA', and AB stacking sequences, there is a rhombohedral BN (r-BN) structure where each next basal plane is successively translated in the [1100] orientation by 0.145 nm.^[37] Unlike graphene or graphite consisting of one element, carbon, h-BN is strongly polarized with electronegativity

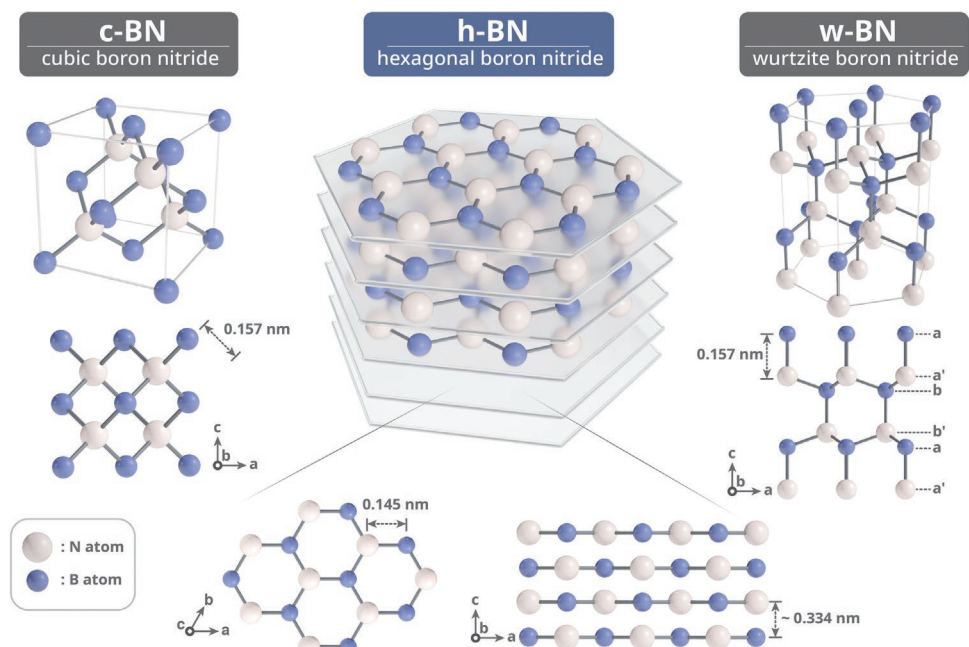


Figure 1. Schematic illustration of the crystal structure of c-BN, h-BN, and w-BN.

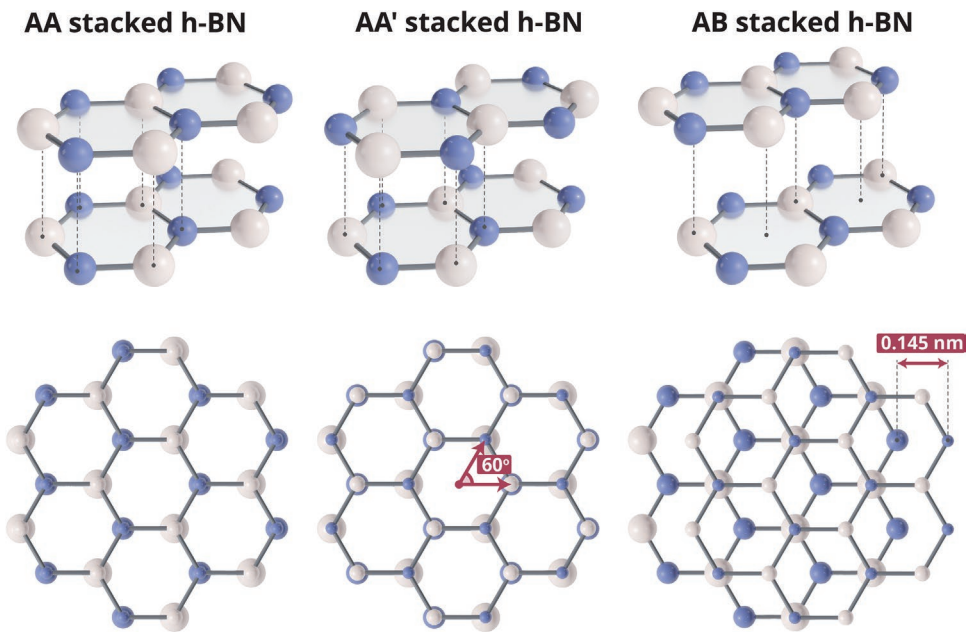


Figure 2. Schematics of the structural polytypes of h-BN.

differences between the B and N atoms giving rise to in-plane anisotropic properties, as well as unique electronic and optical properties depending on its stacking sequences.

Among the polytypes, h-BN with AA' stacking sequence has been employed as a promising wide-bandgap semiconductor for DUV emitters, DUV photodetectors, and photonic devices with strong single-photon emission and as an insulator for gate dielectrics, passivation layers, and atomic tunneling layers, due to its thermodynamical stability compared to other polytypes.^[36] Besides the crystalline forms of BN and the stacking sequences of h-BN, BN with noncrystalline structure, amorphous BN, has been synthesized for an ultralow dielectric constant (low- k) material with an excellent diffusion barrier property for high-performance CMOS-compatible logic and memory devices.^[38]

2.2. Optical Properties

Recently, h-BN has attracted increasing attention as active optical materials for stable quantum emitters in visible spectral ranges,^[27,39,40] and a new generation of emitters and detectors in DUV spectral ranges due to the strong-coupling regime of the exciton–phonon interaction substantiated by exceptionally high IQE of the band-edge emission.^[27,41,42] Inspired by these promising attributes, a huge effort has been made to explore the fundamental optical properties of h-BN for designed functionalities suitable for practical photonic devices with versatile performances.

2.2.1. Optical Properties of h-BN with Number of Layers

h-BN has a layer-dependent optical bandgap around 6 eV, with an indirect bandgap of 5.95 eV for multilayer and a direct bandgap of 6.1 eV for monolayer. Interestingly, regardless of

the number of layers, h-BN exhibits intense optical signatures in the DUV region such as free exciton recombination (5.7–6.0 eV) and shallow-level defects mediated recombination (\approx 5.5 eV). Besides the band-edge emission, various deep levels contribute to the emission from near-ultraviolet (NUV, 4.1 eV) and visible (2–3 eV) regions. These fascinating optical properties make h-BN an emerging active material for DUV optoelectronics and provide great potential for quantum information and sensing applications.

Similar to TMDs, the conduction band at the M point is very sensitive to the number of layers in h-BN.^[43] While both monolayer and bulk h-BN have the valence band maximum at the K point of the Brillouin zone (BZ), the suppression of the interlayer coupling with decreasing number of layers shifts the conduction band minimum from the M point to the K point in monolayer h-BN, leading to the indirect-to-direct bandgap cross-over (Figure 3a).

Therefore, due to the indirect-bandgap nature of bulk h-BN, radiative recombination of bulk h-BN accompanies the phonon-assisted emissions observed between 5.7 and 5.95 eV, which are redshifted compared to the indirect exciton (iX) energy (Figure 3b). Cassabois et al. corroborated that the degree of redshifts of the phonon-assisted emissions corresponds to the detuning given by the energy of the phonon modes involved in the radiative recombination process.^[16] By simplifying the BZ of h-BN, one-phonon scattering processes in h-BN involve phonons in the middle of the BZ around the T points ($T\bar{T}=MK$). The energy detunings of the five emission lines in the photoluminescence (PL) spectrum with respect to iX are 22, 64, 95, 162, and 188 meV, which are perfectly agreed with the phonon energy in the middle of the BZ around T points for the ZA, TA, LA, TO, and LO modes, respectively.

Because of the mirror symmetry between absorption and emission assisted by phonon emission in the optical response of indirect semiconductors,^[48] the Stokes shift is observed both

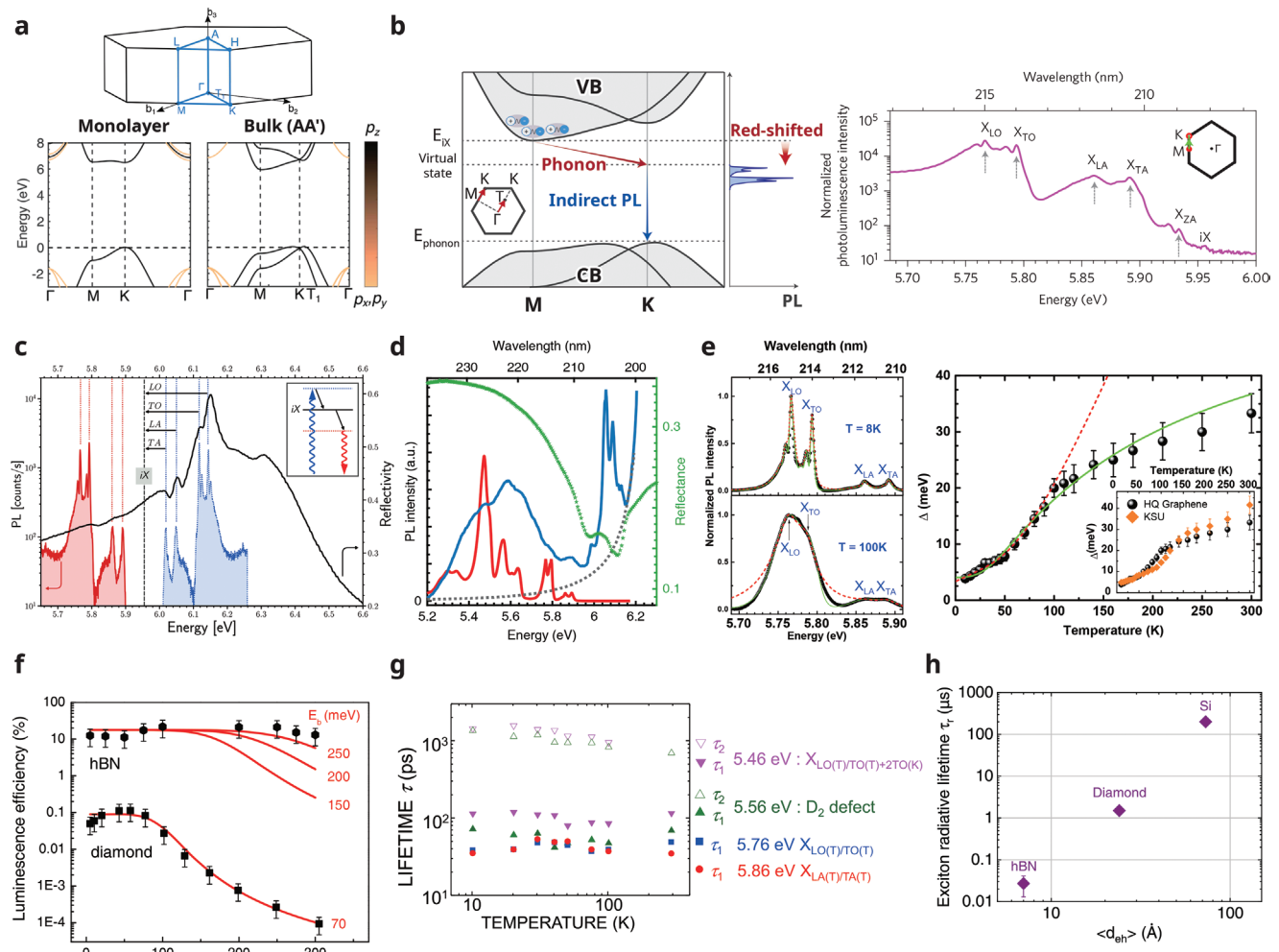


Figure 3. a) Brillouin zone (BZ) of bulk h-BN and the band structure of h-BN in the AA' stacking sequence for bulk and monolayer. The color of each electronic band indicates the p_{xy} and the p_z character of the states corresponds to the color bar. Adapted with permission.^[43] Copyright 2018, American Chemical Society. b) Schematic of indirect decay channels for excitons in h-BN and corresponding phonon modes. The green arrow indicates the phonon scattering path in the 1st BZ. Reproduced with permission.^[16] Copyright 2016, Springer Nature. c) Comparison between PL (red) and reflectivity (black) of bulk h-BN at 8 K. The blue spectrum is the PL spectrum flipped against the energy of the iX. Adapted with permission.^[44] Copyright 2021, American Physical Society. d) 10 K PL spectrum (blue solid line) and reflectance spectrum (green symbols) of monolayer h-BN epitaxially grown on graphite. Adapted under the terms of the CC-BY Creative Commons Attribution 4.0 International license (<https://creativecommons.org/licenses/by/4.0/>).^[45] Copyright 2019, The Authors, published by Springer Nature. e) PL spectrum in h-BN in the DUV at 8 and 100 K (left) and the temperature-dependent full width at half maximum (FWHM) Δ of the phonon replicas (right). Experimental data (black symbols) are theoretically fit with the gaussian line, which means the strong-coupling regime of phonon-exciton (green solid), or with a lorentzian line, which means the weak-coupling regime of phonon-exciton (dashed red). The comparison of several h-BN samples is in the inset. Adapted with permission.^[41] Copyright 2017, American Physical Society. f) Luminescence efficiency of h-BN and diamond from temperature-dependent CL. The red lines correlate to the thermal dissociation of excitons with respect to the temperature. Reproduced with permission.^[42] Copyright 2019, American Physical Society. g) The values of the decay times as a function of temperature extracted from TRCL signals. Reproduced with permission.^[46] Copyright 2018, AIP Publishing. h) Radiative lifetimes of free excitons in h-BN compared to silicon and diamond as a function of the average distance between electron and hole in the indirect exciton. Reproduced with permission.^[47] Copyright 2021, American Physical Society.

in optical absorption and emission. Elias et al. substantiated the resonance between these optical processes in bulk h-BN, by comparing the reflectivity spectrum and the mirrored PL (Figure 3c).^[44] From the PL spectrum of h-BN (red line) and its mirror image with regard to the iX energy (blue line), the lines at 6.02, 6.05, 6.11, and 6.14 eV in the reflectivity spectrum (black line) correspond to the phonon-assisted optical absorption accompanied by TA, LA, TO, and LO phonon emission, respectively. Due to the direct-bandgap nature, the emission and

reflectivity spectra are fully different in monolayer h-BN.^[45,49] Elias et al. investigated that there is no phonon emission between reflectance and PL in monolayer h-BN, whereas the PL spectrum of bulk h-BN shows the phonon-assisted emissions, which substantiate a direct-gap nature of monolayer of h-BN (Figure 3d). In addition, Utilizing complementary experiments using spatially resolved PL imaging in this spectral domain for exfoliated monolayer and adjacent few-layer h-BN, the direct-to-indirect-bandgap cross-over has also been investigated.^[50]

Interestingly, unlike TMDs in which only the monolayer shows a strong PL due to the transition from direct bandgap in monolayer to indirect bandgap in multilayer phase, both monolayer and the multilayer phases, despite the multilayer phase having indirect bandgap, exhibit strong emission. Watanabe et al. reported strong cathodoluminescence (CL) in the DUV spectral range from h-BN crystals, which led to the initial misinterpretation of bulk h-BN as a direct-bandgap material.^[51] The intense band-edge DUV emission of h-BN sparked a long and controversial debate concerning its electronic bandgap structure and excitonic properties.

This puzzle of bright DUV emission in bulk h-BN was resolved by the demonstration of the strong exciton–phonon interaction and the quantitative analysis of the exciton binding energy and recombination dynamics. First, Vuong et al. corroborated the strong exciton–phonon coupling regime of h-BN by using temperature-dependent PL spectroscopy from 4 up to 300 K (Figure 3e).^[41] In the case of the strong exciton–phonon interaction, the excitonic linewidth is affected by the fluctuations of the phonon field during lattice vibrations. Because the amount of the lattice vibration has the square root dependency on the temperature in the exciton–lattice interaction Hamiltonian,^[52] the excitonic line of the material with the strong exciton–phonon interaction is eventually expected to be of a Gaussian shape with a line width Δ increasing as \sqrt{T} . The data fit well by the Gaussian function and the prominent \sqrt{T} dependence of the Δ leads to the strong-coupling regime of the exciton–phonon interaction of h-BN. Second, Schué et al. showed the strong exciton binding energy of bulk h-BN by using temperature-dependent CL from 10 up to 300 K (Figure 3f).^[42] Whereas the diamond with indirect bandgap shows the thermal dissociation of excitons resulting in an abrupt luminescence efficiency drop by three orders of magnitude, the luminescence efficiency of h-BN is almost constant from 10 to 300 K. The estimated exciton binding energy in h-BN is larger than 250 meV, which is superior to that in diamond (70 meV) or AlN (52 meV).^[53] Third, time-resolved cathodoluminescence (TRCL) was used to measure the recombination dynamics.^[46,47,54,55] Chichibu et al. showed the ultrafast decay of the indirect excitons (iXs) and the near-band-edge emission assisted by phonons at the T points of the 1st BZ (TA, LA, TO, LO) on a picosecond time scale (Figure 3g). Also, Roux et al. practically estimated the radiative lifetime of the near-band-edge excitons in h-BN by using TRCL giving a simultaneous measurement of the internal quantum yield (η_i) and the excitonic lifetime (τ) of the near-band-edge phonon-assisted emissions (Figure 3h). Although the high uncertainty of $\approx 50\%$, the radiative lifetime of the near-band-edge emission in h-BN (27 ns) is much shorter than that in other indirect-bandgap materials, such as diamond (1.5 μ s) and Si (200 μ s), which indicates that the nonradiative recombination in h-BN is bypassed by faster radiative recombination. The combination of strong exciton–phonon coupling, high exciton binding energy, and short radiative lifetime of multilayer (bulk) h-BN enables such a strong band-edge emission despite its indirect-bandgap nature, which makes h-BN as a very promising active material in DUV photonic devices with its fascinating optical properties irrespective of its number of layers.

2.2.2. Optical Properties of h-BN with Stacking Sequences

As discussed in Section 2.1, there are h-BN polytypes with high-symmetry stacking sequences, AA, AA', and AB, which lead to different optical properties in h-BN polytypes. To study the optical properties of the polytypes of BN, second-harmonic generation (SHG), which is a useful method of observing the symmetry of surface layers,^[58] has been employed.^[56,59] Bulk h-BN crystals with AA' stacking sequence belong centrosymmetric D_{6h} point group and show a very weak SHG signal. However, few-layer h-BN exhibits different symmetry properties. The AA' h-BN with an even layer number belongs to the centrosymmetric D_{3d} point group, whereas the AA' h-BN with an odd layer number belongs to the noncentrosymmetric D_{3h} point group. Li et al. experimentally probed the difference in symmetry properties of few-layer h-BN and examined the strong enhancement of SHG intensity for odd numbers of layers compared to even layer numbers due to the broken inversion symmetry (Figure 4a).^[56] The SHG intensity of AA' h-BN with even layer numbers is less than 2% of that emitted from the monolayer h-BN. However, the SHG intensity of AA' h-BN with an odd layer number shows very little layer number dependence and is comparable to that of monolayer h-BN, because the SHG signal from the layers underneath the topmost layer cancels out and only top monolayer mainly contributes to the SHG signal.

The other energetically metastable Bernal BN (b-BN) with AB stacking sequence shows a high SHG signal due to the broken inversion symmetry (Figure 4b).^[27,59] Kim et al. exhibit the SHG signal increased by four times in bilayer b-BN compared to that of monolayer h-BN due to the constructive interference of the coherent signals from both layers of the b-BN bilayer. While the b-BN bilayer shows a strong SHG signal, the signal is very small for the bilayer h-BN with AA stacking sequence due to the destructive interference of the signals from both bilayers with inversion symmetry. Yao et al. also substantiated the strong dipole-allowed SHG signals from the h-BN with AB stacking sequence through the generation of AB interfacial layer created by twisting h-BN (Figure 4c).^[5] They fabricated two homostructures of h-BN with 384 layers by breaking a single h-BN flake with 192 layers and subsequently stacking to create AA' homostructures without sample rotation or AB homostructures with rotating selected pieces by 60°. The AB homostructure exhibits improved SHG signals due to the broken inversion symmetry compared to the AA' homostructure despite having the same layer thickness. Furthermore, as shown in Figure 4d, they fabricated the vertical superlattice structure with multiple AB interfaces between h-BN multilayers and showed the SHG signals increase superlinearly with the number of AB interfaces, because the amplitudes of SHG field from multiple AB interfaces are overlapped.

Besides the nonlinear optics, h-BN with AA' or AB stacking sequence has different bandgap-related optoelectronic properties because the different stacking sequence of the successive layers influences the electronic band structure. Although the h-BN with the AA' stack sequence has been widely studied, little is known about the optoelectric properties associated with the bandgap of the h-BN with the AB stack sequence. However, thanks to the recent achievements in the development of spatially resolved and confocal hyperspectral PL imaging in

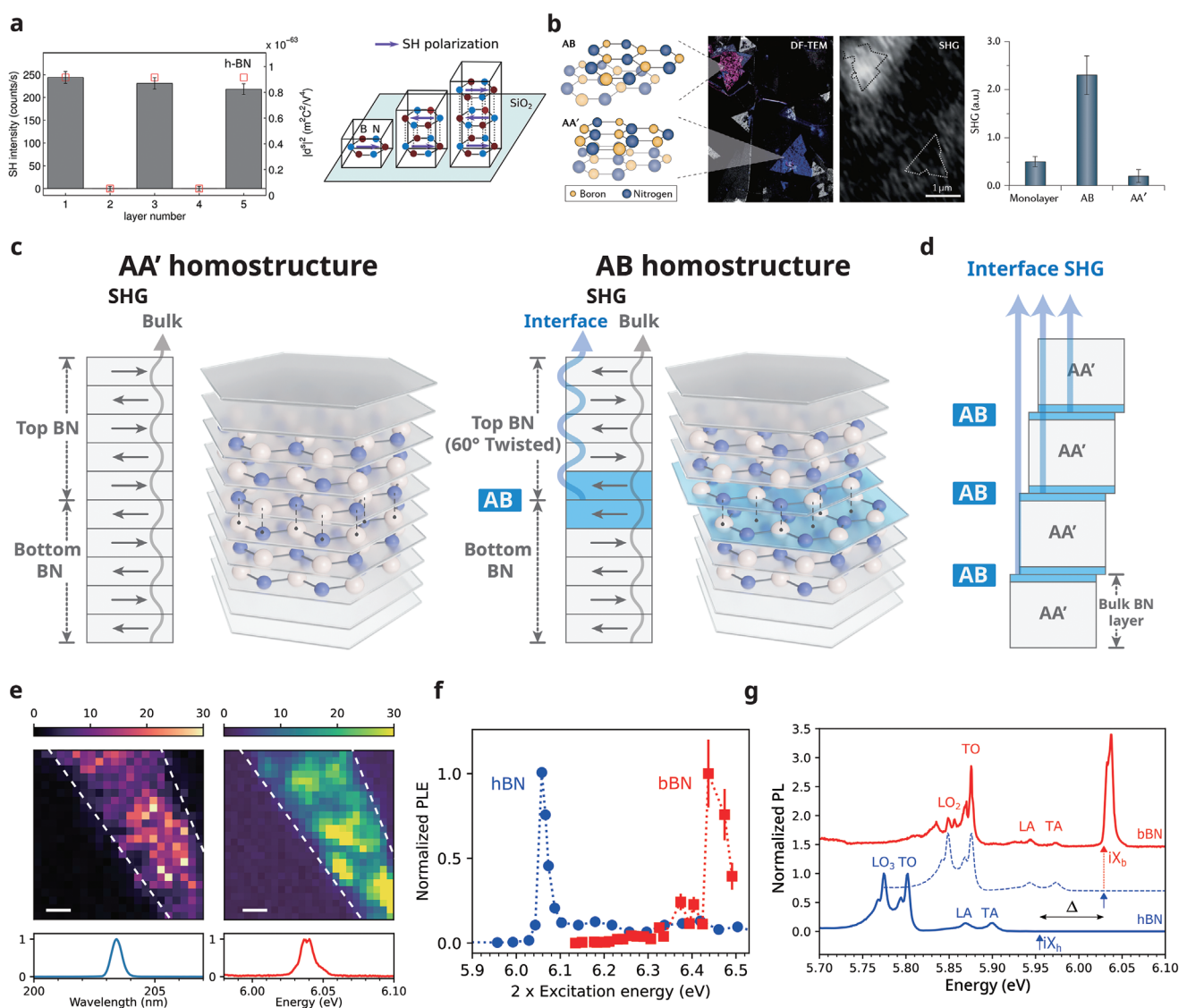


Figure 4. a) The layer-dependent SHG intensities and nonlinear susceptibility for few-layer h-BN. Left: The histogram of the experimental SH intensities and the red squares are the results of a theoretical model. Right: Schematic of the alternating orientation of successive layers in h-BN with AA' stacking sequences. Reproduced with permission.^[56] Copyright 2013, American Chemical Society. b) Dark-field transmission electron microscopy (DF-TEM) images of two different bilayer h-BN with AA' (blue) and AB (pink) stacking sequences and the intensity map of the SHG signals. The histogram shows averaged SHG intensities measured from monolayer, bilayer with AB or AA' stacking sequences. Reproduced with permission.^[27] Copyright 2019, Springer Nature. c) Schematic of a BN homostructure with an AA' or AB stacking sequences by twisting upper BN to 60°. d) SHG intensity improvement in BN vertical superlattices with schematic. e) SHG and PL images at 6 K: the SHG intensity map at ≈203.2 nm and normalized SHG spectrum. (Left) The PL intensity map at ≈6.035 eV and normalized PL spectrum. (Right) Scale bar = 1 μm. f) Two-photon excitation spectroscopy in b-BN (red) (≈6.035 eV emission energy) and in h-BN (blue) (≈5.8 eV emission energy). g) 6 K PL spectra in b-BN (top, red) and h-BN (bottom, blue). PL spectrum of h-BN is blueshifted (the dotted blue line) for comparison. $\Delta = 74$ meV. c–f) Reproduced with permission.^[57] Copyright 2022, American Chemical Society.

this spectral domain, stacking sequence-dependent optoelectronic properties of h-BN in DUV spectral ranges have been systematically investigated (Figure 4e–g). Rousseau et al. verified the small direct-bandgap transition of b-BN crystals by correlating experimental results including broken inversion symmetry observed by SHG and the strong emission line at ≈6.035 eV (Figure 4e).^[57] In addition, the two-photon photoluminescence excitation spectrum shows a coherent phase of the b-BN crystals with negligible ≈6.06 eV resonance of h-BN

(Figure 4f). Compared to the PL spectra of h-BN, b-BN shows a strong emission line at ≈6.035 eV with a 74 meV blueshifted phonon-assisted lines of h-BN with regard to the indirect exciton of b-BN (iX_b) at 6.029 eV (Figure 4g). Therefore, the iX_b is almost resonant with the ≈6.035 eV transition, which was contributed by the recombination of the direct exciton (dX_b) in b-BN. In other words, indirect and direct excitons are quasi-degenerated in b-BN, as predicted by theoretical studies.^[60]

2.3. Electrical and Thermal Properties

From an early stage of research on 2D materials, h-BN has been widely utilized as supportive and passive layers such as “ideal” substrates, dielectrics, and passivation layers for other 2D materials and devices due to its atomically flat, surface free of charged impurities and dangling bonds, outstanding insulating property, and high thermal conductivity. Recently, h-BN has attracted increasing attention owing to substantial advances in emerging electronic applications such as RS memory and RF switch in which h-BN layers are served as highly performing active media. Inspired by these rapid and expansive advances, fundamental electrical and thermal properties of h-BN have been extensively explored. These explorations are important to comprehend the role of h-BN in electronic devices, as well as to develop a new class of next-generation h-BN-based electronic devices.

2.3.1. Dielectric Properties

To realize the potential of h-BN for next-generation electronics, detailed research on the dielectric properties of h-BN has been carried out. h-BN presents an anisotropic dielectric response because of its crystal structure, which consists of strong covalent bonding in the in-plane direction and weak vdW interactions in the out-of-plane direction. Laturia et al. calculated the macroscopic in-plane and out-of-plane dielectric constants of h-BN using density functional theory (DFT) (**Figure 5a**).^[61] The dielectric constant in the out-of-plane ranges from 3.29 to 3.76, increasing with the number of layers, which is much smaller than that in the in-plane direction ranging from 6.82 to 6.93, causing a strong anisotropy in the dielectric response under external electric fields. Anisotropic property has also been observed in the dielectric breakdown of h-BN. For conventional dielectrics, it is empirically known that the dielectric constant is inversely proportional to the dielectric breakdown strength (E_{BD}).^[62,63] h-BN follows this tendency, showing stronger E_{BD} in the out-of-plane direction than the in-plane direction (**Figure 5b**). Hattori et al. measured E_{BD} values in parallel and normal to the *c*-axis ($E_{BD\parallel c}$ and $E_{BD\perp c}$) as 12 and 3 MV cm⁻¹, respectively (**Figure 5b**).^[64] Although this result agrees with the empirical tendency, the aspect of dielectric breakdown of h-BN is likely to be different from that of conventional oxides- and nitrides-based dielectrics. Hattori et al. investigated the breakdown behavior of h-BN by applying electrical stress using a conductive AFM, and h-BN showed a different breakdown behavior compared to conventional dielectrics in two aspects.^[62] First, the h-BN bulk crystal exhibits the layer-by-layer breakdown which involves consecutive physical rupture of individual layers creating a sub-nm hole of h-BN, as schematically described in **Figure 5c**. The layer-by-layer breakdown phenomenon leads to unusual electrical behavior, where the h-BN beneath the hole still contains insulating dielectric behavior with similar current-voltage (*I*-*V*) characteristics in the low-voltage region, and an earlier breakdown compared to the 1st *I*-*V* during hole creation, as shown in **Figure 5d** (red line).

Second, the statistical aspect of h-BN breakdown is different from conventional dielectric materials. The breakdown

mechanism of conventional amorphous oxide-based dielectrics has been described with the percolation model.^[65] According to this model, when the defect density reaches a critical value due to random generation of defects, conductive defect paths can be formed under electrical stress, causing breakdown. As the thickness of the dielectric layer becomes thinner, the probability of forming such a conductive path becomes higher.^[65,66] Thus, in the case of amorphous dielectrics, the random breakdown events can occur even at a relatively low defect density. However, statistical analyses of h-BN breakdown using the Weibull plot indicate different behavior from the conventional percolation model.^[62,66–71] The Weibull plot is the graph of $W \equiv \ln(-\ln(1 - F(V_{BD}))$ versus $\ln(V_{BD})$ where the $F(V_{BD})$ is the cumulative distribution function of the breakdown voltage (V_{BD}) population at a set of different locations.^[72] **Figure 5e** shows the Weibull plots of h-BN layers with different thicknesses (11, 16, and 22 nm). The slope of Weibull plot β is an important parameter for evaluating the degree of variability and reliability. The thinner h-BN (thickness \approx 11 nm) shows the higher β , representing lower variability of breakdown voltage, which is opposite to the tendency of conventional dielectric materials. Recently, Ranjan et al. also demonstrated a similar phenomenon in atomically thin single-crystal h-BN layers with the thicknesses of 3, 3.5, 4, and 8 nm (**Figure 5f**).^[67] The extraordinarily high β indicates that single-crystal h-BN has excellent electrical reliability and low variability.

Moreover, several studies have shown that h-BN has superior breakdown strength and unprecedented reliability even with a sub-nanometer thickness compared to conventional dielectrics. Reported breakdown strength values of h-BN and representative oxide-based dielectrics, silicon dioxide (SiO_2),^[63,73] and hafnium oxide (HfO_2),^[74,75] are summarized in **Table 1**. Ji et al. investigated the breakdown strength of CVD-grown h-BN and showed that even monolayer h-BN exhibits exceptional stability against electrical stress.^[76] Unlike the high-*k* 2 nm-thick HfO_2 showing the random fluctuation of onset voltage involving sudden degradation, the monolayer h-BN exhibits a very low variation of onset voltage and reproducible *I*-*V* characteristics after multiple electrical stresses (**Figure 5g**). Jiang et al. also reported the remarkable breakdown properties in monolayer h-BN compared to SiO_2 , HfO_2 , and Al_2O_3 .^[77] While oxide-based dielectrics exhibit breakdown-induced hillocks due to the electrical stress, monolayer h-BN maintains its atomically flat surface without such hillocks. They inferred that the outstanding heat dissipation capability of the monolayer h-BN suppressed thermally driven catastrophic breakdown. Consequently, the atomically thin single-crystal h-BN layer substantiates the suitability of h-BN as gate dielectrics, passivation layers, and substrates for electronic devices due to its outstanding dielectric properties such as high breakdown strength, excellent reliability, and low variability.

2.3.2. Thermal Properties

As summarized in **Table 2**, h-BN exhibits exceptionally high in-plane thermal conductivities compared to conventional oxide-based dielectrics and low-*k* materials. Although the out-of-plane thermal conductivity of h-BN is much lower than the in-plane

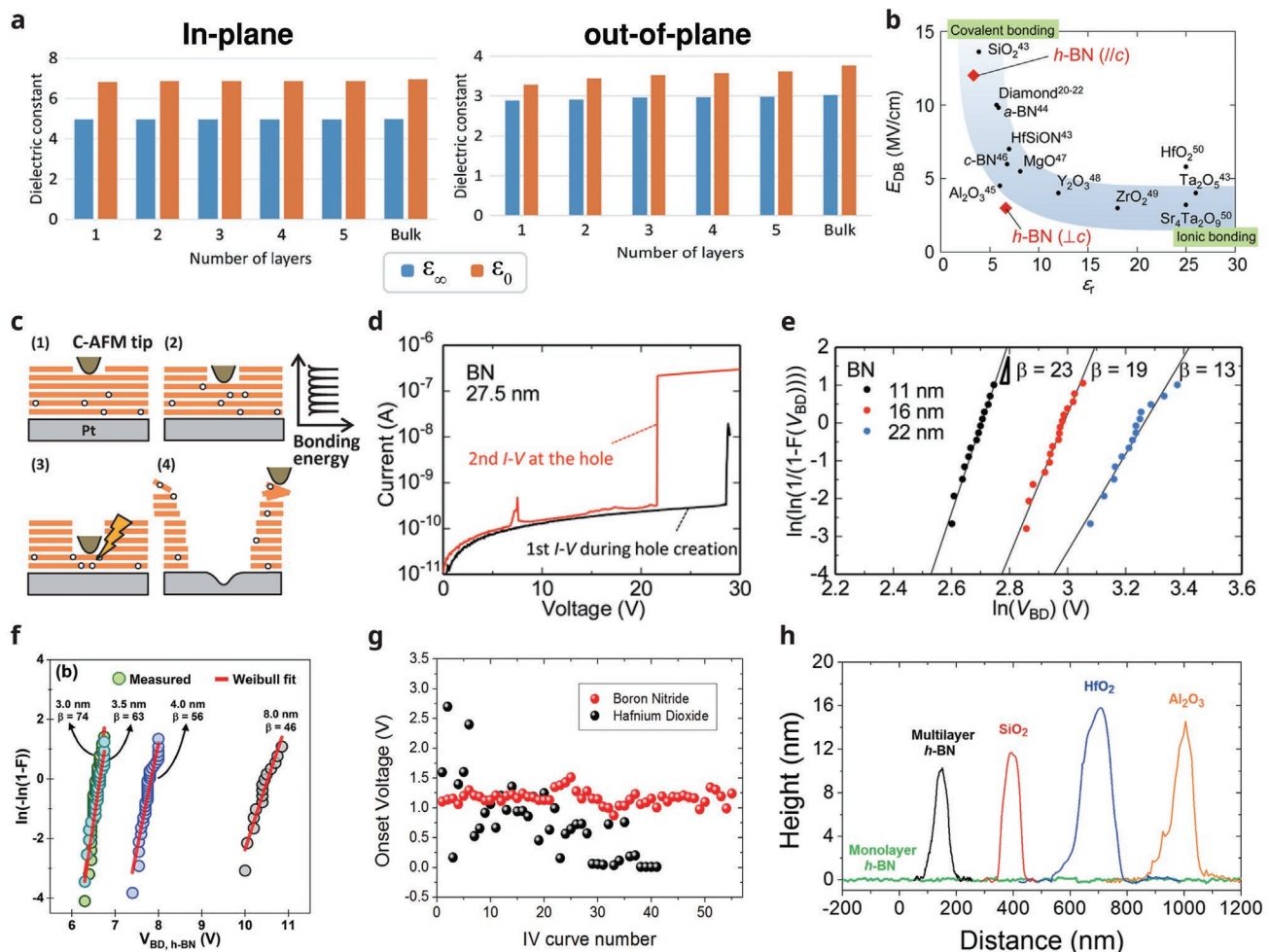


Figure 5. Characterization of h-BN dielectric properties in terms of dielectric constant and breakdown strength. a) The layer number dependence of in-plane and out-of-plane dielectric constant. ϵ_{∞} and ϵ_0 represent the macroscopic optical and macroscopic static dielectric constant, respectively. Adapted under the terms of the CC-BY Creative Commons Attribution 4.0 International license (<https://creativecommons.org/licenses/by/4.0/>).^[61] Copyright 2018, The Authors, published by Springer Nature. b) Breakdown strength (E_{BD}) as a function of dielectric constant (ϵ_f) for conventional dielectrics and h-BN. The anisotropic dielectric constant of h-BN in the direction of both parallel and normal direction to the c -axis ($E_{BD||c}$ and $E_{BD\perp c}$). Reproduced with permission.^[64] Copyright 2016, American Chemical Society. c) Schematic of layer-by-layer breakdown process in h-BN bulk crystal. The irreversible defects of h-BN by electrical stress are represented as open circles. d) I-V curves for the first-time breakdown of h-BN (thickness ≈ 27.5 nm) and the second-time breakdown of the remaining h-BN layers (thickness ≈ 16.5 nm). The black line is the first I-V curve, and the red line is the second I-V curve at the same points. e) Weibull plots of breakdown voltage (V_{BD}) distribution. The Weibull slope, β , values were estimated to be 23, 19, and 13, respectively, depending on the thickness of h-BN for 11, 16, and 22 nm. c-e) Reproduced with permission.^[62] Copyright 2015, American Chemical Society. f) Weibull plots of V_{BD} distributions at different h-BN thicknesses (3–8 nm) with the exceptionally high β . Reproduced with permission.^[67] Copyright 2021, American Chemical Society. g) Onset voltage versus the number of I-V curves for both h-BN and HfO₂ films. Reproduced with permission.^[76] Copyright 2016, AIP Publishing. h) The cross-sectional heights of the breakdown-induced hillocks in multilayer and monolayer h-BN and conventional dielectrics such as SiO₂, HfO₂, and Al₂O₃. The monolayer h-BN is only observed with no signal of the breakdown-induced hillock. Reproduced with permission.^[77] Copyright 2017, American Chemical Society.

values due to the highly anisotropic layered structure, it is still higher than that of common dielectric materials. The remarkable thermal property makes h-BN an excellent heat dissipation layer for thermal management applications. In addition, atomically thin nature of h-BN, when applied to 3D device integration, can significantly reduce the thermal resistance, enhancing the reliability and functionality of the integrated electronic devices.^[84] Despite such promising aspects, there is a lack of information on the accurate thermal conductivity value, its anisotropy, and thickness dependency. Thus, further systematic studies are required for a comprehensive interpretation of the h-BN thermal conductivity.

Recently, Jiang et al. experimentally and theoretically explored the anisotropic thermal conductivity of bulk single-crystal h-BN.^[85] They investigated the in-plane and out-of-plane thermal conductivities of h-BN over the temperature range of 100–500 K by using time-domain thermoreflectance techniques. Figure 6a,b shows the experimental and calculated thermal conductivity values with previously reported data. The room temperature in-plane (K_t) and out-of-plane (K_z) thermal conductivities were measured to be 420 ± 46 and $4.8 \pm 0.6 \text{ W m}^{-1} \text{ K}^{-1}$, respectively, which match well with the calculated ones.

Table 1. Reported values of the breakdown field of h-BN and conventional oxide-based dielectrics.

Material	Breakdown field [MV cm ⁻¹]	Thickness	Refs.
SiO ₂	13.2	7–15 nm	[73]
HfO ₂	4–8	5–30 nm	[74]
h-BN	11.8	monolayer	[78]
	13–21	3–8 nm	[67]
	7.94	1–31 layers	[79]
	9.75	2.0 nm	[80]
	7.80	3.0 nm	
	11–12	13–50 nm	[81]
	8.3	14.3 nm	[82]
	12 (c), 3 (⊥c)	10–100 nm	[64]
	7.6	17–20 nm	[83]
	12	11–27.5 nm	[62]

Cai et al. also investigated the thermal conductivity from monolayer to trilayer h-BN.^[86] As shown in Figure 6c,d, the monolayer of h-BN exhibits an average thermal conductivity of as high as 751 W m⁻¹ K⁻¹ at close to room temperature. They also revealed the effect of the number of h-BN layers on the thermal conductivity that drops to 646 and 602 W m⁻¹ K⁻¹ bilayer and trilayer, respectively, due to interlayer interaction.

The study on the h-BN thermal conductivity provides fundamental insight into the thermal transport properties of anisotropic 2D materials and can open avenues for next-generation

thermal management applications and diverse electronic devices.

3. h-BN for Next-Generation Photonics

Although bulk h-BN has an indirect bandgap, it shows intense emission and strong absorption thanks to its strong exciton-phonon coupling, high exciton binding energy, and short radiative lifetime, showing great potential as a promising light emitter and absorber in DUV spectral region. In addition, various deep levels contribute to stable single-photon emission from h-BN with high quantum efficiency covering from 2 to 4.1 eV, making h-BN a promising building block for an integrated quantum photonic platform.

3.1. Light Emitter in DUV Region

The wavelength range between 100 and 280 nm in the electromagnetic spectrum is referred to as UV-C or simply DUV light. Major uses of DUV light sources are food processing sterilization, purification of water and air, disinfection in hospitals, and medical applications due to its ability to effectively kill microbes.^[102–104] Mercury lamps have been widely used as DUV light sources for over 100 years,^[105] despite their problems including low efficiency, short lifetime, high power consumption, bulky and fragile characteristics, and serious environmental pollution from mercury use and disposal. By contrast,

Table 2. Reported thermal conductivity of h-BN and conventional oxide-based dielectrics, in both experiment (exp.) and calculation (calc.) at close to room temperature (RT).

Materials	Thermal conductivity [W m ⁻¹ K ⁻¹]		Thickness	Temperature [K]	Refs.
	In-plane	Out-of-plane			
SiO ₂	1.4		–	–	[87]
HfO ₂	1.2		>500 nm	–	[88,89]
Hydrogen-silsesquioxane (HSQ)	0.155–0.40		215–775 nm	298	[90]
Silica xerogel	1.35		0.5–2.5 μm	RT	[91]
h-BN	250 (exp.)	2.5 (exp.)	58 nm	235, 800	[92]
	360 (exp.)		11 layer	300	[93]
	390 (exp.)		10–20 nm	–	[94]
	227–280 (exp.)		9 layer	RT	[95]
	300 ± 30 (calc.)	–	Monolayer	300	[96]
	484 (exp.)	–	Bilayer	300	[97]
	315 ± 52 (exp.)	5.2 ± 0.6 (exp.)	Flake	300	[98]
	420 ± 46 (exp.)	4.8 ± 0.6	Bulk	300	[85]
	537 (calc.)	4.1			
	751 ± 340 (exp.)		Monolayer	RT	[86]
	849 (calc.)				
	585 ± 80	3.5 ± 0.8	Bulk (monoisotopic ¹⁰ B)	–	[99]
	550 ± 75 (exp.)	4.5 ± 1.4	Monoisotopic ¹¹ B		
	656 ± 27 (calc.)	–	Monolayer	300	[100]
	511.6 ± 71.2 (exp.)		Monolayer	–	[101]

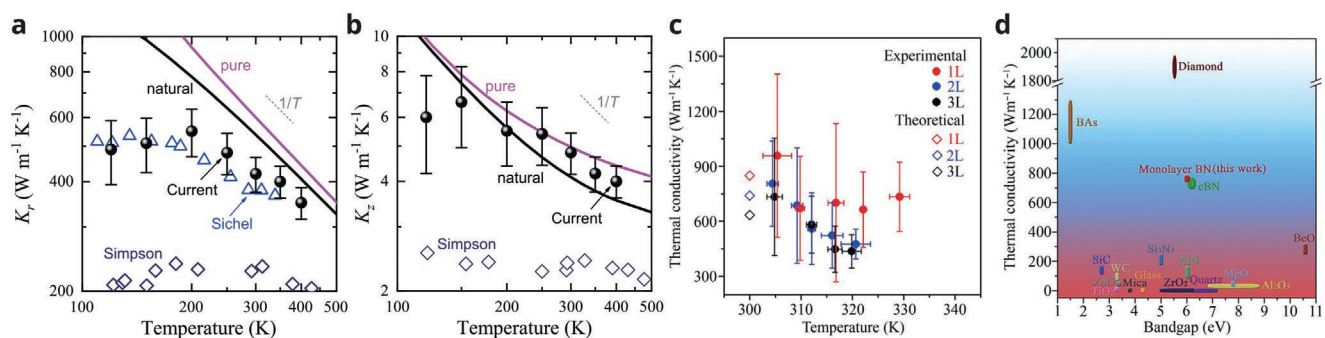


Figure 6. Thermal conductivity of h-BN. a) In-plane and b) out-of-plane thermal conductivities of h-BN from experimental data (solid symbols) and theoretical first-principles calculations (solid curves) as a function of temperature, compared with other literature data. a,b) Reproduced with permission.^[85] Copyright 2018, American Physical Society. c) Experimental thermal conductivity of from monolayer to trilayer h-BN as a function of temperature. d) Comparison of the thermal conductivity of general semiconductors and insulators. c,d) Reproduced under the terms of the CC-BY Creative Commons Attribution 4.0 International license (<https://creativecommons.org/licenses/by/4.0/>).^[86] Copyright 2019, The Authors, published by American Association for the Advancement of Science.

AlGaN-based DUV light-emitting diodes (LEDs) exhibit compact size, long lifetime, environmental friendliness, and low power consumption, covering a wide range of UV wavelengths from 365 nm (GaN) down to 210 nm (AlN) by modulating Al mole fraction in AlGaN. The promise of AlGaN-based DUV LEDs goes beyond simply replacing the mercury lamps in conventional DUV applications.

However, the external quantum efficiency (EQE) of AlGaN-based DUV LEDs is fundamentally limited by the high activation energy of Mg acceptors, resulting in low IQE,^[106] and strong anisotropic TM-polarized emission leading to low light-extraction efficiency.^[107,108] These fundamental problems of AlGaN-based LEDs become more severe when the Al fraction in AlGaN increases, i.e., the emission wavelength goes shorter, calling for a new material platform for DUV light sources.

h-BN has been emerged as a promising candidate for active emissive material in DUV light emitters, overcoming the fundamental limitations of AlGaN-based LEDs. At first, few-layer or bulk h-BN exhibits bright DUV emission with high IQE, despite

its indirect-bandgap nature, due to the strong exciton–phonon interaction, high exciton binding energy, and short radiative lifetime. Schué et al. corroborated the high IQE of h-BN by measuring temperature-dependent CL compared to zinc oxide (ZnO) and diamond (Figure 7a).^[109] Whereas the band-edge emission of a diamond is unstable above 60 K, the bright near-band-edge emission at 215 nm (~5.77 eV) in h-BN remains stable up to room temperature due to its high exciton binding energy. Moreover, the quantum yield is as high as 50% in bulk h-BN, comparable to that of the direct-bandgap ZnO. Majety et al. reported a much stronger DUV PL emission (5.48 eV) in h-BN compared to AlN. At 10 K and room temperature, the emission from h-BN is about two orders of magnitude higher than that of crystalline AlN epilayers, as shown in Figure 7b.^[110] For AlN, there is a redshift of the PL peak by ~80 meV with increasing temperature from 10 to 300 K, whereas there is no change in h-BN. Also, even in the case of the near-band edge emission, the peak shifts only below 25 meV with increasing temperature from 8 to 300 K.^[41] Second, DUV photons generated in h-BN

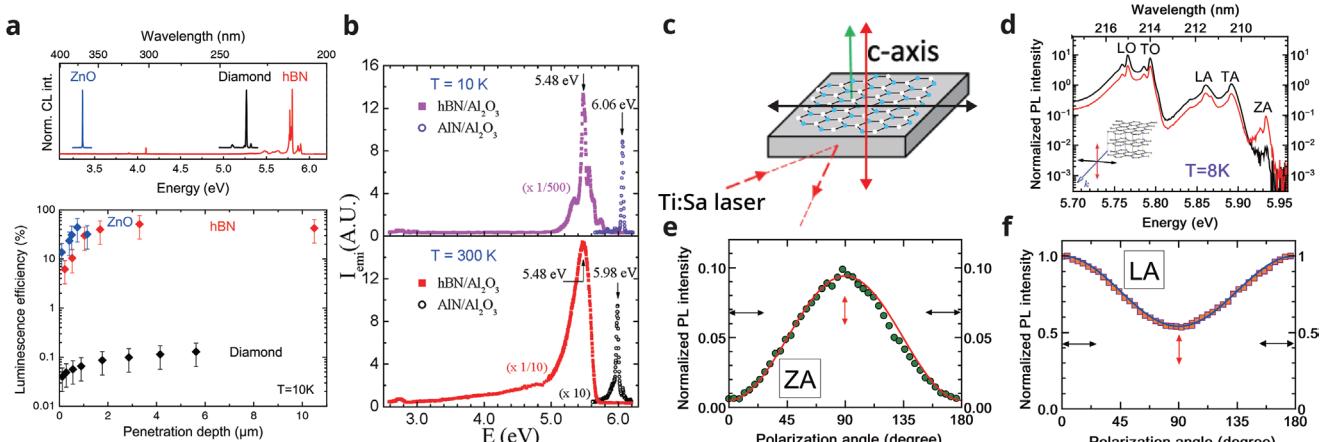


Figure 7. a) CL spectra at 10 K and luminescence efficiencies of ZnO, h-BN, and diamond. Reproduced with permission.^[109] Copyright 2019, American Physical Society. b) PL spectra of h-BN and AlN at 10 K and room temperature (300 K). Reproduced with permission.^[110] Copyright 2012, American Institute of Physics. c) Schematic of bulk h-BN measurements where the emission wave-vector is perpendicular to the *c*-axis. d) Polarization-resolved PL spectra in bulk h-BN at 8 K for linear polarization detection. The red (black) line means the detection when it is parallel (perpendicular) to the *c*-axis. e,f) Normalized PL emission intensity of the ZA (e) and LA (f) phonon replicas according to the polarization angle. c-f) Adapted under the terms of the CC-BY Creative Commons Attribution 3.0 Unported license (<https://creativecommons.org/licenses/by/3.0/>).^[111] Copyright 2016, IOP Publishing.

can be effectively extracted due to: i) the suppression of reabsorption by the Stokes shift between phonon-assisted emission and absorption processes, and ii) dominant isotropic emission compared to AlN that emits a strong anisotropic TM-polarized light. Vuong et al. measured polarization-resolved PL at 8 K in bulk h-BN as shown in Figure 7c.^[111] The black line and the red line in Figure 7d represent the emission polarized perpendicular to the *c*-axis, and along the *c*-axis, respectively. In the layered structure of bulk h-BN, there are two types of transverse modes when a phonon wave-vector *k* is perpendicular to the *c*-axis. One is a mode related to in-plane atomic displacements, TO and TA, and the other is an out-of-plane vibration mode, ZO, and ZA. Since the ZA phonon replica is strongly polarized along with the *c*-axis, the PL intensity of the ZA phonon replica increases in the polarized emission along with the *c*-axis (red line in Figure 7d,e), and decreases perpendicular to the *c*-axis (black line in Figure 7d,e). Conversely, the PL intensity of the phonon replica decreases when detecting along the *c*-axis due to the transverse and longitudinal phonon modes, which are polarized in the in-plane direction. As shown in Figure 7d, the overall intensity reduction of the LO, TO, LA, and TA phonon replicas, which are linearly polarized perpendicular to the *c*-axis, is observed. This causes an anticorrelation of the polarization dependence in the ZA and LA phonon replicas (Figure 7e,f). Consequently, the extraction efficiency of h-BN is expected to be much higher than that of AlN due to less reabsorption of emitted DUV photons as well as dominant isotropic emission.

Despite such promising optical properties of h-BN, the implementation of h-BN in DUV light emitter is still in its infancy. Watanabe et al. fabricated a far-ultraviolet (FUV) planar-emission device with a fluorescent screen containing h-BN powder as shown in Figure 8a.^[112] This FUV plane-emission device operates stably with an output power of 0.2 mW at an excitation voltage of 8 kV. The h-BN is excited by electrons accelerated by a high voltage (5 kV) applied to the anode. As a result, the h-BN emits FUV fluorescence with an emission peak at 220 nm (5.64 eV) which originates from the near-band edge as shown in Figure 8b.^[113] The weak tail from 250 to 400 nm originates from impurities and defect states.^[117–120] Although this portable FUV CL emitter exhibited the near-band-edge emission with a long lifetime and low power consumption, its efficiency is low ($\approx 0.6\%$). Note that this is the first attempt to fabricate a DUV light emitter with an h-BN emissive layer using CL.

However, CL requires a high voltage, about a few kV, to accelerate electrons enough to excite the active materials, whereas electroluminescence (EL), like luminescence from LEDs, requires only a few voltages to inject carriers into the active region where radiative recombination of carriers occurs. Compared to CL devices, EL devices have many advantages such as low power consumption, small size, and high efficiency. Many efforts have been made to realize an efficient h-BN-based EL emitter, i.e., h-BN LED. Lee et al. demonstrated an h-BN-based EL device consisting of alternately stacked 9 nm-thick Al₂O₃ and 3 nm-thick h-BN so that the Al₂O₃ layers act as potential barriers to confine the carriers injected into the h-BN wells, mimicking the multiple quantum well active region widely used in current LED technology, as shown in Figure 8c.^[114] In PL measurement, the Al₂O₃/h-BN multiple heterostructures exhibited

two near-band-edge emission lines with higher intensity than the h-BN-only structure without Al₂O₃ barriers, attributed to the confinement of excitons in the h-BN, enhancing the probability of radiative recombination.^[121,122] However, no band-edge emission was observed, yet, broad EL emission was observed in the visible wavelength range, which is attributed to the defect-mediated emission from the h-BN wells. Kim et al. proposed a graphene/h-BN/graphene vdW heterostructure device with additional thick top- and bottom-h-BN for encapsulation, as shown in Figure 8d,^[115] and demonstrated the first NUV light emission in h-BN at high electrical bias. The h-BN between the graphene layers is the active emissive layer. When the voltage was increased above 1 V nm⁻¹, the device started to emit NUV light by radiative recombination via active defects. This NUV light emission was initiated at the edge of the region where h-BN and graphene electrodes overlap and expanded over the entire area as the electrical bias increased. This is because the local electric field is stronger at the edge of the graphene. This device shows a strong peak at the 394 nm (3.14 eV) originating from the active defects in the h-BN and a broad emission peak in the visible region. Recently, Song et al. demonstrated the first band-edge EL and photocurrent generation in the h-BN exfoliated from a crystal. As shown in Figure 8e, the exfoliated h-BN active layer is located between monolayer graphene electrodes, which are capped with top and bottom h-BN layers. Figure 8f shows the EL spectra at 10 K for three devices, and Figure 8g shows the PL spectrum at 10 K using a laser with 6.22 eV excitation energy. A series of emission lines in the PL spectrum originates from the band-to-band transition, and is also present in the EL spectrum. The S-series lines, 5.89 (S₁ line), 5.86 (S₂ line), 5.79 (S₃ line), and 5.76 eV (S₄ line), represent the emission of TA, LA, TO, and LO phonons at the T point, respectively. Besides sharp band-edge emission lines, the broad lines originating from defects in the h-BN called D-series, are observed below 5.7 eV. Although their h-BN-based DUV light emitters exhibited a low EQE ($\approx 10^{-5}\%$) at room temperature, it is the first band-edge EL device with an h-BN active layer, demonstrating promising potential toward highly efficient h-BN based optoelectronic devices at DUV range. There is abundant room for further progress in the improvement of efficiency by implementing current LED technologies such as multiple quantum well heterostructures for improving carrier injection and suppressing carrier leakage, and formation of low resistivity ohmic contacts, etc.

3.2. Single-Photon Emitters

SPE is a promising building block for the development of quantum information technology which requires quantum indistinguishability.^[123–124] Desirable properties of SPEs for practical applications include high brightness, stable room temperature operation, and high purity of single-photon. At an early stage of SPE, many researchers have focused on large-bandgap materials including diamond and SiC for room temperature operation. Recently, h-BN has attracted enormous attention owing to its stable and efficient emission at room temperature.^[23] Moreover, h-BN-based SPEs exhibit a wide range of emission wavelengths, from NIR to NUV, which makes h-BN a unique and promising material for SPEs. Substantial research

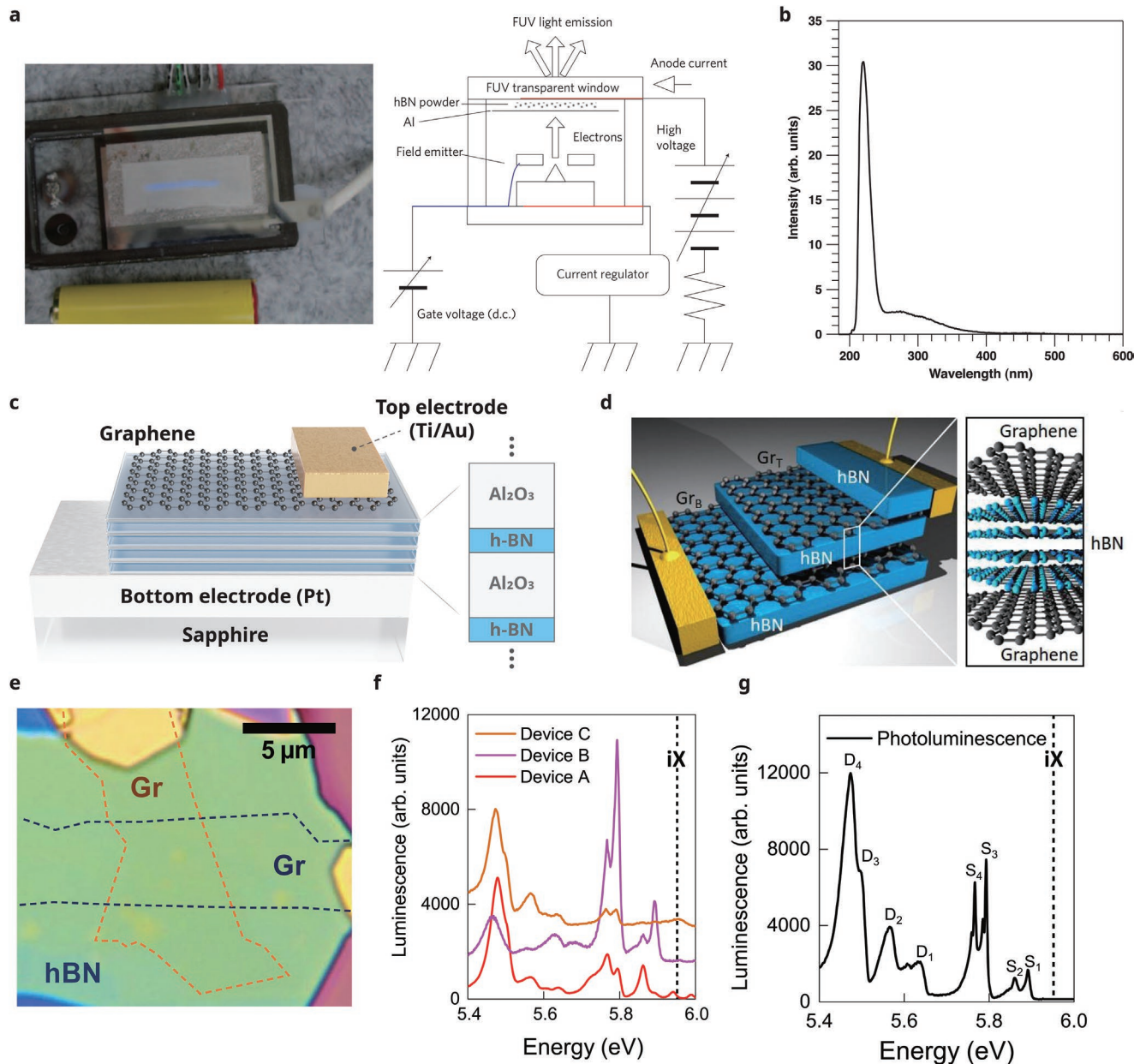


Figure 8. a) Photograph of an operating FUV plane-emission compact device and schematics of the device and connected electric circuits. Reproduced with permission.^[112] Copyright 2009, Springer Nature. b) Output spectrum of FUV device. Reproduced with permission.^[113] Copyright 2011, The American Ceramic Society. c) Schematics of EL device composed of a five-periods $\text{Al}_2\text{O}_3/\text{h-BN}$ multiple heterostructure and graphene (Gr)-top and Pt-bottom electrodes. d) Schematics of a vdW-stacked h-BN/Gr/h-BN/Gr/h-BN heterostructure. e,f) Reproduced with permission.^[115] Copyright 2019, IEEE. e) Optical microscopy image of the EL device. f) DUV EL spectra of three devices at 10 K. g) The PL spectrum of exfoliated h-BN at 10 K. e–g) Adapted under the terms of the CC-BY Creative Commons Attribution 4.0 International license (<https://creativecommons.org/licenses/by/4.0/>).^[116] Copyright 2021, The Authors, published by Springer Nature.

has been carried out to explore the origin of single-photon emission in a wide range of wavelengths, i.e., which deep-level defect is responsible for a specific emission spectrum.

Tran et al. first reported single-photon emission from both monolayer and multilayer h-BN at 623 nm (Figure 9a),^[21] and suggested that $\text{V}_\text{N}\text{N}_\text{B}$, an antisite complex in which the N substitution on the B site (N_B) is located next to the N vacancy(V_N), is the most probable candidate through DFT calculation, consistent with other studies.^[125,126]

In addition to native defects including vacancies, interstitials, and antisites, external impurities can be incorporated in h-BN, forming carbon-, and oxygen-related deep-level defect complexes acting as single-photon emission sources. After Tawfik et al. suggested carbon-based defect is the origin responsible for the SPE at 635 nm through DFT calculation,^[127] many researches have backed up this result.^[128–131] Notably, Mendelson et al. intentionally incorporated various impurities including Si, O, and C in h-BN by ion-implantation, and reported that only

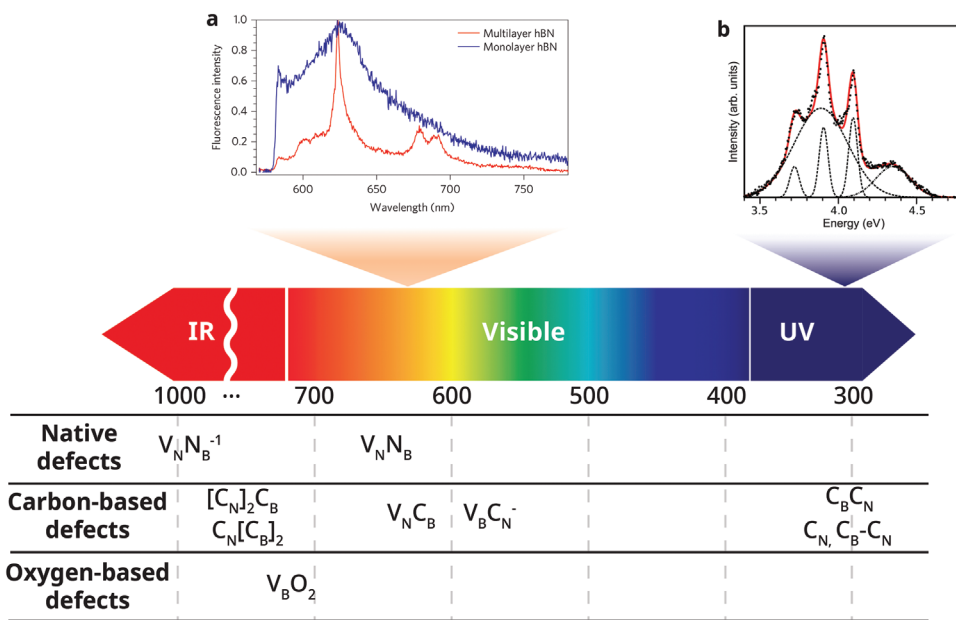


Figure 9. Typical emission spectra of h-BN SPEs from infrared (IR) to NUV and proposed deep-level defects as corresponding origins of the single-photon emission spectra. The type of possible origin is categorized into three groups, including native defects, carbon-based defects, and oxygen-based defects. a) PL spectrum of the first reported quantum emission in h-BN at 623 nm. Reproduced with permission.^[21] Copyright 2015, Springer Nature. b) CL spectrum of first reported quantum emission at NUV region (≈ 300 nm, 4.1 eV). Reproduced with permission.^[25] Copyright 2016, American Chemical Society.

C-implanted h-BN shows single-photon emission near 580 nm, and concluded that carbon-based defects, $V_B C_N^-$, is the origin by DFT calculation.^[128] Furthermore, several works have also proposed carbon-based defects as promising candidates for the creation of single-photons in the UV wavelength range. After Bourrellier et al. reported the first quantum emission at near 300 nm (4.09 eV) using CL (Figure 9b), theoretical calculations also revealed that $C_B C_N$,^[132] C_B ,^[133] and other carbon-related defects^[131,134] are origins of the single-photon emissions near 300 nm (≈ 4.1 eV). The wavelengths of single-photon emissions from exfoliated h-BN (flake) or grown h-BN with corresponding proposed defect origins are summarized in Figure 9 and Table 3. Although the exact origins of single-photon emission in h-BN at specific wavelengths are still under debate, carbon-based defects are mainly suggested as most likely candidates for both the NIR-visible and UV range via combined theoretical and experimental works.

For the practical application of SPEs for quantum information technology, there are desirable aspects. It would be greatly beneficial for real-world applications if an SPE could create single-photons with high efficiency, with tunable wavelengths by controlling external stimuli, at intentionally defined locations. Many efforts have been devoted to realizing such SPEs using various methods. First, defining the location of SPE is a particularly important technological step toward integrated and scalable device technology.^[136,137] Motivated by h-BN SPEs tend to form at edges, Ziegler et al. fabricated an array of holes in h-BN by using focused-ion beam milling and found that single-photon emission was observed predominantly at the perimeter of the holes, as shown in Figure 10a.^[138] The location of SPE can also be controlled by nanoindenting h-BN with an AFM

probe, followed by activation annealing under Ar ambient (Figure 10b).^[139] Other reported methods to define the SPE location include the capillary assembly of suspended h-BN particles into submicron polymer holes,^[140] and integration of h-BN SPE in SiN waveguide,^[141] and electron beam irradiation.^[137] Stewart et al. achieved SPEs localization both laterally and vertically using annealing and fluorescence quenching with a pre-patterned graphene mask (Figure 10c).^[136] SPEs are activated

Table 3. The wavelengths of single-photon emissions from exfoliated h-BN (flake) or grown h-BN by chemical vapor deposition (CVD) or metal–organic chemical vapor deposition (MOCVD) with corresponding proposed defect origins.

Proposed defect origin	Wavelength	Method	Refs.
$V_N N_B^{-1}$	998 nm (1.24 eV)	Exp. (Flake) Calc. (DFT)	[24]
Neutral C trimers	760 nm (1.63 eV), 751 nm (1.65 eV)	Calc. (DFT)	[123]
$[C_N]_2 C_B$, $C_N[C_B]_2$			
$V_B O_2$	711 nm (≈ 1.74 eV)	Exp. (Flake) Calc. (DFT)	[135]
$V_N N_B$	646 nm (1.92 eV)	Calc. (DFT)	[125]
$V_N C_B$	635 nm (1.951 eV)	Calc. (DFT)	[127]
$V_N N_B$	623 nm (1.99 eV)	Exp. (CVD-grown) Calc. (DFT)	[21]
$V_N C_B$	620 nm (≈ 2 eV)	Calc. (DFT)	[129]
$V_B C_N^-$	580 nm (2.137 eV)	Exp. (MOCVD-grown) Calc. (DFT)	[128]
$C_B C_N$	304 nm (4.08 eV)	Calc. (DFT)	[132]
$C_B - C_N$	302 nm (4.1 eV)	Calc. (DFT)	[123]

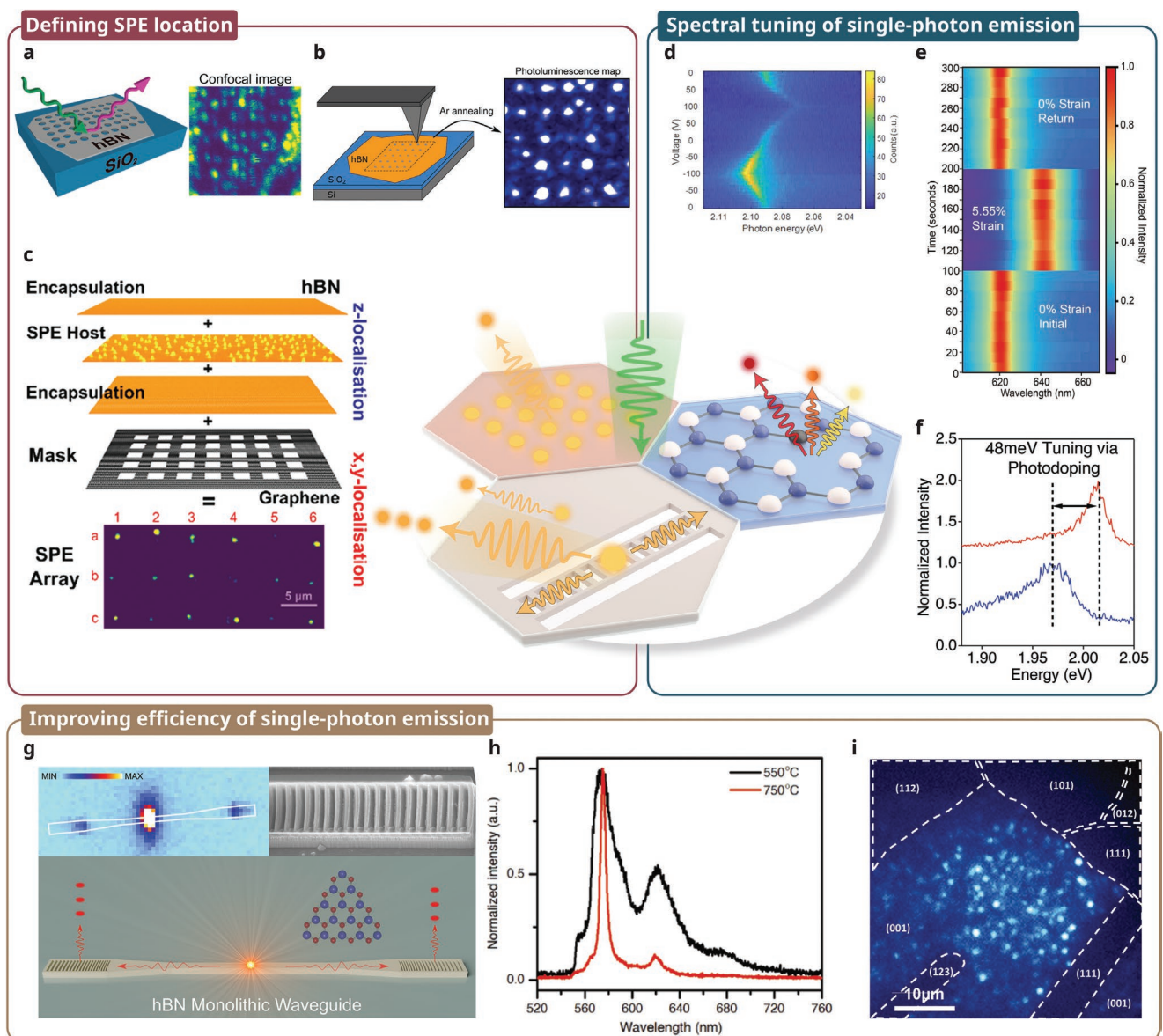


Figure 10. a–c) Recent research focused on: a–c) defining SPE location, d–f) spectral tuning of single-photon emission, g–i) improving the efficiency of single-photon emission. a) (Left) Schematic of patterned h-BN SPEs by FIB milling. (Right) Confocal scan for SPE indicating high emission visibility. Reproduced with permission.^[138] Copyright 2019, American Chemical Society. b) (Left) Schematic of the activation of h-BN SPEs by AFM nanoindentation. (Right) PL map of the flake after nanoindentation, after Ar annealing. Reproduced with permission.^[139] Copyright 2021, American Chemical Society. c) Schematic of the monolayer engineering approach of emitter localization in 3D. Reproduced with permission.^[136] Copyright 2021, American Chemical Society. d) ZPL intensity map of the h-BN SPE as a function of the applied voltage to the electrode. Reproduced with permission.^[142] Copyright 2019, American Chemical Society. e) A time-resolved photoluminescence (TRPL) before and after release of the strain (bottom and top), 5.55% strain (middle). Reproduced with permission.^[145] Copyright 2020, Wiley-VCH. f) Normalized PL spectra of an SPE. Reproduced with permission.^[144] Copyright 2019, American Chemical Society. g) Schematic of h-BN SPE in a monolithic waveguide. Enhanced coupling efficiencies of emitter-waveguide are achieved. (Inset) PL map of h-BN waveguides. Reproduced with permission.^[146] Copyright 2021, American Chemical Society. h) Representative PL spectra of h-BN SPEs annealed at 550 °C (black) and 750 °C (red). The FWHM of ZPLs is ≈18.0 and 4.0 nm, respectively. Reproduced under the terms of the CC-BY Creative Commons Attribution 4.0 International license (<https://creativecommons.org/licenses/by/4.0/>).^[151] Copyright 2018, The Authors, published by De Gruyter. i) Wide-field imaging (white dashed area) confirms the high density of SPEs on (001) Ni grains. Reproduced with permission.^[155] Copyright 2020, Wiley-VCH.

by annealing under Ar ambient, but deactivated by annealing under air ambient that causes oxidation of h-BN. They achieved lateral-emission localization via quenching with a patterned graphene mask, and selectively activate only the middle layer of h-BN by the Ar annealing.^[136]

Second, a wide spectral tuning range is desirable for scaling up quantum information processing such as wavelength division multiplexing quantum key distribution,^[142] which can be achieved by controlling external stimuli, for example, strain, electric field,^[143] and electrostatic gating.^[144]

Xia et al. first reported room temperature Stark tuning by applying voltages, showing the Stark shift of single-photon energy up to $43 \text{ meV} \times (\text{V nm})^{-1}$ (Figure 10d).^[142] Tuning the spectral range can also be achieved by strain engineering.^[41] Mendelson et al. reported red and blue spectral shifts up to 65 meV (Figure 10e)^[145] by applying tensile strain to the h-BN on PDMS, which leads to the broadening of the zero-phonon line (ZPL) linewidth. A theoretical model related to the strain susceptibility and the angle between the strain field and the defect dipole moment was introduced to explain the effect of strain on the shift of single-photon energy.^[145] Using electrostatic gating, the spectral shift of up to 48 meV was observed, which was attributed to the field-assisted photodoping due to injected and trapped charges in defects close to SPEs (Figure 10f).^[144]

Thirdly, many efforts have been made to improve the efficiency of SPEs using various methods. Integrating SPEs into a photonic component is a promising way to achieve enhanced brightness and purity of single-photon emission. For example, enhanced coupling efficiencies^[146–150] and high purity^[141,150] of SPEs can be achieved by combination with a photonic waveguide,^[141,146] and cavity.^[147–150] Li et al. achieved ≈ 4 times enhanced coupling efficiency by introducing a monolithic waveguide to h-BN (Figure 10g).^[146] In the figure, h-BN SPE is located at the center of the waveguide, the brightest spot on the PL map, and the other two bright spots on both sides of the waveguide give a clue for efficient coupling via waveguide mode. Various processes have been proposed to enhance the efficiency of SPEs, including post-annealing of SPEs,^[136,139–140,151,152] and plasma etching for removing residual polymers, resulting in much reduced linewidth of the SPE spectrum (Figure 10h),^[151] and longer lifetime.^[153] Furthermore, h-BN grown by CVD with an appropriate condition exhibits improved crystallinity,^[154] narrow ZPL distribution,^[144] and bright single-photon emission.^[155] Mendelson et al. corroborated grain-dependent single-photon emission in h-BN grown on different Ni grain orientations. Single-photon emissions were observed only on (001) Ni grains (Figure 10i)^[155] because of the high diffusivity of impurity atom on (001) Ni grains. Although the grain-dependent diffusion effects were also found on the Cu substrate, (001) Ni shows 2.5-fold enhanced emission intensity compared to the Cu substrate.^[155]

After Tran et al. reported the first single-photon emission in h-BN in 2016, research on the h-BN SPEs has substantially

expanded to explore the origin of single-photon emissions in a wide spectral range, and to enhance practical aspects of h-BN-based SPEs including defining SPE location, spectral tuning, and improving the efficiency of single-photon emission. Although there are still many remaining challenges toward real-world applications, h-BN SPEs will play a key role in the integrated quantum photonic technology in the near future.

3.3. DUV Photodetectors

Solar-blind DUV (200–280 nm) photodetection has gained grand interest in recent years because of significant applications in diverse fields such as remote control, chemical monitoring, radiation detection, missile warning systems, and space communication. Silicon photodiodes have been widely used for DUV photodetection, however, due to the narrow bandgap of silicon, additional optical equipment and high-power operation are required for securing high selectivity in the DUV range.^[156] Diamond and AlN have been suggested as promising DUV photodetector materials due to their solar blindness and low dark current characteristics enabled by ultrawide-bandgap nature. Recently, h-BN has emerged as a very promising material due to its more appropriate optical properties for DUV detection compared to diamond and AlN. At first, h-BN shows a giant light-matter interaction despite its indirect-bandgap nature, enabled by electronic flat bands, i.e., the conduction and valence bands are nearly parallel and flat along a specific Brillouin zone, inducing the macroscopic degeneracy of the direct transitions along with the KH line parallel to the *c*-axis (Figure 11a).^[44] This degeneracy leads to van Hove singularities, which results in a high electronic density of states participating in the DUV absorption process.^[157] Second, h-BN can capture significant DUV light with a high band-edge absorption coefficient. The band-edge absorption coefficient of h-BN was first estimated by Zunger et al. to be $\approx 5 \times 10^5 \text{ cm}^{-1}$ at room temperature.^[158] Recently, Vuong et al. reported the band-edge absorption coefficient of h-BN on the sapphire substrate.^[159] With little variations of the absorption spectrum around 6 eV dependent on the growth condition of each h-BN layer, the absorption peaks at around 6.02 eV were measured, and the maximum value of the band-edge absorption coefficient was

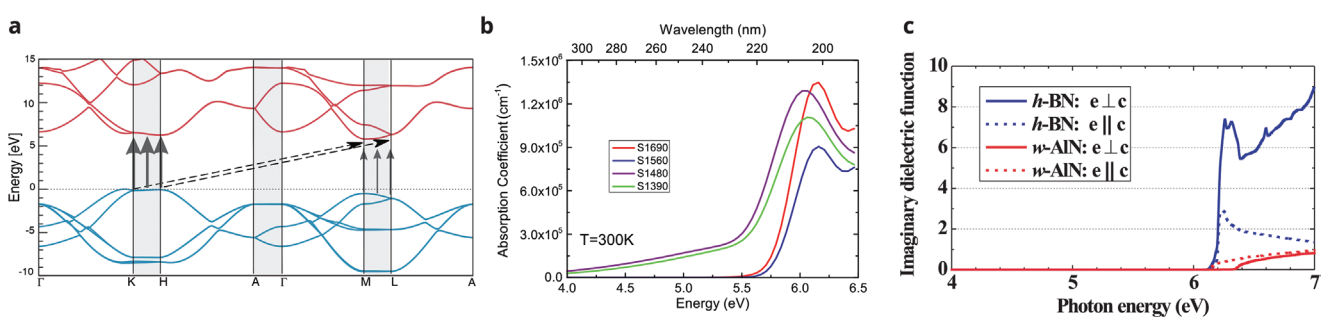


Figure 11. a) Electronic band structure evaluated by many-body GW calculations. Reproduced with permission.^[44] Copyright 2021, American Physical Society. b) Absorption spectrum in four h-BN samples grown on sapphire substrate, which is labeled as S followed by the growth temperature in °C (1690 °C, 1560 °C, 1480 °C, 1390 °C). Reproduced under the terms of the CC-BY Creative Commons Attribution 3.0 Unported license (<https://creativecommons.org/licenses/by/3.0/>).^[159] Copyright 2017, IOP Publishing. c) The calculated imaginary dielectric function $\varepsilon_i(\omega)$ of h-BN and w-AlN as a function of the polarization of the light \vec{e} . Reproduced with permission.^[165] Copyright 2012, American Physical Society.

$1.4 \times 10^6 \text{ cm}^{-1}$ (Figure 11b). The absorption peaks result from the optical response of h-BN including phonons with a finite group velocity, which leads to the phonon replicas with sharp resonances. Li et al. also estimated the band-edge absorption coefficients of a 30 nm-thick h-BN layer of above 10^6 cm^{-1} , much higher than that of wurtzite AlN with direct bandgap ($\approx 2 \times 10^5 \text{ cm}^{-1}$).^[160,161] h-BN exhibits strong optical absorption above the bandgap as a result of the interband transition from s and p states of N to s and p states of B.^[162] In addition to the high-absorption coefficient, h-BN has a significantly improved absorption intensity at the band-edge with a short absorption tail.^[163,164] The imaginary dielectric function $\epsilon_i(\omega)$ of h-BN and AlN as a function of the polarization of the light \vec{e} is shown in Figure 11c.^[165] The absorption peak of $\vec{e} \parallel \vec{c}$ is considerably smaller than that along the $\vec{e} \perp \vec{c}$ direction in h-BN, whereas the dispersion $\epsilon_i(\omega)$ at the absorption edge for AlN is proportional to the conventional $(E_{cv} - E_g)^{1/2}$. Consequently, h-BN has much more appropriate optical properties for DUV photodetection, compared to other wide-bandgap materials, including visible-blindness, sharp cut-off at the bandgap, and very high absorption coefficient in DUV range.

Li et al. demonstrated that the estimated absorption coefficient ($7 \times 10^5 \text{ cm}^{-1}$) and dielectric strength ($\approx 4.4 \text{ MV cm}^{-1}$) of h-BN are larger than that of AlN ($\approx 2 \times 10^5 \text{ cm}^{-1}$, 4.1 MV cm^{-1}). They fabricated a metal–semiconductor–metal type photodetector with a sharp cut-off wavelength of around 230 nm and a very small response in the long wavelengths up to 800 nm.^[160] However, DUV to visible rejection ratio ($R_{\text{DUV}}/R_{\text{visible}}$) was several orders of magnitude lower than that of AlN photodetectors. To improve the overall performance of h-BN DUV photodetectors, various efforts have been made including enhancing crystallinity of h-BN by direct growth and post-growth treatments, impurity doping, and inducing localized surface plasmon resonance (LSPR) by incorporating metallic nanoparticles (NPs).

Enhancing Crystallinity of h-BN: To avoid inevitable contamination and mechanical damage from the typical transfer process of h-BN grown on a catalytic substrate onto a target substrate, many approaches have been attempted to grow h-BN directly on target substrates followed by postgrowth treatments for enhancing the crystallinity of h-BN. Li et al. grew h-BN films on quartz, sapphire, and Si (100) substrates via ion beam assisted deposition at a low temperature 500 °C, and showed high peak responsivity with an excellent on/off ratio ($I_{\text{ph}}/I_{\text{dark}}$) of 10^3 at 204 nm (Figure 12a) and a high rejection ratio ($R_{204\text{nm}}/R_{250\text{nm}} > 10^3$) from h-BN photodetector directly grown on the quartz substrate.^[166] Introducing postgrowth treatments has been reported to be effective for improving crystallinity, thus, enhancing device performance. Gao et al. reported that N⁺ sputtering can supplement the deficiency of N of as-grown h-BN, which enabled the fabrication of N sufficient h-BN-based photodetectors with a high on/off ratio of 6800 (Figure 12b) and a fast response time of 1 ms (Figure 12c) in wafer scale.^[167] Chen et al. introduced high-temperature annealing not only for removing defects in h-BN films but also for increasing the size of h-BN grains.^[168] They reported that the responsivity of h-BN film annealed in N₂ ambient at 1700 °C for 10 min was about nine times higher than that of the as-grown h-BN film (Figure 12d).

Impurity Doping: In situ doping of impurities during h-BN growth has been suggested to enhance the performance of photodetectors. Chen et al. reported the increase of photocurrent from 6.3 to 16.7 nA and a high on/off ratio of 1.03×10^4 by introducing 1.8 at% C by controlling CH₄ during the growth (Figure 12e).^[169] Wang et al. also reported that C doping can be an effective method to improve the performance of h-BN photodetectors through bandgap narrowing and sub-bandgap absorption.^[170] Tan et al. proved that optoelectronic properties of h-BN can be modulated by substitutional doping with S on a molten Au substrate during the CVD growth.^[171] Due to enhanced electrical conductivity and light absorption of the S-doped h-BN, the photocurrent and the responsivity of the S doped h-BN photodetector are about 50 times higher than that of the photodetector with an intrinsic h-BN layer (Figure 12f).

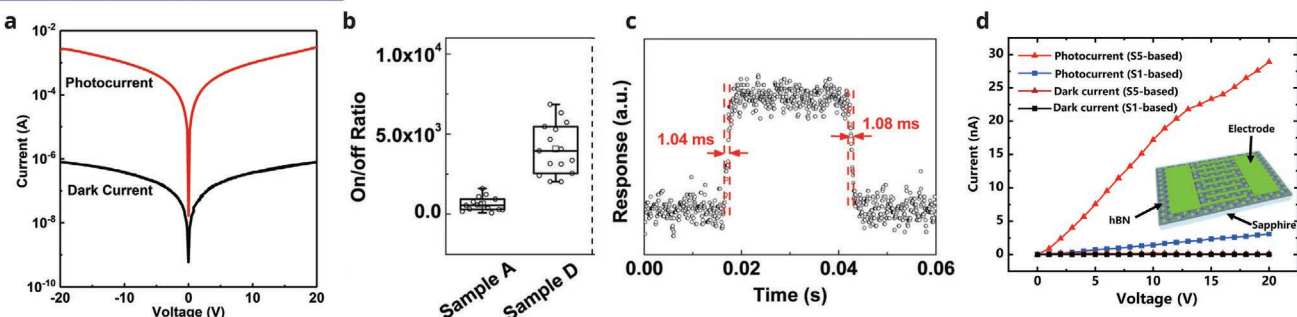
Localized Surface Plasmon Resonance: Recently, it was reported that introducing the LSPR effect by incorporating metal NPs on h-BN is very effective to enhance light-absorbing performance. A strong LSPR induced by the metallic NPs leads to greatly increased photocarrier injection, offering the rapid charge transfer of hot electrons with increased photocurrent. Zhu et al. attempted to introduce plasmonic enhancement by incorporating Au NPs in the h-BN photodetector, which resulted in remarkable improvement of photoresponse.^[172] The photocurrent of the h-BN photodetector with Au NPs was increased 7–9 times under 205 nm illumination due to the enhanced numbers of photoexcited electron–hole pairs (Figure 12g). Note that the antisymmetric current offset is induced since Au NPs are located only on one end as shown in the inset of Figure 12h.

Besides the efforts made to enhance the overall efficiency of h-BN DUV photodetectors, the current research trend includes securing the flexibility of h-BN DUV photodetectors and expanding the detection wavelength range down to vacuum-UVC (UUV, 10–200 nm). Flexible optoelectronic and electronic devices have been a recent surge in interest and research. h-BN is a good candidate material to be used in flexible devices due to its atomically thin 2D nature and high fracture strength. h-BN possesses a high fracture strength of 26.3 GPa, which is about ten times larger than that of AlN (0.61–2.76 GPa), offering that h-BN can be fabricated as flexible DUV photodetectors with stable bendability.^[173,174] Veeralingam et al. fabricated flexible h-BN photodetectors through the synthesis of h-BN by a one-step solid reaction.^[175] They showed a fast response time of 0.2 s and notable stability after 500 cycles of continuous bending, high detectivity of 6.1×10^{12} Jones, and a quantum yield of 2945% at a power intensity of $9.937 \mu\text{W cm}^{-2}$. Lin et al. employed high thermal conductivity nanopaper composed of h-BN nanosheets to form flexible photodetectors.^[176]

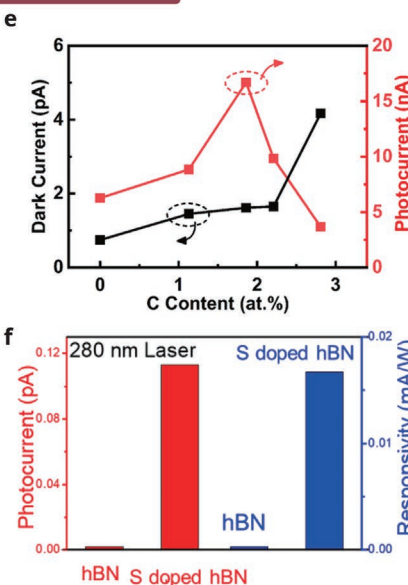
On the other hand, since h-BN photodetectors exhibit sharp cut-off wavelengths around 200 nm, they can even be applied to VUV light detection for applications in the diverse area such as spectroscopy and space communication. Although VUV light detection is still in its infancy due to the complexity of the experimental setup, there have been noteworthy studies about h-BN VUV photodetectors with excellent performance in wavelengths shorter than 200 nm.^[177–179]

In addition to the photonic applications in DUV and visible spectral ranges, h-BN can also be employed for infrared (IR)

Enhancing crystallinity of h-BN



Impurity doping



Localized Surface Plasmon Resonance (LSPR)

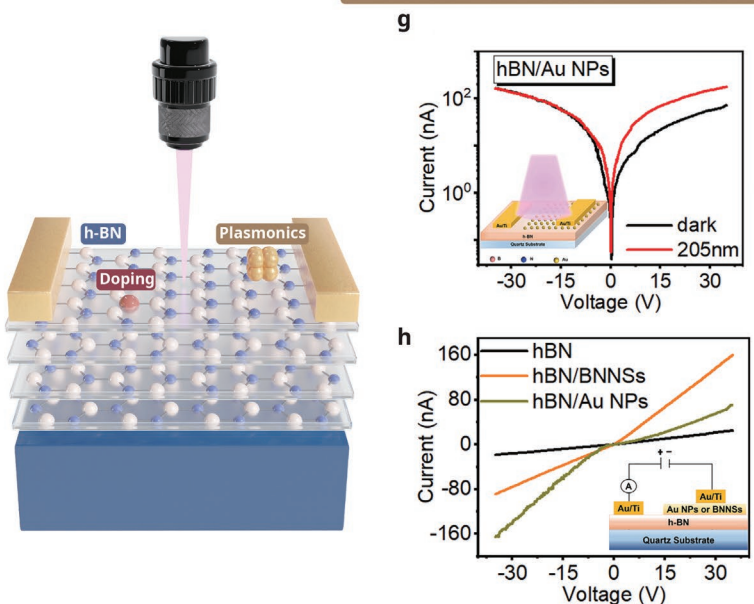


Figure 12. a) The semilogarithmic I/V curves of the h-BN photodetectors in the dark and under a 212 nm illumination at a power density of 6.4 mW cm^{-2} . Reproduced with permission.^[166] Copyright 2021, Wiley-VCH. b) The on/off ratio for Sample A and Sample D based photodetectors. Sample A as the reference indicates the h-BN layer without nitridation, Ar⁺ sputtering and Sample D indicates the h-BN layer with the combination of surface nitridation and N⁺ sputtering. Adapted with permission.^[167] Copyright 2019, Royal Society of Chemistry. c) The photoresponse of h-BN photodetector based on Sample D for the rise and decay times. Reproduced with permission.^[167] Copyright 2019, Royal Society of Chemistry. d) The photocurrents and dark currents from S1-based and S5-based photodetectors on the applied voltages. S1 indicates as-grown h-BN and S5 indicates h-BN layer annealed in N₂ ambient at 1700 °C for 10 min. Reproduced with permission.^[168] Copyright 2022, Elsevier. e) The on/off ratio and responsivity related to the C content calculated at 20 V. Reproduced with permission.^[169] Copyright 2022, American Chemical Society. f) The column diagram of photocurrent and responsivity of h-BN and S-doped h-BN photodetectors under a 280 nm light irradiation. Reproduced with permission.^[170] Copyright 2022, American Chemical Society. g) The semilogarithmic I/V curves of the h-BN photodetector with Au NPs under the dark and a 205 nm illumination at a power density of 19 mW cm^{-2} with the applied bias from -35 to 35 V. Reproduced with permission.^[172] Copyright 2022, AIP Publishing. h) The dark currents of the h-BN photodetector and h-BN hybrid devices. Reproduced with permission.^[172] Copyright 2022, AIP Publishing.

nano photonics with its inherent hyperbolic properties in the IR region.^[180] In h-BN, the strong coupling between phonons and IR photons produces hybrid quasiparticles and phonon polaritons.^[181] Due to the layered and anisotropic structure of h-BN, h-BN exhibits two separate optical phonon branches originating from the in-plane (TO phonons) and the out-of-plane (LO phonons) lattice vibrations.^[27] The polar character of h-BN breaks the degeneracy of LO and TO phonons, resulting in two spectrally distinct regions referred to as the lower Reststrahlen band ($\approx 760\text{--}825 \text{ cm}^{-1}$) and the upper Reststrahlen band ($1360\text{--}1620 \text{ cm}^{-1}$) between separated LO and TO phonon frequencies, where the

permittivities are hyperbolic.^[182-184] The hyperbolicity causes unique physical properties that the sign of permittivity along in-plane directions is opposite to that along with the out-of-plane directions, and the directional propagation of hyperbolic phonon polaritons is confined to sub-wavelength dimensions like in a metal.^[185,186] Since these natural hyperbolic properties of h-BN were first demonstrated in 2014,^[183,184] a broad range of nano photonic applications of h-BN in the IR region have been offered including hyperlensing,^[187,188] metasurface-based optical components via the surface-enhanced IR absorption effect,^[189-191] free carrier injection,^[192-194] and electromagnetic hybrids.^[22,195]

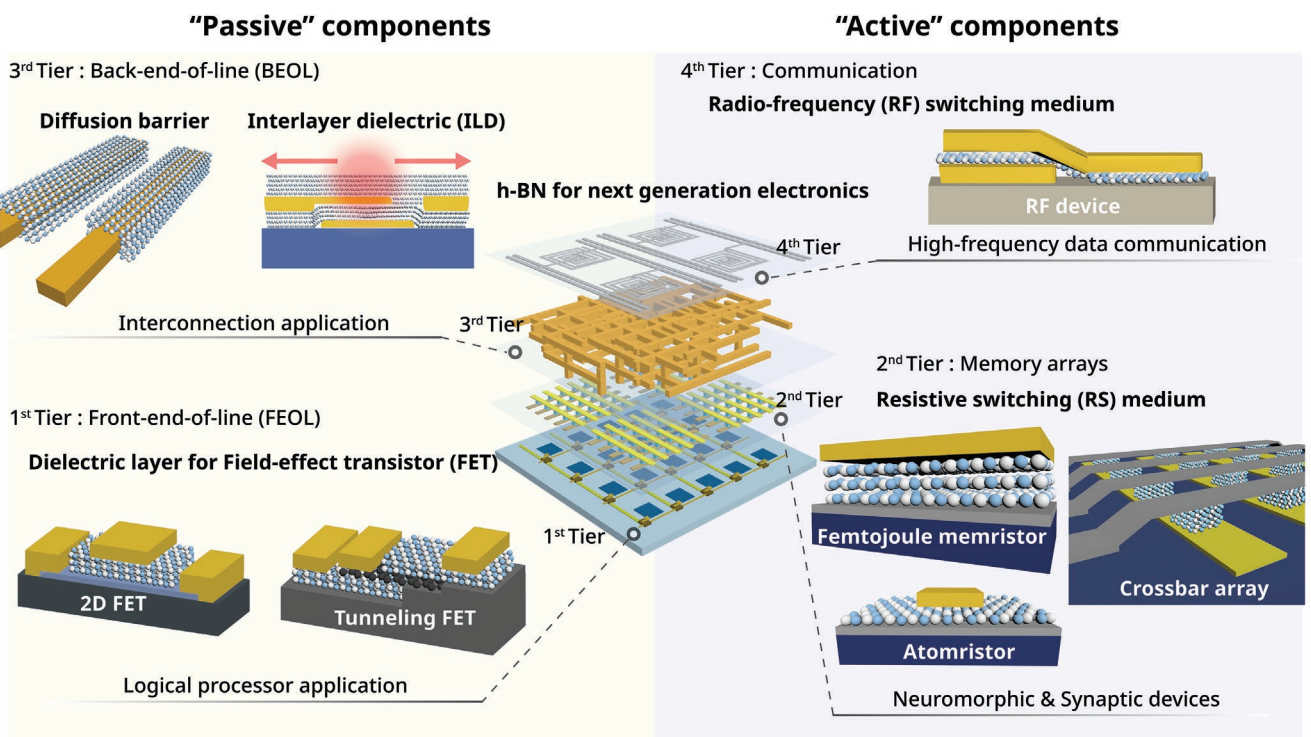


Figure 13. Schematic description of current 3D integrated electronics in which h-BN can be utilized both for passive and active components.

4. h-BN for Next-Generation Electronics

h-BN is a prospective 2D insulating material that can be utilized for overcoming the physical limits encountered by the scaling of CMOS and monolithic 3D integration of current electronics technologies. Figure 13 schematically shows potential applications of h-BN in a 3D integration where multiple tiers including processors, memories, interconnects, etc. are consecutively stacked, as multifunctional passive components as well as active layers for emerging devices. As multifunctional passive components, h-BN is a very promising candidate for dielectric layers of various FETs for enhanced performances in the front-end-of-line, sub-nm diffusion barriers for interconnect technology, and ILD for excellent electrical isolation and heat management in the back-end-of-line. On the other hand, h-BN is a prospective candidate for active layers of RS memory toward energy-efficient neuromorphic devices and RF devices for advanced wireless data communications with terahertz frequency range.

4.1. Passive Components for Electronic Devices

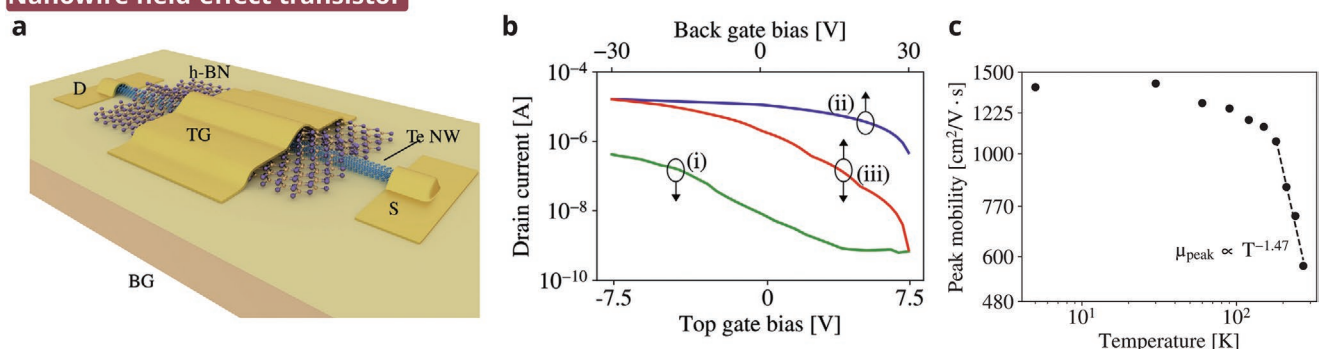
4.1.1. Dielectric Layer for FETs

FETs are essential building blocks for modern CMOS technology.^[196] Conventional FETs are fabricated from conventional 3D bulk materials, including silicon, oxides, and nitrides. These materials face several challenges as devices continually shrink in size. For example, as the thickness of the gate oxide layer decreases, subthreshold leakage at the gate is aggravated, and carrier mobility of the channel is severely degraded.^[197] As the

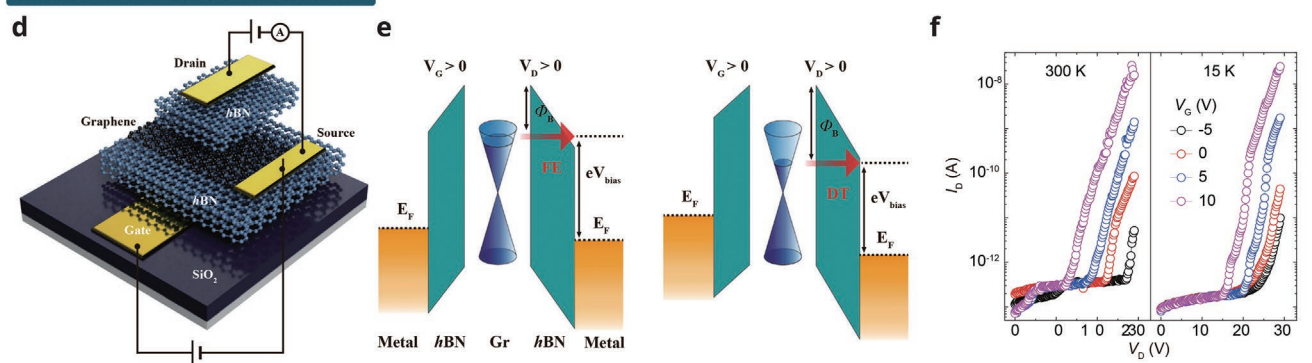
representative 2D dielectric material, h-BN is a promising candidate to replace conventional oxides and nitrides, overcoming the challenges from CMOS scaling. The ultraflat and dangling bond-free nature of h-BN can improve the performance of gate dielectric layers,^[198,199] and the carrier mobility of the channel underlying the gate can be enhanced because h-BN can effectively screen the effects of phonons and charged impurities.^[200–202] Inserting monolayer h-BN between a semiconducting channel and a metal contact can also decrease the contact resistance of the source/drain by modulating the Schottky barrier.^[203,204] Accordingly, many studies on employing h-BN for emerging FETs have been conducted. Recently, emerging FETs for CMOS electronics have been presented, including the nanowire field-effect transistor (NWFET) and the tunnel field-effect transistor (TFET). These devices are expected to realize denser integration, faster-switching speed, and lower energy consumption thanks to their novel structures and working principles beyond conventional FETs.^[205] The utilization of h-BN in these emerging FETs as an excellent dielectric layer will play a key role in advancing next-generation electronics.

Nanowire Field-Effect Transistors: NWFET is one of the emerging FET devices where semiconducting nanowire works as the channel. For NWFET, the electrostatic control of the current in the nanowire channel can be effectively and tightly modulated by the gate dielectrics surrounding the nanowire. Therefore, the short-channel effect can be reduced, and denser integration of devices can be achieved. For these reasons, NWFET has attracted attention as a future device that replaces fin field-effect transistor.^[206–208] Dasika et al. demonstrated the dual-gated junctionless NWFET using tellurium (Te) nanowire as the channel and multilayer h-BN as the top gate dielectric

Nanowire field-effect transistor



Tunnel field-effect transistor



Floating-gate field-effect transistor

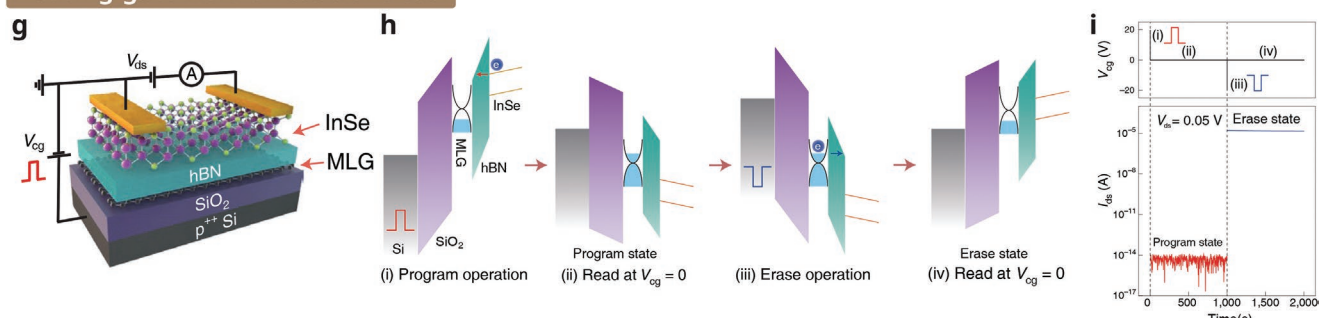


Figure 14. Emerging FET devices using h-BN dielectric layer. a) Schematic illustration of the dual-gated junctionless NWFET with h-BN gate encapsulated Te nanowire channel. b) Transfer characteristics for individual-gating and dual-gating at $V_D = -1.2$ V. Dual-gating (iii) provides an on/off ratio of 2×10^4 , but top (i) or bottom-gating (ii) alone is only around 10^2 . c) Plot of peak hole mobility as a function of temperature. The highest hole mobility of $1390 \text{ cm}^2 \text{ V}^{-1} \text{ s}^{-1}$ was achieved at 5 K. a–c) Reproduced with permission.^[209] Copyright 2021, Wiley-VCH. d) Schematic illustration of the semiconductor-less TFET based on h-BN/graphene/h-BN vertical heterostructure. e) Schematic energy band diagram and the switching principle of TFET device for positive V_G and V_D . FE-dominant (left) and DT-dominant (right) operations are performed through the h-BN tunneling layer. f) Output characteristics of the semiconductor-less TFET at 300 K (left) and 15 K (right). Both plots show analogous temperature-independent characteristics. d–f) Reproduced under the terms of the CC-BY Creative Commons Attribution 4.0 International license (<https://creativecommons.org/licenses/by/4.0/>).^[215] Copyright 2021, The Authors, published by Springer Nature. g) Schematic illustration of ultrafast nonvolatile memory based on FGFET with h-BN tunnel dielectric. h) Schematic energy band diagram and working principle of FGFET for the program, erase and read operations. h-BN functions as tunnel dielectric with MLG floating-gate. i) Program and erase operation with a high extinction ratio of 10^{10} of FGFET. Voltage pulses of $+17.7$ and -17.7 V with FWHM of 160 ns were applied. g–i) Adapted with permission.^[218] Copyright 2021, The Authors, published by Springer Nature.

(Figure 14a).^[209] 15 nm-thick h-BN was transferred to Te nanowires by a dry transfer method. Because of its chiral nature, the Te nanowire channel forms an ideal dangling bond-free interface with the h-BN gate dielectric. Such an interface can mitigate the degradation of the channel current, resulting in the current on/off ratio of over 2×10^4 and the on-current density of $216 \mu\text{A } \mu\text{m}^{-1}$ (Figure 14b). In addition, the hole mobility

of $570 \text{ cm}^2 \text{ V}^{-1} \text{ s}^{-1}$, which is higher than that of state-of-the-art strained Si mobility,^[210] was achieved at 270 K, and the mobility was increased to $1390 \text{ cm}^2 \text{ V}^{-1} \text{ s}^{-1}$ at 5 K (Figure 14c).

Tunnel Field-Effect Transistors : The TFET is an FET that conducts switching with tunneling phenomena, unlike conventional FETs. It can exhibit low power consumption and overcome the subthreshold swing of $60 \text{ mV decade}^{-1}$. It is also

expected to improve the current on/off ratio and achieve superior performance due to lower off-current.^[211,212] h-BN can be exploited as a switching layer of TFET due to its outstanding tunneling capabilities.^[79,213,214] Lee et al. reported the unprecedented semiconductor-less TFET based on vertical heterostructure of metal/h-BN/graphene/h-BN/metal (Figure 14d).^[215] The switching behavior of the device is based on two tunneling mechanisms, field emission (FE) and direct tunneling (DT),^[196] through the h-BN layer. h-BN/graphene heterostructure was introduced because its clean and smooth interface, makes it a suitable platform for uniform tunneling.^[216] The gate bias (V_G) and drain bias (V_D) modulate the Fermi level of graphene and the tunneling barrier height (Φ_B), allowing FE and DT to control the channel current (Figure 14e). When the Fermi level of graphene is located at the energy level of the h-BN tunneling barrier, it exhibits the FE-dominant current that depends on Φ_B exponentially, whereas when the Fermi level of graphene decreases and Φ_B increases, it exhibits the DT-dominant current. The device shows distinct switching behavior at $V_D = 14$ V by the current changing from DT regime to FE regime with increasing V_D , and a high current on/off ratio close to 10^6 . Moreover, due to the temperature-independent nature of the FE tunneling, the channel current (I_D) manifests analogous output characteristics at both 300 and 15 K (Figure 14f). It also maintained nearly constant performance without degradation from 15 up to 400 K.

Floating-Gate Field-Effect Transistors: Floating-gate field-effect transistor (FGFET) is considered as an indispensable component of nonvolatile memory, where the floating-gate operates as memory cells that store charges.^[217] h-BN is a promising tunnel dielectric material to replace conventional oxides for FGFET. Indeed, ultrafast FGFETs based on h-BN have recently been achieved. Wu et al. demonstrated the ultrafast nonvolatile memory based on FGFET comprising indium selenide (InSe)/h-BN/multilayer graphene (MLG) vdW heterostructures.^[218] InSe, h-BN, and MLG layers function as a channel, tunnel dielectric, and floating-gate, respectively (Figure 14g). The working principles of the program, erase, and read operations are depicted in Figure 14h. When a positive pulse ($V_{cg} > 0$) is applied to the control gate, electrons at the InSe channel tunnel through the h-BN layer, and are stored in the MLG floating-gate, which is a program operation. The electrons remain stored in the MLG even when the electric field caused by the gate voltage is removed, so the InSe channel has low conductance at $V_{cg} = 0$. This state can be read as program state. Conversely, when a negative pulse ($V_{cg} < 0$) is applied to the control gate, electrons stored at the MLG floating-gate can tunnel through the h-BN layer and migrate back to InSe, which is an erase operation. Since the InSe channel has a high conductance at $V_{cg} = 0$, this state can be read as an erase state. The defect-free h-BN tunnel dielectric and atomically sharp interfaces of vdW heterostructures contribute to achieving outstanding performances. The devices represent a high extinction ratio of 10^{10} (Figure 14i), indicating the feasibility of a multilevel memory cell. The triple- and the quadruple-level cells were demonstrated through the stepwise drain current (I_{ds}) by applying different numbers of positive pulses, with 13.5 and 16 nm-thick h-BN, respectively. Furthermore, program and erase operations were successfully performed with ultrafast voltage pulses of

21 ns. The long retention time of 16.5 days and endurance of 2000 cycles were accomplished due to the excellent insulating performance of h-BN as an efficient high opaque barrier for electrons stored in graphene. Liu et al. also demonstrated an FGFET device with an h-BN tunnel dielectric and a molybdenum disulfide (MoS₂) channel.^[219] Tunnel currents due to Fowler–Nordheim (FN) tunneling at the h-BN/MoS₂ heterostructure were calculated to be consistent with the experimental results. The device exhibits ultrafast write and erase speeds of 20 ns with the nonvolatile operation. They also claimed that the steep energy band of h-BN/MoS₂ heterostructure can enhance the appearance of the tunneling electrons due to FN tunneling, and produce large tunnel currents that can result in ultrafast write and erase operations.

4.1.2. Diffusion Barrier for Interconnection

The nanoscale copper (Cu) interconnection inevitably requires an atomically thin, sub-nm scale diffusion barrier for suppressing Cu diffusion, which cannot be achieved by using conventional diffusion barriers, such as tantalum nitride (Ta_N).^[220–222] 2D layered materials such as graphene,^[223–231] h-BN,^[228,232–236] and TMDs^[228,233–234,237–239] have been considered as reliable ultrathin diffusion barriers. The strong in-plane covalent bonding in 2D materials effectively blocks the diffusion of interconnection metallic atoms with large atomic radii.^[228,229,231,235–237] Figure 15a compares the diffusion energy barrier of single-crystalline 2D materials and TaN, showing that especially graphene and h-BN have much higher energy barriers for diffusion than TaN.^[236]

Lo et al. evaluated h-BN diffusion barrier properties through electrical, structural, and chemical analyses, and provided intuitive evidence of excellent suppression of Cu diffusion by h-BN and a dramatic improvement of SiO₂ dielectric lifetimes as shown in Figure 15b,c.^[234] Recently, first-principles calculations have been employed to compare the capability of Cu diffusion through 2D materials with defects.^[228,235] Ahmed et al. investigated the diffusion barrier performance of graphene, h-BN, and MoS₂ having a monovacancy defect where a Cu atom geometrically adsorbed (Figure 15d).^[228] As shown in Figure 15e, the MoS₂–V_{2s} defect site shows the highest energy barrier of 3.39 eV among the 2D materials, whereas the MoS₂–V_{Mo} site shows the lowest barrier energy. This result infers that the Cu atoms can easily penetrate through the MoS₂–V_{Mo} site in MoS₂ layer. On the other hand, the energy barriers of h-BN–V_B and h-BN–V_N are 2.24 and 1.4 eV, respectively, higher than those of Gr–V_c and MoS₂–V_{Mo}, indicating that h-BN has superior diffusion barrier performance compared to other 2D materials (Figure 15e).

4.1.3. Interlayer Dielectric

Monolithic 3D integration, as schematically shown in Figure 16a, involves consecutively stacked devices and circuits with interconnects and ILDs.^[84,240] The ILDs, essential components to isolate the interconnects, must have low relative dielectric constants (k) against the electrical interference between the interconnects, excellent thermal management capabilities,

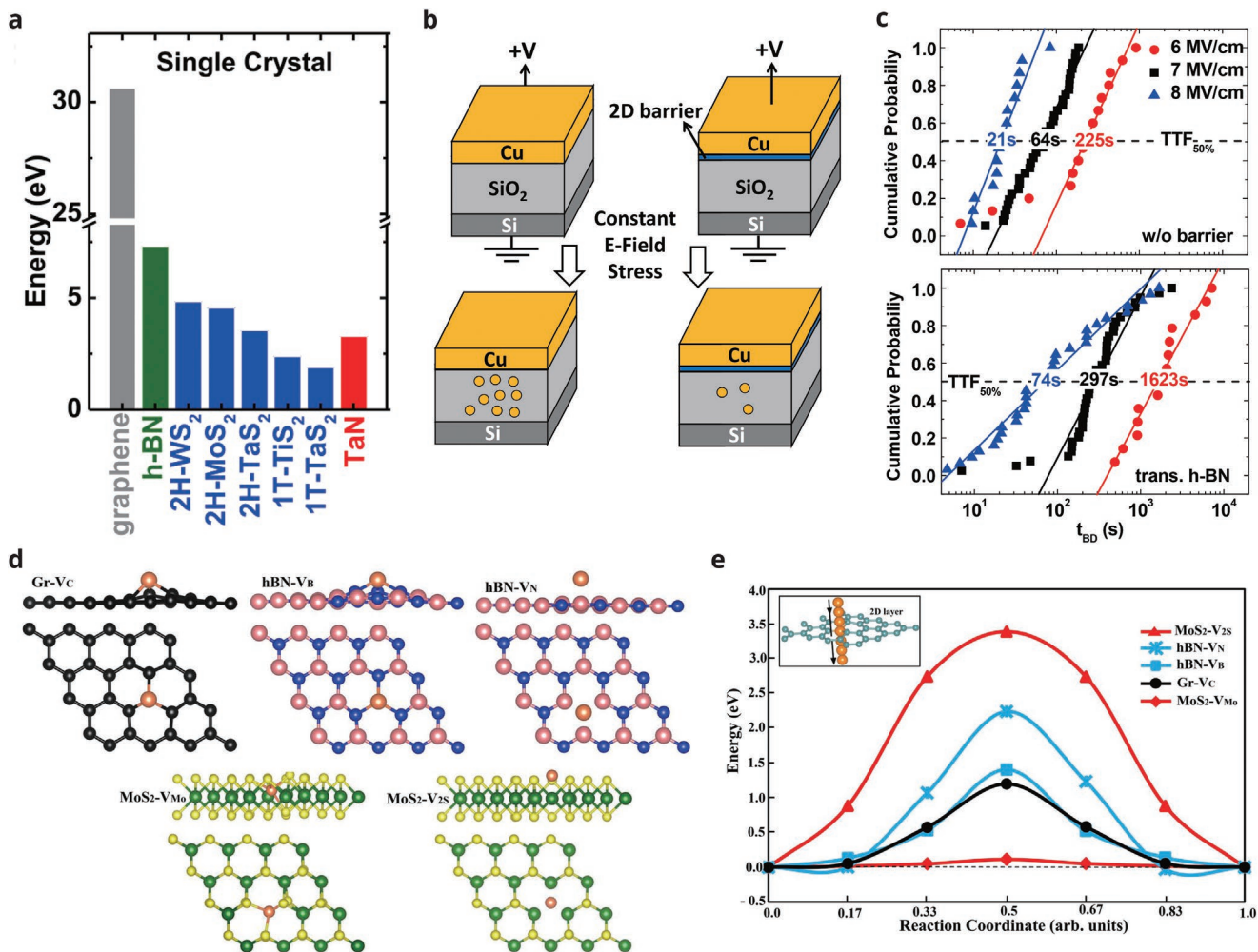


Figure 15. a) Summary of diffusion barrier energies of single-crystal 2D materials and conventional TaN diffusion barrier. Reproduced with permission.^[236] Copyright 2020, AIP Publishing. b) A series of schematic illustrations of MOS capacitors used for h-BN barrier property evaluation. c) Time-dependent dielectric breakdown (TDDB) results at the various electrical field with and without the h-BN barrier. Each data point means the breakdown time of a single MOS capacitor. TTF_{50%} represents the median-time-to-failure which is a probability of 0.5 indicating the device reliability. b,c) Reproduced under the terms of the CC-BY Creative Commons Attribution 4.0 International license (<https://creativecommons.org/licenses/by/4.0/>).^[234] Copyright 2017, The Authors, published by Springer Nature. d) Top and side views for the most stable configurations of Cu atom adsorbed 2D materials in terms of graphene, h-BN, and MoS₂. e) The diffusion energy barrier of Cu atom through graphene, h-BN, and MoS₂. The diffusion energy barrier gradually increases as Cu atom approaches to the vacancy defect site. d,e) Reproduced with permission.^[228] Copyright 2022, IOP Publishing.

and chemically and mechanically stable features. Until now, the International Technology Roadmap for Semiconductors (ITRS) predictions for implementation of low-*k* materials indicate the several times delay due to the difficulties in the integration process of porous low-*k* materials.^[241]

The 3D integration with an atomically thin h-BN layer can dramatically reduce the ILD thickness and also provide a solution to overcoming the major drawback of the current architecture in terms of RC (resistance–capacitance) delay, chip-overheating, and chemical and thermal instability.^[84] Although crystalline h-BN and its compounds possess relatively low dielectric constants (Figure 16b,^[241] *k*: 3–5), these values do not meet the recommendation of ITRS (*k* < 2). Recently, the exceptionally low dielectric constant of the BN layer has been reported. As shown in Figure 16c, Ahmed et al. reported an unusual reduction in effective dielectric constant at high frequency (up to

100 MHz) by employing a time domain reflectometry.^[242] Hong et al. also demonstrated that the randomly oriented amorphous BN (a-BN) has an ultralow *k* value of 1.16 at high frequencies of 1 MHz (Figure 16d).^[243] The ultralow *k* a-BN is an unprecedented low-*k* material with additional excellent performance that satisfies almost all criteria of ILD such as thermal, chemical, and mechanical stability.

On the other hand, the atomically thin nature and remarkable thermal transport property of h-BN are favorable for effective heat dissipation, resulting in lower thermal resistance in 3D integration. Contrary to very low thermal conductivity values of conventional low-*k* materials (under 1.6 W m⁻¹ K⁻¹ as shown in Figure 16e),^[244] h-BN demonstrates excellent thermal conductivity (monolayer in-plane thermal conductivity \approx 751 W m⁻¹ K⁻¹), as discussed in Section 2.3.2. Also, as shown in Figure 16f,^[84] the out-of-plane h-BN thermal conductance,

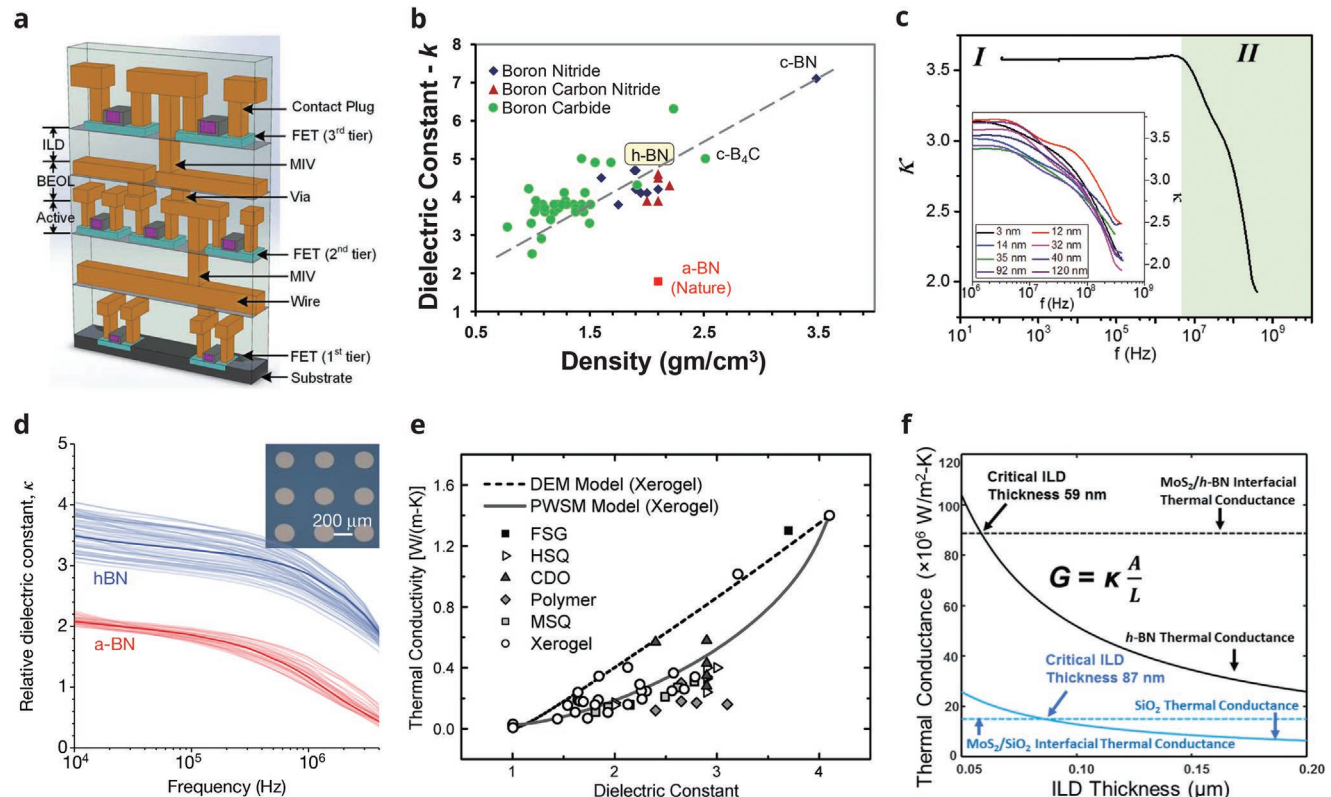


Figure 16. a) Schematic of monolithic 3D integration with ILD. Reproduced with permission.^[240] Copyright 2018, IEEE. b) Mass density versus dielectric constant of h-BN and its compounds. Adapted with permission.^[241] Copyright 2020, IEEE. c) Calculated dielectric constant of h-BN as a function of frequency (up to 100 MHz). Reproduced with permission.^[242] Copyright 2018, Wiley-VCH. d) Relative dielectric constant as a function of frequency compared between a-BN and h-BN. Reproduced with permission.^[243] Copyright 2020, The Authors, published by Springer Nature. e) Thermal conductivity of conventional low- κ materials and the correlation between thermal conductivity and dielectric constant. Reproduced with permission.^[244] Copyright 2005, IEEE. f) Comparison of out-of-plane thermal conductance (normalized by the area, G/A) of h-BN and conventional SiO₂ dielectric. Reproduced under the terms of the CC-BY Creative Commons Attribution 4.0 International license (<https://creativecommons.org/licenses/by/4.0/>).^[84] Copyright 2019, The Authors, published by IEEE.

which is a critical factor for heat management in 3D integration is superior to conventional SiO₂ dielectric, which makes atomically thin BN a very promising ILD for the next-generation electronics.

4.2. Active Components for Electronic Devices

4.2.1. Resistive Switching Medium

Memristors with nonvolatile RS memories,^[245–247] which can modulate the resistance between different states depending on the external electrical stress, are regarded as emerging next-generation digital information storage and advanced computing system due to their excellent performance in terms of low power consumption,^[248,249] fast speed operation,^[250,251] and high density.^[249,252,253] However, the conventional RS memory devices using transition metal oxides as the RS medium have several challenges such as poor reliability and variability, and difficulty in scaling down to nano- or even sub-nanolevels in the vertical direction.^[254–256]

h-BN-based RS memory devices have been considered as promising candidates to overcome the challenges of current

oxide-based RS devices. h-BN possesses great advantages as an active RS medium thanks to its extraordinary physical properties: i) h-BN is the only wide-bandgap (≈ 6 eV) 2D material that ensures an extremely low current level in high resistive states (HRS) and a high current on/off ratio.^[257–261] ii) Atomically thin nature of h-BN can lead to ultrafast switching speed, low energy consumption, and high-density 3D integration.^[260,262–270] iii) The high breakdown strength and low variability of h-BN can improve device reliability and variability.^[257,260,271–273] iv) Excellent thermal and chemical stabilities provide sustainable operation in HRS and low resistive states (LRS) under long continuous electrical stress.^[270,274,275] With these tremendous benefits, Qian et al. introduced the first RS memory devices based on CVD-grown h-BN on a flexible PET substrate (Figure 17a), showing long retention time, reproducible endurance properties, and the capability to operate under extreme bending tests.^[276] With this study as a starting momentum, considerable research in h-BN-based RS memory devices with different switching types (unipolar (Figure 17b),^[261,266,275,277] bipolar (Figure 17c),^[257–261,264–268,270–288] and threshold switching (Figure 17d)^[257,260,265,270,277,280,287] has been carried out with different electrode materials and thickness of h-BN. Pan et al. revealed the coexistence of bipolar and threshold RS types

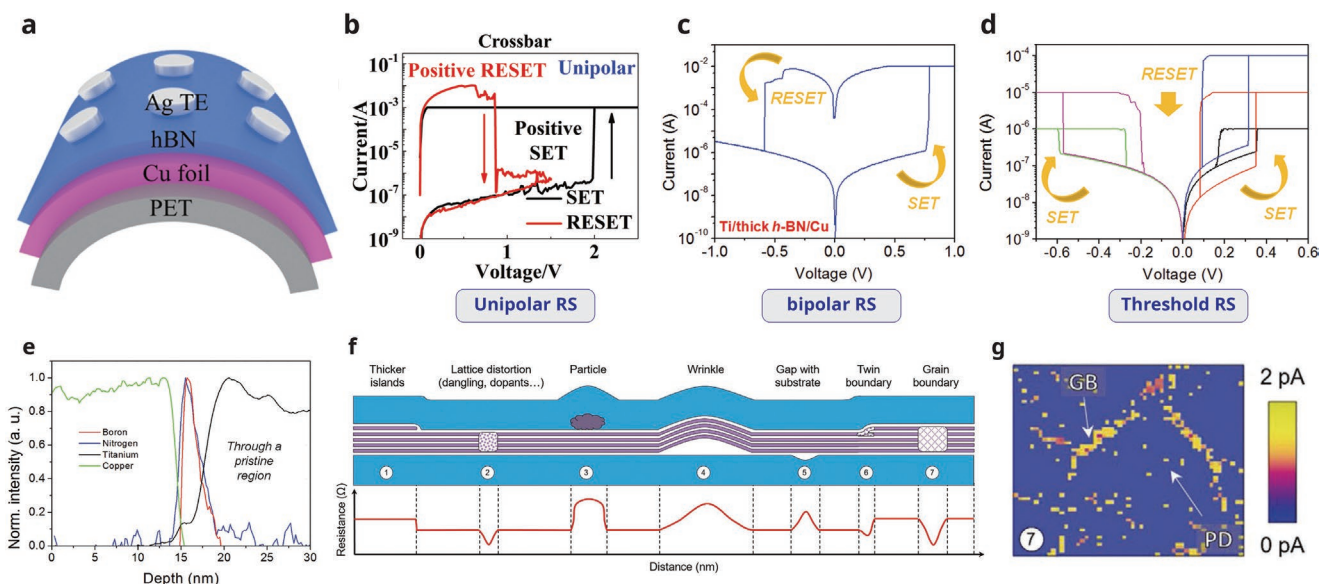


Figure 17. a) Schematic of flexible Ag/h-BN/Cu RS memory devices. Reproduced with permission.^[276] Copyright 2016, Wiley-VCH. b) Unipolar RS behavior in monolayer h-BN. Reproduced with permission.^[266] Copyright 2019, Wiley-VCH. c,d) Coexistence of bipolar RS (c) and threshold RS types (d) in Ti/thick h-BN/Cu device structure. e) EELS cross-sectional analyses of grain boundary-conductive filament locations. f,g) Reproduced with permission.^[257] Copyright 2017, Wiley-VCH. f) Schematic of a transferred h-BN on the bottom electrode and their resistance (1) thickness variation, (2) localized defects, rests of (3) polymer particles and (4) wrinkles from the transfer process, (5) suspended h-BN, (6) twin boundaries, and (7) grain boundaries. (1), (3), (4), (5) increase the local out-of-plane resistance and (2), (6), (7) reduce the resistance. g) Current map at the grain boundaries (GB) and point defects (PD) collected with the conductive AFM. Grain boundary and point defects increase the out-of-plane local current flow. f,g) Reproduced with permission.^[272] Copyright 2021, Wiley-VCH.

shown in Figure 17c,d^[257] in multilayer h-BN depending on the current compliance, opening the door for electronic synaptic application.^[265] Due to the high thermal and chemical stability and reliability of the h-BN RS medium, the threshold RS switches back from the LRS to the HRS without any electrical stress. They revealed that the RS is driven by the migration of B and the penetration of Ti ion into the h-BN grain boundaries by using the electron energy loss spectroscopy profiles at grain boundary regions, as shown in Figure 17e.^[257]

Nevertheless, there is still uncertainty about the origin of defects influencing the switching mechanism in h-BN RS devices. Recently, Shen et al. reported a comprehensive analysis of each type of defect which impacts on the RS memory switching.^[272] They claimed the defects in h-BN, created during the transfer process such as wrinkles, particles, and polymer residue, have no remarkable effect on the performance of h-BN-based memristors. Whereas incorporated particles, wrinkles, and gaps with substrate increase the local out-of-plane resistance of the sample, twin boundaries and grain boundaries reduce the resistance of h-BN (Figure 17f). Figure 17g shows the current maps where the leakage current flows preferentially across the grain boundaries and local defect sites. The highly conductive defective sites can mainly generate the path of conductive filament and promote the RS phenomenon.

Recently, many efforts have been made to enhance the performance of h-BN-based RS memories, taking great advantages offered by h-BN, including h-BN atomristor with fast switching speed and excellent reliability, femtojoule energy-efficient memristive devices, and large area memristive crossbar array, as shown in Figure 18.^[256]

h-BN Atomristors: The precise scaling of the thickness of RS medium is crucial for the performance of filamentary type memristors in terms of operating current, Set/Reset voltage, switching speed, and energy consumption. The thickness of transition metal oxide switching material is restricted to above few nanometers due to excessive leakage current and processing limitations. h-BN atomristor,^[266] an RS memory device with monolayer h-BN layer, was first demonstrated, showing nonvolatile switching with a large current on/off ratio ($\approx 10^7$), as shown in Figure 18a,b. Recently, Nikam et al. reported the quantized conductance atomic threshold switch (QCATS) by using monolayer h-BN that has atomic-scale conductive filaments (CFs).^[270] With precise control of single atomic-scale CF, excellent performance with low operation voltage of ≈ 0.3 V, low off-state current of 1 pA, fast switching speed of 50 ns (Figure 18c), and good endurance under $\approx 10^7$ AC cycles, was realized.

Energy-efficient femtojoule memristive devices: The current requirement of energy consumption for RS memory is known as ≈ 10 pJ per transition, calling for highly energy-efficient memristive devices for the next-generation neuromorphic applications. Zhao et al. demonstrated an oxidative h-BN-based femtojoule thinnest device (total device thickness ≈ 60 nm) with sub-pA operation current by minimizing the thickness of the filamentary switching medium (0.9 to 2.3 nm) as shown in Figure 18d.^[264] Furthermore, lately, Shi et al. fabricated multi-layer h-BN-based synaptic devices.^[265] The volatile and nonvolatile resistive switching can emulate the energy-efficient short-term and long-term plasticity. The power consumption of the volatile RS in Ag/h-BN/Au synapses is 0.1 fW in standby and 600 pW per transition due to an extremely lower level of HRS

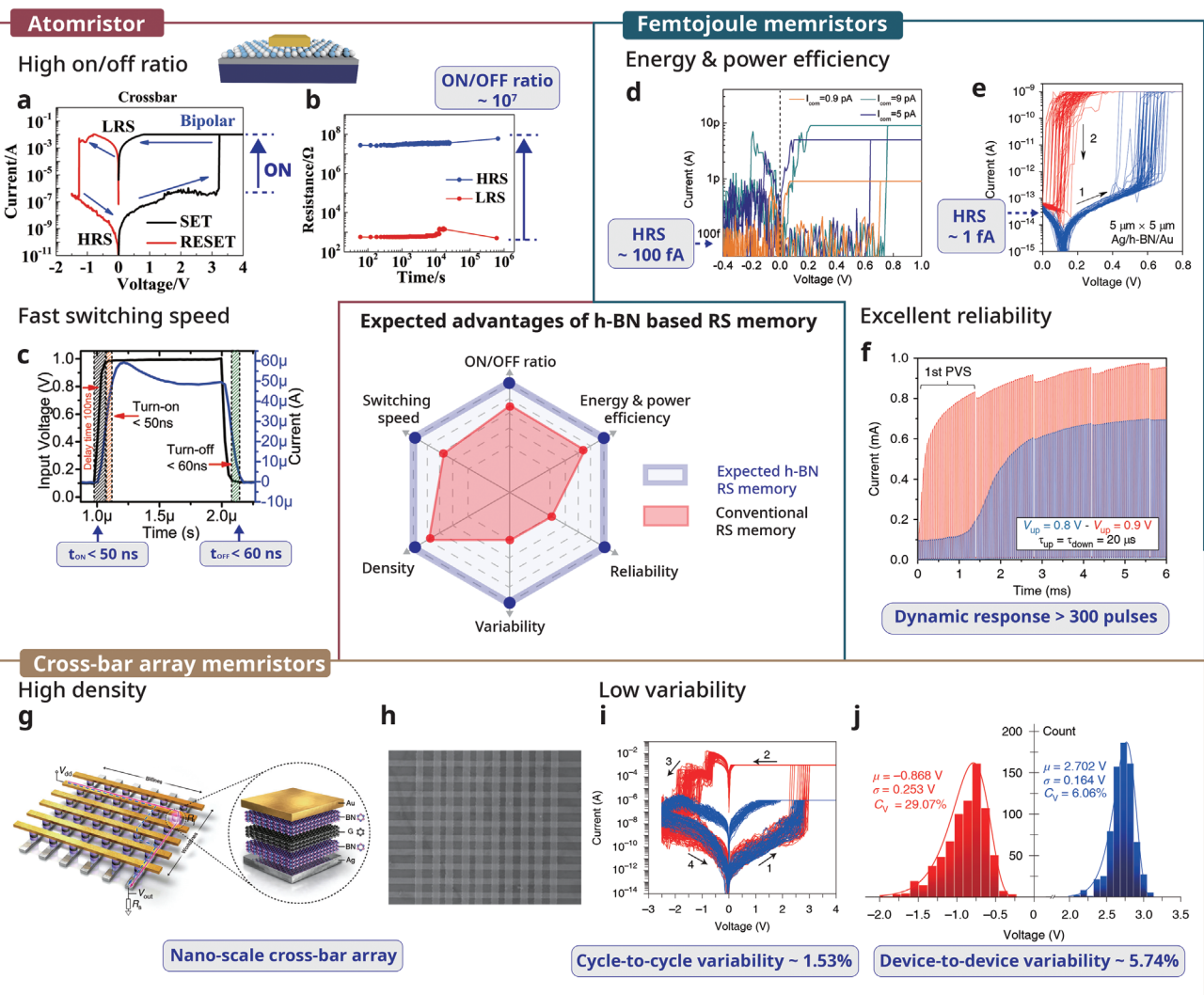


Figure 18. a) The bipolar RS behavior of monolayer h-BN with high current on/off ratio ($\approx 10^7$). b) The retention time of h-BN atomistor indicating stable retention over a week at room temperature. The resistance of HRS and LRS is determined by the read voltage at 0.1 V. a,b) Adapted with permission.^[266] Copyright 2019, Wiley-VCH. c) Operation speed and delay time of hBN-QCATS device using AC pulses ($t_{on} < 50$ ns and $t_{off} < 60$ ns). Adapted with permission.^[270] Copyright 2021, Wiley-VCH. d) I–V characteristics of atomically thin (≈ 0.9 nm) BNO_x switching layer with very low HRS current level (≈ 10 – 100 fA) at different current compliances of 0.9, 5, and 9 pA. Reproduced with permission.^[264] Copyright 2017, Wiley-VCH. e) Volatile Ag/15–18 layer h-BN/Au synapses with very low HRS current level (≈ 1 fA). The power consumption in standby and the power per set transition is about 0.1 fW and 600 pW, respectively. f) Dynamic response of cross-point Au/Ti/5–7-layer h-BN/Au synapses by applying two sequences of 4 pulsed voltage stresses (PVS) with 30 pulses each. Progressive synapse potentiation with different voltage up (V_{up} , 0.8 V (blue) and 0.9 V (red)). The voltage down (V_{down}) is identical to 0.1 V and the time up and down (τ_{up} and τ_{down}) is 20 μ s. e,f) Reproduced with permission.^[265] The Authors, published by Copyright 2018, Springer Nature. g) Schematic image of the vdW heterostructure (h-BN/graphene/h-BN) in the crossbar memory array architecture. Reproduced under the terms of the CC-BY Creative Commons Attribution 4.0 International license (<https://creativecommons.org/licenses/by/4.0/>).^[258] Copyright 2019, The Authors, published by Springer Nature. h) Scanning electron microscopy (SEM) image of a crossbar array containing 750 nm \times 750 nm Ag/h-BN/Ag memristors. i) I–V characteristics of bipolar RS in Au/h-BN/Au memristors measure during 120 cycles at different current compliance (I_{cc}), including a yield of $\approx 98\%$. The graph shows the low cycle to cycle variability. The blue and red lines indicate I_{cc} of 1 μ A and 1 mA, respectively. j) Cumulative distribution of 48 devices indicating low device to device variability of about 5.75% ($I_{cc} = 1$ mA). h–j) Reproduced with permission.^[260] Copyright 2020, The Authors, published by Springer Nature.

current (Figure 18e) with ultrafast switching times (< 10 ns). Moreover, the h-BN-based synapses show a stable relaxation during 300 pulses when exposed to sequential pulsed voltage stresses (Figure 18f). These high-performance electronic synapses can lead to the significant advance toward future energy-efficient brain-like computing.

Large-Scale Crossbar Arrays: The concept of the crossbar array plays an important role in hardware-amenable memory and

energy-efficient neuromorphic application. A large-scale h-BN-based crossbar array can provide a major technological breakthrough overcoming current limitations in low device yield, high device-to-device variability, large sneak current, low selectivity, and poor reliability. As shown in Figure 18g, Sun et al. introduced a self-selective crossbar array containing unique architecture by forming h-BN/graphene/h-BN vdW heterostructure.^[258] The two h-BN switching media provide both volatile and

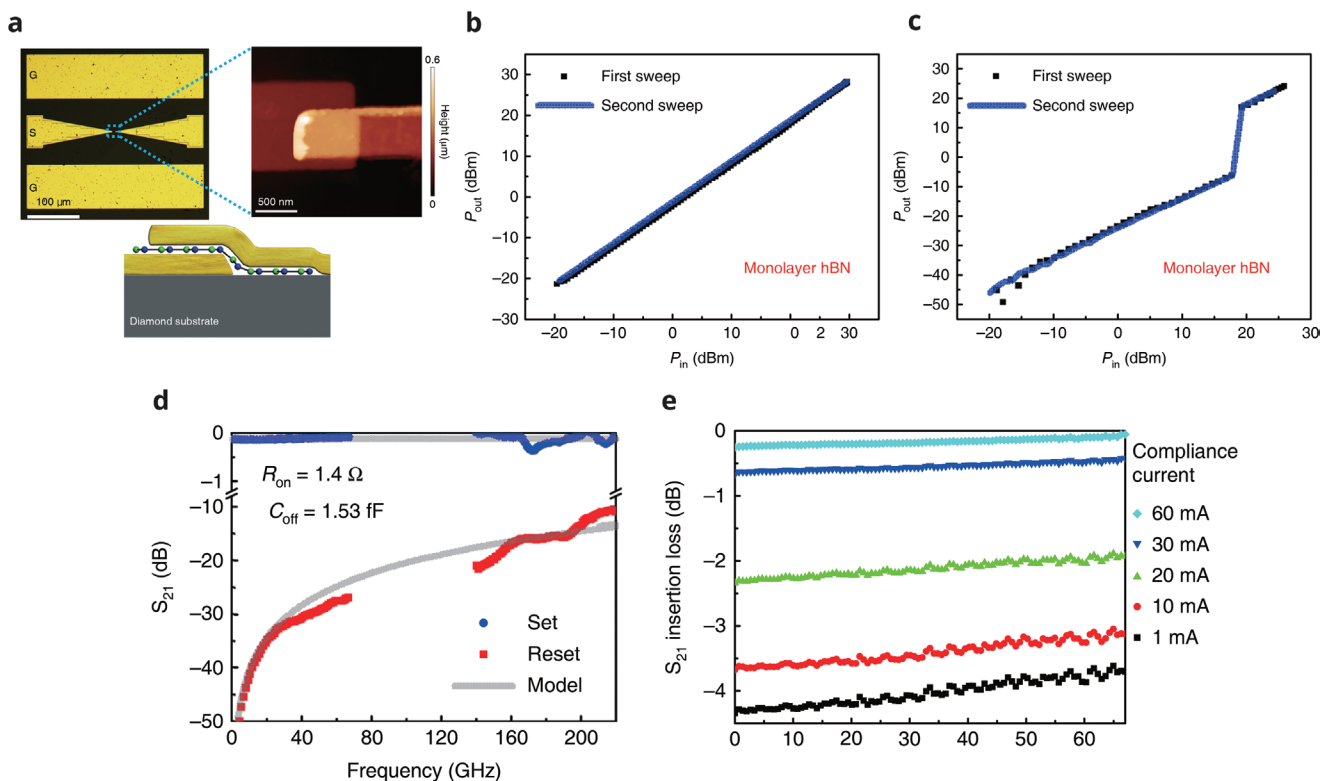


Figure 19. a) Optical microscopy, AFM image, and schematic image of fabricated monolayer h-BN RF device. b,c) The power handling of h-BN-based RF device: b) ON-state and c) OFF-state at 40 GHz. The OFF-state shows the self-switching at about 20 dBm. d) High-frequency performance of h-BN RF device. Measured high-frequency scattering (S_{21})-parameter and model data in both the ON-state and OFF-state of h-BN-based RF device into the terahertz range. The h-BN-based RF device shows an insertion loss of less than 0.5 dB and isolation higher than 10 dB. e) Analogous switching characteristics of h-BN RF device. The ON-state resistance depending on switching compliance current. a–e) Reproduced with permission.^[291] Copyright 2020, The Authors, published by Springer Nature.

nonvolatile switchings in one cell with ultralow off-state current and excellent endurance against the high on-state current. The crossbar array architecture with vdW heterostructure resolved the key restriction of large sneak current, demonstrating outstanding self-selectivity ($\approx 10^{10}$) and a high on/off resistance ratio ($> 10^3$). Analogously, Chen et al. reported the wafer-scale and high-density crossbar array using CVD-grown multilayer h-BN for neuromorphic devices, shown in Figure 18h.^[260] The h-BN-based crossbar array demonstrated nonvolatile bipolar switching and volatile threshold switching behaviors with Au and Ag electrodes, respectively. Memristors with both switching types presented outstanding performance with high device yield (above 98%), and ultralow variability (cycle-to-cycle $\approx 1.53\%$ and device-to-device $\approx 5.75\%$) as shown in Figure 18i,j. These outstanding capabilities of the h-BN memristor are superior to state-of-the-art conventional oxide-based devices. Furthermore, the h-BN crossbar arrays show the feasible potential of high-performance artificial neural network applications.

4.2.2. RF Switching Medium

The wireless communication field is seeking beyond silicon-based devices, operating at wide frequency bands with low energy consumption. 2D materials-based RF devices have

attracted increasing attention as promising candidates for energy-efficient terahertz communication systems with extraordinarily high data processing speed and excellent transportability.^[289–296] Until now, 2D materials-based RF devices have been demonstrated with thin-film transistors (TFTs) including graphene,^[297–299] TMDs,^[300–302] and black phosphorus^[292,303] as channel layers, which are volatile switches and consume both dynamic and static energy.

Recently, it was reported that 2D materials-based RF devices with a metal–insulator–metal (MIM) structure can be operated with high energy efficiency due to nonvolatile memory characteristics maintaining the current state without any voltage stress.^[290] Atomic scale thickness of 2D materials enables lower ON-state resistance (R_{on}) of under 5 Ω , avoiding parasitic insertion losses, while keeping low OFF-state capacitance (C_{off}) by reducing the device area for isolation. Kim et al. first investigated nonvolatile RF devices with monolayer h-BN in a simple MIM structure (Figure 19a).^[291,294] Compared to other 2D materials-based RF devices, the h-BN-based RF device exhibits excellent power handling, which means it can transmit the high maximum power (up to 30 dBm) during the ON-state, while retaining high isolation in the OFF-state (around 20 dBm) as shown in Figure 19b,c. In addition, the h-BN-based RF device presents a cutoff-frequency ($F_{co} = 1/2\pi R_{on} C_{off}$) of around 129 THz with a low insertion loss (≤ 0.5 dB) and high isolation

(≥ 10 dB), as shown in Figure 19d. Furthermore, as shown in Figure 19e, the correlation between compliance current and R_{on} of the h-BN-based RF device suggests the possibility for non-volatile tunable memory devices with programmable resistance states.

5. Conclusion

We have highlighted the most recent discoveries of extraordinary properties of h-BN including the effect of the stacking sequences and structural anisotropy of h-BN on optical and electrical properties, and both theoretical and experimental evidences elucidating unique light absorption and emission, as well as excellent dielectric breakdown and thermal properties. Being the only wide-bandgap semiconductor among 2D vdW materials family, h-BN is a very promising candidate for the active layers in both light emission and detection in wide spectral ranges, from DUV to visible region, despite its indirect-bandgap nature. The combination of strong exciton–phonon coupling, high exciton binding energy, and short radiative lifetime makes h-BN a very promising active material in a variety of photonics applications. First, h-BN-based DUV light emitters can replace AlGaN-based DUV LEDs thanks to their exceptionally high IQE comparable to direct-bandgap semiconductors and effective extraction of DUV photons. Due to its strong band-edge absorption with a short absorption tail, h-BN-based DUV photodetectors exhibit superior visible-blind DUV photo-detection. In addition, point defects in h-BN are bright sources for single-photon emission at room temperature from NIR to NUV. Recent studies on h-BN have also shown superior breakdown strength, unprecedented reliability and variability, and exceptionally high thermal conductivity even with sub-nanometer thickness compared to conventional dielectrics, showing very promising potential to be used in both active and passive components for next-generation electronics applications. We discussed recent results on RS memories and RF devices with excellent performances where h-BN layers were used as active components, as well as remarkable advancements in conventional passive applications of h-BN such as insulators for FETs, effective diffusion barrier, and low- k ILD.

Despite notable advances being achieved recently, there are remaining technical challenges toward real-world applications at an industrial level. The large-area synthesis of multilayer h-BN with excellent crystallinity is the most significant challenge. Small microscale h-BN flakes exfoliated from high-purity h-BN crystals were used in most of studies described in this review. Mechanical exfoliation is an inherently random process, with which h-BN flakes with suitable thickness, size, and shape should be selected and transferred, makes it incompatible with the standard industrial microelectronic processes. As a scalable growth method, CVD of h-BN on catalytic substrates such as Cu, Ni, and Fe, has been widely used to grow wafer-scale single-crystalline monolayer h-BN. In addition to CVD, organic chemical vapor deposition, molecular beam epitaxy, and atomic layer deposition have been introduced for epitaxial growth of single crystal multilayer h-BN films in a large scale. Unlike CVD method, relying on the catalytic effect of metallic substrates, thus the transfer of grown h-BN onto a target substrate

is necessary, these growth techniques allow for direct growth of h-BN on various large-area substrates including sapphire and SiO₂, making them very suitable for creating vertically stacked heterostructures by growth, and for ensuring the compatibility with current Si-based microelectronics processes. Integration of h-BN and other 2D materials with Si-based CMOS technology will lead to a huge impact on breaking the downscaling limit with conventional materials, enhancing the performance and the functionality of Si chips for photonic-integrated circuits, neuromorphic computing, and quantum-solid technologies. However, the growth temperature of h-BN is still too high for standard CMOS processes, which should be addressed for the realization of highly performing active and passive components for next-generation 2D/3D hybrid and eventually all-2D devices.

Besides high-crystallinity and low-defect h-BN growth, the synthesis of h-BN with precisely controlled crystallinity, defects, and impurities would be very beneficial, but is challenging. With controlled surface chemistry, structural geometry, and growth conditions, h-BN could be grown with desired molecular structure, stacking, orientation, strain, and defect density, making it possible to tune their electrical, optical, and magnetic properties on demand. For example, h-BN with high crystallinity is required for an enhanced switching performance of FETs and an effective diffusion barrier, however, h-BN layers with controlled defects density and crystallinity can promote RS phenomena and result in exceptionally ultralow dielectric constant for ILD materials, respectively. Controlling the number of layers or staking sequences results in remarkable change in the electronic band structure, thus, in electrical and optical properties, which can be utilized to explore new functionalities of h-BN. Electrical doping of h-BN, either by replacing atoms in the h-BN crystal lattice with impurity atoms, defects, or molecular adsorbates, remains a big challenge. Exploring suitable atoms forming shallow levels near the conduction and the valence bands, and the methods of incorporating them on predetermined area of h-BN in a precisely controlled and deterministic way will make a huge impact on enhancing the performance and expanding the functionality of h-BN.

For h-BN based devices, we strongly believe that there is a huge room for further improvements in performance and reliability of emerging next-generation photonics and electronics technologies. Although h-BN exhibits counterintuitive, bright PL and CL emission and excellent absorption properties despite its indirect bandgap, h-BN-based DUV EL emitters, SPEs, and DUV photodetectors are still in their infancy with efficiencies much lower than theoretically expected. Rapid progress in the performance of both electronics and photonic devices can be made by adopting the lessons learned from conventional 3D devices, for example, though improved carrier injection, suppression of carrier leakage, and reduction of contact resistance by choosing an appropriate contact material or doping.

Acknowledgements

This work was supported by Samsung Electronics Co., Ltd (I0210520-08650-01 and I0210707-08808-01), the Technology Innovation Program (Grant No. 20016290, development of sub-micrometer blue color light source for modular display) funded by the Ministry of Trade, Industry & Energy (MOTIE, Korea), and National Research Foundation

of Korea (NRF) grant funded by the Korean Government (NRF-2021M3C1C3097673, NRF-2018H1A2A1060392, and NRF-2018-Global Ph.D. Fellowship Program).

Conflict of Interest

The authors declare no conflict of interest.

Author Contributions

S.M. and J.K. contributed equally to this work. J.K.K. led this work, and designed the review structure. S.M. led the drafting of the manuscript and contributed to the structural and optical properties of h-BN and next-generation photonics, J.K. contributed to the electrical and thermal properties of h-BN and next-generation electronics, J.P. developed the light emitter in DUV region section, S.I. developed the single-photon emitter section, J.K. developed the DUV photodetectors section, and I.H. developed the dielectric layer for field-effect transistors section. All authors participated in the discussion, review, and editing of the entire article content.

Keywords

2D materials, electronics, hexagonal boron nitride, optoelectronics, photonics

Received: May 9, 2022

Revised: June 14, 2022

Published online: December 30, 2022

- [1] K. S. Novoselov, A. K. Geim, S. V. Morozov, D. Jiang, Y. Zhang, S. V. Dubonos, I. V. Grigorieva, A. A. Firsov, *Science* **2004**, 306, 666.
- [2] K. S. Novoselov, A. K. Geim, S. V. Morozov, D. Jiang, M. I. Katsnelson, I. V. Grigorieva, S. V. Dubonos, A. A. Firsov, *Nature* **2005**, 438, 197.
- [3] Y. Zhang, Y.-W. Tan, H. L. Stormer, P. Kim, *Nature* **2005**, 438, 201.
- [4] M. Yankowitz, Q. Ma, P. Jarillo-Herrero, B. J. LeRoy, *Nat. Rev. Phys.* **2019**, 1, 112.
- [5] K. Yao, N. R. Finney, J. Zhang, S. L. Moore, L. Xian, N. Tancogne-Dejean, F. Liu, J. Ardelean, X. Xu, D. Halbertal, *Sci. Adv.* **2021**, 7, 8691.
- [6] K. Novoselov, A. Mishchenko, A. Carvalho, A. C. Neto, *Science* **2016**, 353, 9439.
- [7] M. Gibertini, M. Koperski, A. F. Morpurgo, K. S. Novoselov, *Nat. Nanotechnol.* **2019**, 14, 408.
- [8] X. Wang, F. Xia, *Nat. Mater.* **2015**, 14, 264.
- [9] R. Frisenda, E. Navarro-Moratalla, P. Gant, D. P. De Lara, P. Jarillo-Herrero, R. V. Gorbachev, A. Castellanos-Gomez, *Chem. Soc. Rev.* **2018**, 47, 53.
- [10] J. Cheng, C. Wang, X. Zou, L. Liao, *Adv. Opt. Mater.* **2019**, 7, 1800441.
- [11] Q. Zeng, Z. Liu, *Adv. Electron. Mater.* **2018**, 4, 1700335.
- [12] W. Zhang, Q. Wang, Y. Chen, Z. Wang, A. T. Wee, *2D Mater.* **2016**, 3, 022001.
- [13] Q. H. Wang, K. Kalantar-Zadeh, A. Kis, J. N. Coleman, M. S. Strano, *Nat. Nanotechnol.* **2012**, 7, 699.
- [14] M. Shayegan, *Nat. Rev. Phys.* **2022**, 4, 212.
- [15] Y. K. Ryu, R. Frisenda, A. Castellanos-Gomez, *Chem. Commun.* **2019**, 55, 11498.
- [16] G. Cassabois, P. Valvin, B. Gil, *Nat. Photonics* **2016**, 10, 262.
- [17] C. R. Dean, A. F. Young, I. Meric, C. Lee, L. Wang, S. Sorgenfrei, K. Watanabe, T. Taniguchi, P. Kim, K. L. Shepard, *Nat. Nanotechnol.* **2010**, 5, 722.
- [18] D. Pacile, J. Meyer, Ç. Girit, A. Zettl, *Appl. Phys. Lett.* **2008**, 92, 133107.
- [19] S. Roy, X. Zhang, A. B. Puthirath, A. Meiyazhagan, S. Bhattacharya, M. M. Rahman, G. Babu, S. Susarla, S. K. Saju, M. K. Tran, L. M. Sassi, M. Saadi, J. Lai, O. Sahin, S. M. Sajadi, B. Dharmarajan, D. Salpekar, N. Chakingal, A. Baburaj, X. Shuai, A. Adumbumkulath, K. A. Miller, J. M. Gayle, A. Ajnsztajn, T. Prasankumar, V. V. J. Harikrishnan, V. Ojha, H. Kannan, A. Z. Khater, Z. Zhu, et al., *Adv. Mater.* **2021**, 33, 2101589.
- [20] K. Zhang, Y. Feng, F. Wang, Z. Yang, J. Wang, *J. Mater. Chem. C* **2017**, 5, 11992.
- [21] T. T. Tran, K. Bray, M. J. Ford, M. Toth, I. Aharonovich, *Nat. Nanotechnol.* **2016**, 11, 37.
- [22] A. Woessner, M. B. Lundeberg, Y. Gao, A. Principi, P. Alonso-González, M. Carrega, K. Watanabe, T. Taniguchi, G. Vignale, M. Polini, *Nat. Mater.* **2015**, 14, 421.
- [23] N. Nikolay, N. Mendelson, E. Özeltci, B. Sontheimer, F. Böhm, G. Kewes, M. Toth, I. Aharonovich, O. Benson, *Optica* **2019**, 6, 1084.
- [24] R. Camphausen, L. Marini, S. A. Tawfik, T. T. Tran, M. J. Ford, S. Palomba, *APL Photonics* **2020**, 5, 076103.
- [25] R. Bourrellier, S. Meuret, A. Tararan, O. Stephan, M. Kociak, L. H. Tizei, A. Zobelli, *Nano Lett.* **2016**, 16, 4317.
- [26] K. K. Kim, H. S. Lee, Y. H. Lee, *Chem. Soc. Rev.* **2018**, 47, 6342.
- [27] J. D. Caldwell, I. Aharonovich, G. Cassabois, J. H. Edgar, B. Gil, D. Basov, *Nat. Rev. Mater.* **2019**, 4, 552.
- [28] Y. Gong, Z.-Q. Xu, D. Li, J. Zhang, I. Aharonovich, Y. Zhang, *ACS Energy Lett.* **2021**, 6, 985.
- [29] M. J. Molaei, M. Younas, M. Rezakazemi, *ACS Appl. Electron. Mater.* **2021**, 3, 5165.
- [30] R. R. Wills, *Int. J. High Technol. Ceram.* **1985**, 1, 139.
- [31] L. Vel, G. Demazeau, J. Etourneau, *Mater. Sci. Eng., B* **1991**, 10, 149.
- [32] F. R. Corrigan, F. P. Bundy, *J. Chem. Phys.* **1975**, 63, 3812.
- [33] C. Chen, D. Yin, T. Kato, T. Taniguchi, K. Watanabe, X. Ma, H. Ye, Y. Ikuhara, *Proc. Natl. Acad. Sci. USA* **2019**, 116, 11181.
- [34] A. Segura, R. Cuscó, T. Taniguchi, K. Watanabe, G. Cassabois, B. Gil, L. Artús, *J. Phys. Chem. C* **2019**, 123, 20167.
- [35] M. Topsakal, E. Aktürk, S. Ciraci, *Phys. Rev. B* **2009**, 79, 115442.
- [36] S. M. Gilbert, T. Pham, M. Dogan, S. Oh, B. Shevitski, G. Schumm, S. Liu, P. Ercius, S. Aloni, M. L. Cohen, *2D Mater.* **2019**, 6, 021006.
- [37] M. Chubarov, H. Höglberg, A. Henry, H. Pedersen, *J. Vac. Sci. Technol., A* **2018**, 36, 030801.
- [38] S. Hong, C.-S. Lee, M.-H. Lee, Y. Lee, K. Y. Ma, G. Kim, S. I. Yoon, K. Ihm, K.-J. Kim, T. J. Shin, *Nature* **2020**, 582, 511.
- [39] T. T. Tran, C. Elbadawi, D. Totonjian, C. J. Lobo, G. Grossi, H. Moon, D. R. Englund, M. J. Ford, I. Aharonovich, M. Toth, *ACS Nano* **2016**, 10, 7331.
- [40] G. Grossi, H. Moon, B. Lienhard, S. Ali, D. K. Efetov, M. M. Furchi, P. Jarillo-Herrero, M. J. Ford, I. Aharonovich, D. Englund, *Nat. Commun.* **2017**, 8, 705.
- [41] T. Q. P. Vuong, G. Cassabois, P. Valvin, S. Liu, J. H. Edgar, B. Gil, *Phys. Rev. B* **2017**, 95, 201202.
- [42] L. Schué, L. Sponza, A. Plaud, H. Bensalah, K. Watanabe, T. Taniguchi, F. Ducastelle, A. Loiseau, J. Barjon, *Phys. Rev. Lett.* **2019**, 122, 067401.
- [43] D. Wickramaratne, L. Weston, C. G. Van de Walle, *J. Phys. Chem. C* **2018**, 122, 25524.
- [44] C. Elias, G. Fugallo, P. Valvin, C. L'Henoret, J. Li, J. Edgar, F. Sottile, M. Lazzeri, A. Ouerghi, B. Gil, *Phys. Rev. Lett.* **2021**, 127, 137401.

- [45] C. Elias, P. Valvin, T. Pelini, A. Summerfield, C. Mellor, T. Cheng, L. Eaves, C. Foxon, P. Beton, S. Novikov, *Nat. Commun.* **2019**, *10*, 2639.
- [46] S. F. Chichibu, Y. Ishikawa, H. Kominami, K. Hara, *J. Appl. Phys.* **2018**, *123*, 065104.
- [47] S. Roux, C. Arnold, F. Paleari, L. Sponza, E. Janzen, J. H. Edgar, B. Toury, C. Journet, V. Garnier, P. Steyer, *Phys. Rev. B* **2021**, *104*, L161203.
- [48] P. J. Dean, D. C. Herbert, in *Excitons*, (Ed.: K. Cho), Springer, Berlin/Heidelberg, Germany **1979**, pp. 55–182.
- [49] G. Cassabois, G. Fugallo, C. Elias, P. Valvin, A. Rousseau, B. Gil, A. Summerfield, C. Mellor, T. Cheng, L. Eaves, *Phys. Rev. X* **2022**, *12*, 011057.
- [50] A. Rousseau, L. Ren, A. Durand, P. Valvin, B. Gil, K. Watanabe, T. Taniguchi, B. Urbaszek, X. Marie, C. Robert, *Nano Lett.* **2021**, *21*, 10133.
- [51] K. Watanabe, T. Taniguchi, H. Kanda, *Nat. Mater.* **2004**, *3*, 404.
- [52] Y. Toyozawa, *Prog. Theor. Phys.* **1958**, *20*, 53.
- [53] B. Gil, D. Felbacq, B. Guizal, G. Bouchitté, *Phys. Status Solidi B* **2012**, *249*, 455.
- [54] G. Cassabois, P. Valvin, B. Gil, *Phys. Rev. B* **2016**, *93*, 035207.
- [55] K. Watanabe, T. Taniguchi, T. Kuroda, O. Tsuda, H. Kanda, *Diamond Relat. Mater.* **2008**, *17*, 830.
- [56] Y. Li, Y. Rao, K. F. Mak, Y. You, S. Wang, C. R. Dean, T. F. Heinz, *Nano Lett.* **2013**, *13*, 3329.
- [57] A. Rousseau, P. Valvin, W. Desrat, L. Xue, J. Li, J. H. Edgar, G. Cassabois, B. Gil, *ACS Nano* **2022**, *16*, 2756.
- [58] G. A. Reider, T. F. Heinz, in *Photonic Probes of Surfaces*, (Ed: P. Halevi), *Electromagnetic Waves: Recent Developments in Research*, Elsevier, Amsterdam, The Netherlands **1995**, pp. 413–478.
- [59] C.-J. Kim, L. Brown, M. W. Graham, R. Hovden, R. W. Havener, P. L. McEuen, D. A. Muller, J. Park, *Nano Lett.* **2013**, *13*, 5660.
- [60] L. Sponza, H. Amara, C. Attaccalite, S. Latil, T. Galvani, F. Paleari, L. Wirtz, F. Ducastelle, *Phys. Rev. B* **2018**, *98*, 125206.
- [61] A. Laturia, M. L. Van de Put, W. G. Vandenberghe, *npj 2D Mater. Appl.* **2018**, *2*, 6.
- [62] Y. Hattori, T. Taniguchi, K. Watanabe, K. Nagashio, *ACS Nano* **2015**, *9*, 916.
- [63] J. W. McPherson, K. Jinyoung, A. Shanware, H. Mogul, J. Rodriguez, *IEEE Trans. Electron Devices* **2003**, *50*, 1771.
- [64] Y. Hattori, T. Taniguchi, K. Watanabe, K. Nagashio, *ACS Appl. Mater. Interfaces* **2016**, *8*, 27877.
- [65] R. Degraeve, G. Groeseneken, R. Bellens, J. L. Ogier, M. Depas, P. J. Roussel, H. E. Maes, *IEEE Trans. Electron Devices* **1998**, *45*, 904.
- [66] F. Palumbo, C. Wen, S. Lombardo, S. Pazos, F. Aguirre, M. Eizenberg, F. Hui, M. Lanza, *Adv. Funct. Mater.* **2020**, *30*, 1900657.
- [67] A. Ranjan, N. Raghavan, M. Holwill, K. Watanabe, T. Taniguchi, K. S. Novoselov, K. L. Pey, S. J. O’Shea, *ACS Appl. Electron. Mater.* **2021**, *3*, 3547.
- [68] A. Ranjan, N. Raghavan, F. M. Puglisi, S. Mei, A. Padovani, L. Larcher, K. Shubhakar, P. Pavan, M. Bosman, X. X. Zhang, S. J. O’Shea, K. L. Pey, *IEEE Electron Device Lett.* **2019**, *40*, 1321.
- [69] A. Ranjan, N. Raghavan, S. J. O’Shea, S. Mei, M. Bosman, K. Shubhakar, K. L. Pey, in *2018 IEEE Int. Reliability Physics Symp. (IRPS)*, IEEE, Piscataway, NJ, USA **2018**, <https://doi.org/10.1109/IRPS.2018.8353574>.
- [70] A. Ranjan, S. J. O’Shea, M. Bosman, N. Raghavan, K. L. Pey, *ACS Appl. Mater. Interfaces* **2020**, *12*, 55000.
- [71] F. Hui, C. Pan, Y. Shi, Y. Ji, E. Grustan-Gutierrez, M. Lanza, *Microelectron. Eng.* **2016**, *163*, 119.
- [72] W. Weibull, *J. Appl. Mech.* **1951**, *18*, 293.
- [73] S. J. O’Shea, R. M. Atta, M. P. Murrell, M. E. Welland, *J. Vac. Sci. Technol., B: Nanotechnol. Microelectron.* **1995**, *13*, 1945.
- [74] J. Müller, P. Polakowski, S. Mueller, T. Mikolajick, *ECS J. Solid State Sci. Technol.* **2015**, *4*, N30.
- [75] M. M. Rahman, J. G. Kim, D. H. Kim, T. W. Kim, *Micromachines* **2019**, *10*, 361.
- [76] Y. Ji, C. Pan, M. Zhang, S. Long, X. Lian, F. Miao, F. Hui, Y. Shi, L. Larcher, E. Wu, M. Lanza, *Appl. Phys. Lett.* **2016**, *108*, 012905.
- [77] L. Jiang, Y. Shi, F. Hui, K. Tang, Q. Wu, C. Pan, X. Jing, H. Uppal, F. Palumbo, G. Lu, T. Wu, H. Wang, M. A. Villena, X. Xie, P. C. McIntyre, M. Lanza, *ACS Appl. Mater. Interfaces* **2017**, *9*, 39758.
- [78] Z. Cui, Y. He, H. Tian, A. Khanaki, L. Xu, W. Shi, J. Liu, *ACS Appl. Electron. Mater.* **2020**, *2*, 747.
- [79] G.-H. Lee, Y.-J. Yu, C. Lee, C. Dean, K. L. Shepard, P. Kim, J. Hone, *Appl. Phys. Lett.* **2011**, *99*, 243114.
- [80] D. Zhang, F. Wu, Q. Ying, X. Gao, N. Li, K. Wang, Z. Yin, Y. Cheng, G. Meng, *J. Mater. Chem. C* **2019**, *7*, 1871.
- [81] Y. Hattori, T. Taniguchi, K. Watanabe, K. Nagashio, *Appl. Phys. Lett.* **2016**, *109*, 253111.
- [82] Y. Hattori, T. Taniguchi, K. Watanabe, K. Nagashio, *Phys. Rev. B* **2018**, *97*, 045425.
- [83] H. Agarwal, B. Terrés, L. Orsini, A. Montanaro, V. Sorianello, M. Pantouvaki, K. Watanabe, T. Taniguchi, D. V. Thourhout, M. Romagnoli, F. H. L. Koppens, *Nat. Commun.* **2021**, *12*, 1070.
- [84] J. Jiang, K. Parto, W. Cao, K. Banerjee, *IEEE J. Electron Devices Soc.* **2019**, *7*, 878.
- [85] P. Jiang, X. Qian, R. Yang, L. Lindsay, *Phys. Rev. Mater.* **2018**, *2*, 064005.
- [86] Q. Cai, D. Scullion, W. Gan, A. Falin, S. Zhang, K. Watanabe, T. Taniguchi, Y. Chen, E. J. G. Santos, L. H. Li, *Sci. Adv.* **2019**, *5*, aav0129.
- [87] W. M. Haynes, D. R. Lide, T. J. Bruno, *CRC Handbook of Chemistry and Physics*, CRC Press, Boca Raton, FL, USA **2016**.
- [88] S.-M. Lee, D. G. Cahill, T. H. Allen, *Phys. Rev. B* **1995**, *52*, 253.
- [89] M. Hinz, O. Marti, B. Gotsmann, M. Lantz, U. Dürig, *Appl. Phys. Lett.* **2008**, *92*, 043122.
- [90] R. M. Costescu, A. J. Bullen, G. Matamis, K. E. O’Hara, D. G. Cahill, *Phys. Rev. B* **2002**, *65*, 094205.
- [91] A. Jain, S. Rogojevic, S. Ponoth, W. N. Gill, J. L. Plawsky, E. Simonyi, S.-T. Chen, P. S. Ho, *J. Appl. Phys.* **2002**, *91*, 3275.
- [92] A. Simpson, A. D. Stuckes, *J. Phys. C: Solid State Phys.* **1971**, *4*, 1710.
- [93] I. Jo, M. T. Pettes, J. Kim, K. Watanabe, T. Taniguchi, Z. Yao, L. Shi, *Nano Lett.* **2013**, *13*, 550.
- [94] M. T. Alam, M. S. Bresnahan, J. A. Robinson, M. A. Haque, *Appl. Phys. Lett.* **2014**, *104*, 013113.
- [95] H. Zhou, J. Zhu, Z. Liu, Z. Yan, X. Fan, J. Lin, G. Wang, Q. Yan, T. Yu, P. M. Ajayan, J. M. Tour, *Nano Res.* **2014**, *7*, 1232.
- [96] B. Mortazavi, L. F. C. Pereira, J. W. Jiang, T. Rabczuk, *Sci. Rep.* **2015**, *5*, 13228.
- [97] C. Wang, J. Guo, L. Dong, A. Aiyiti, X. Xu, B. Li, *Sci. Rep.* **2016**, *6*, 25334.
- [98] P. Jiang, X. Qian, R. Yang, *Rev. Sci. Instrum.* **2017**, *88*, 074901.
- [99] C. Yuan, J. Li, L. Lindsay, D. Cherns, J. W. Pomeroy, S. Liu, J. H. Edgar, M. Kuball, *Commun. Phys.* **2019**, *2*, 8.
- [100] X. Wu, Q. Han, *Comput. Mater. Sci.* **2020**, *184*, 109938.
- [101] H. Ying, A. Moore, J. Cui, Y. Liu, D. Li, S. Han, Y. Yao, Z. Wang, L. Wang, S. Chen, *2D Mater.* **2020**, *7*, 015031.
- [102] M. Kneissl, J. Rass, *III-Nitride Ultraviolet Emitters—Technology and Applications*, Springer, Berlin, Germany **2016**.
- [103] P.-J. J. Hargis, T.-J. Soering, G.-C. Tisone, J.-S. Wagner, *Proc. SPIE* **1995**, *2366*, 147.
- [104] W. Kowalski, *Ultraviolet Germicidal Irradiation Handbook*, Springer, Berlin, Germany **2009**.
- [105] D. Y. Kim, J. H. Park, J. W. Lee, S. Hwang, S. J. Oh, J. Kim, C. Sone, E. F. Schubert, J. K. Kim, *Light: Sci. Appl.* **2015**, *4*, 263.

- [106] K. B. Nam, M. L. Nakarmi, J. Li, J. Y. Lin, H. X. Jiang, *Appl. Phys. Lett.* **2003**, *83*, 878.
- [107] Y. Taniyasu, M. Kasu, *NTT Tech. Rev.* **2010**, *8*, 1.
- [108] J. E. Northrup, C. L. Chua, Z. Yang, T. Wunderer, M. Kneissl, N. M. Johnson, T. Kolbe, *Appl. Phys. Lett.* **2012**, *100*, 021101.
- [109] L. Schue, L. Sponza, A. Plaud, H. Bensalah, K. Watanabe, T. Taniguchi, F. Ducastelle, A. Loiseau, J. Barjon, *Phys. Rev. Lett.* **2019**, *122*, 067401.
- [110] S. Majety, X. K. Cao, J. Li, R. Dahal, J. Y. Lin, H. X. Jiang, *Appl. Phys. Lett.* **2012**, *101*, 051110.
- [111] T. Q. P. Vuong, G. Cassabois, P. Valvin, V. Jacques, A. V. D. Lee, A. Zobelli, K. Watanabe, T. Taniguchi, B. Gil, *2D Mater.* **2016**, *4*, 011004.
- [112] K. Watanabe, T. Taniguchi, T. Niizuma, K. Miya, M. Taniguchi, *Nat. Photonics* **2009**, *3*, 591.
- [113] K. Watanabe, T. Taniguchi, *Int. J. Appl. Ceram. Technol.* **2011**, *8*, 977.
- [114] S. H. Lee, H. Jeong, D. Y. Kim, S. Y. Seo, C. Han, O. F. N. Okello, J. I. Lo, Y. C. Peng, C. H. Oh, G. W. Lee, J. I. Shim, B. M. Cheng, K. Song, S. Y. Choi, M. H. Jo, J. K. Kim, *Opt. Express* **2019**, *27*, 19692.
- [115] S. H. Chae, J. Hone, D. Seo, J. Kwon, G.-H. Lee, H.-J. Choi, Q. Cao, X. Hua, I. P. Herman, E.-M. Shih, C. R. Dean, T. Taniguchi, K. Watanabe, D. Schiminovich, I. Kymmissis, Y. D. Kim, in *2019 Conf. on Lasers and Electro-Optics (CLEO)*, IEEE, Piscataway, NJ, USA **2019**, https://doi.org/10.1364/CLEO_SI.2019.SM10.2.
- [116] S. B. Song, S. Yoon, S. Y. Kim, S. Yang, S. Y. Seo, S. Cha, H. W. Jeong, K. Watanabe, T. Taniguchi, G. H. Lee, J. S. Kim, M. H. Jo, J. Kim, *Nat. Commun.* **2021**, *12*, 7134.
- [117] P. Jaffrennou, J. Barjon, J. S. Lauret, B. Attal-Trétout, F. Ducastelle, A. Loiseau, *J. Appl. Phys.* **2007**, *102*, 116102.
- [118] L. Museur, A. Kanaev, *J. Appl. Phys.* **2008**, *103*, 103520.
- [119] L. Museur, E. Feldbach, A. Kanaev, *Phys. Rev. B* **2008**, *78*, 155204.
- [120] T. Taniguchi, K. Watanabe, *J. Cryst. Growth* **2007**, *303*, 525.
- [121] G. Longo, M. G. La-Placa, M. Sessolo, H. J. Bolink, *ChemSusChem* **2017**, *10*, 3788.
- [122] Y. Kanemitsu, *J. Lumin.* **2002**, *100*, 209.
- [123] C. Jara, T. Rauch, S. Botti, M. A. L. Marques, A. Norambuena, R. Coto, J. E. Castellanos-Aguila, J. R. Maze, F. Munoz, *J. Phys. Chem. A* **2021**, *125*, 1325.
- [124] I. Aharonovich, D. Englund, M. Toth, *Nat. Photonics* **2016**, *10*, 631.
- [125] S. Gao, H.-Y. Chen, M. Bernardi, *npj Comput. Mater.* **2021**, *7*, 85.
- [126] M. Abdi, J.-P. Chou, A. Gali, M. B. Plenio, *ACS Photonics* **2018**, *5*, 1967.
- [127] S. A. Tawfik, S. Ali, M. Fronzi, M. Kianinia, T. T. Tran, C. Stampfl, I. Aharonovich, M. Toth, M. J. Ford, *Nanoscale* **2017**, *9*, 13575.
- [128] N. Mendelson, D. Chugh, J. R. Reimers, T. S. Cheng, A. Gottscholl, H. Long, C. J. Mellor, A. Zettl, V. Dyakonov, P. H. Beton, S. V. Novikov, C. Jagadish, H. H. Tan, M. J. Ford, M. Toth, C. Bradac, I. Aharonovich, *Nat. Mater.* **2021**, *20*, 321.
- [129] A. Sajid, K. S. Thygesen, *2D Mater.* **2020**, *7*, 031007.
- [130] P. Ares, H. Santos, S. Lazić, C. Gibaja, I. Torres, S. Pinilla, J. Gómez-Herrero, H. P. Meulen, P. García-González, F. Zamora, *Adv. Electron. Mater.* **2021**, *7*, 2001177.
- [131] C. Linderålv, W. Wieczorek, P. Erhart, *Phys. Rev. B* **2021**, *103*, 115421.
- [132] M. Mackoit-Sinkevičienė, M. Maciaszek, C. G. Van de Walle, A. Alkauskas, *Appl. Phys. Lett.* **2019**, *115*, 212101.
- [133] L. Weston, D. Wickramaratne, M. Mackoit, A. Alkauskas, C. G. Van de Walle, *Phys. Rev. B* **2018**, *97*, 214104.
- [134] M. Maciaszek, L. Razinkovas, A. Alkauskas, *Phys. Rev. Mater.* **2022**, *6*, 014005.
- [135] Z. Q. Xu, C. Elbadawi, T. T. Tran, M. Kianinia, X. Li, D. Liu, T. B. Hoffman, M. Nguyen, S. Kim, J. H. Edgar, X. Wu, L. Song, S. Ali, M. Ford, M. Toth, I. Aharonovich, *Nanoscale* **2018**, *10*, 7957.
- [136] J. C. Stewart, Y. Fan, J. S. H. Danial, A. Goetz, A. S. Prasad, O. J. Burton, J. A. Alexander-Webber, S. F. Lee, S. M. Skoff, V. Babenko, S. Hofmann, *ACS Nano* **2021**, *15*, 13591.
- [137] C. Fournier, A. Plaud, S. Roux, A. Pierret, M. Rosticher, K. Watanabe, T. Taniguchi, S. Buil, X. Quelin, J. Barjon, J. P. Hermier, A. Delteil, *Nat. Commun.* **2021**, *12*, 3779.
- [138] J. Ziegler, R. Klaiss, A. Blaikie, D. Miller, V. R. Horowitz, B. J. Aleman, *Nano Lett.* **2019**, *19*, 2121.
- [139] X. Xu, Z. O. Martin, D. Sychev, A. S. Lagutchev, Y. P. Chen, T. Taniguchi, K. Watanabe, V. M. Shalaev, A. Boltasseva, *Nano Lett.* **2021**, *21*, 8182.
- [140] J. A. Preuß, E. Rudi, J. Kern, R. Schmidt, R. Bratschitsch, S. Michaelis de Vasconcellos, *2D Mater.* **2021**, *8*, 035005.
- [141] A. W. Elshaari, A. Skalli, S. Gyger, M. Nurizzo, L. Schweickert, I. Esmaeil Zadeh, M. Svedendahl, S. Steinhauer, V. Zwiller, *Adv. Quantum Technol.* **2021**, *4*, 2100032.
- [142] Y. Xia, Q. Li, J. Kim, W. Bao, C. Gong, S. Yang, Y. Wang, X. Zhang, *Nano Lett.* **2019**, *19*, 7100.
- [143] G. Noh, D. Choi, J. H. Kim, D. G. Im, Y. H. Kim, H. Seo, J. Lee, *Nano Lett.* **2018**, *18*, 4710.
- [144] N. Mendelson, Z. Q. Xu, T. T. Tran, M. Kianinia, J. Scott, C. Bradac, I. Aharonovich, M. Toth, *ACS Nano* **2019**, *13*, 3132.
- [145] N. Mendelson, M. Doherty, M. Toth, I. Aharonovich, T. T. Tran, *Adv. Mater.* **2020**, *32*, 1908316.
- [146] C. Li, J. E. Fröch, M. Nonahal, T. N. Tran, M. Toth, S. Kim, I. Aharonovich, *ACS Photonics* **2021**, *8*, 2966.
- [147] S. Häußler, G. Bayer, R. Waltrich, N. Mendelson, C. Li, D. Hunger, I. Aharonovich, A. Kubanek, *Adv. Opt. Mater.* **2021**, *9*, 2002218.
- [148] J. E. Froch, S. Kim, N. Mendelson, M. Kianinia, M. Toth, I. Aharonovich, *ACS Nano* **2020**, *14*, 7085.
- [149] J. E. Froch, C. Li, Y. Chen, M. Toth, M. Kianinia, S. Kim, I. Aharonovich, *Small* **2022**, *18*, 2104805.
- [150] T. Vogl, R. Lecamwasam, B. C. Buchler, Y. Lu, P. K. Lam, *ACS Photonics* **2019**, *6*, 1955.
- [151] C. Li, Z.-Q. Xu, N. Mendelson, M. Kianinia, M. Toth, I. Aharonovich, *Nanophotonics* **2019**, *8*, 2049.
- [152] J. D. Caldwell, I. Aharonovich, G. Cassabois, J. H. Edgar, B. Gil, D. N. Basov, *Nat. Rev. Mater.* **2019**, *4*, 552.
- [153] T. Vogl, M. W. Doherty, B. C. Buchler, Y. Lu, P. K. Lam, *Nanoscale* **2019**, *11*, 14362.
- [154] I. H. Abidi, N. Mendelson, T. T. Tran, A. Tyagi, M. Zhuang, L. T. Weng, B. Özyilmaz, I. Aharonovich, M. Toth, Z. Luo, *Adv. Opt. Mater.* **2019**, *7*, 1900397.
- [155] N. Mendelson, L. Morales-Inostroza, C. Li, R. Ritika, M. A. P. Nguyen, J. Loyola-Echeverria, S. Kim, S. Götzinger, M. Toth, I. Aharonovich, *Adv. Opt. Mater.* **2020**, *9*, 2001271.
- [156] H. Liu, J. Meng, X. Zhang, Y. Chen, Z. Yin, D. Wang, Y. Wang, J. You, M. Gao, P. Jin, *Nanoscale* **2018**, *10*, 5559.
- [157] Y. Lu, *Two-Dimensional Materials in Nanophotonics: Developments, Devices, and Applications*, CRC Press, Boca Raton, FL, USA **2019**.
- [158] A. Zunger, A. Katzir, A. Halperin, *Phys. Rev. B* **1976**, *13*, 5560.
- [159] T. Vuong, G. Cassabois, P. Valvin, E. Rousseau, A. Summerfield, C. Mellor, Y. Cho, T. Cheng, J. D. Albar, L. Eaves, *2D Mater.* **2017**, *4*, 021023.
- [160] J. Li, S. Majety, R. Dahal, W. P. Zhao, J. Y. Lin, H. X. Jiang, *Appl. Phys. Lett.* **2012**, *101*, 171112.
- [161] X. Li, S. Sundaram, Y. El Gmili, T. Ayari, R. Puybaret, G. Patriarche, P. L. Voss, J. P. Salvestrini, A. Ougazzaden, *Cryst. Growth Des.* **2016**, *16*, 3409.
- [162] R. Beiranvand, S. Valedbagi, *Diamond Relat. Mater.* **2015**, *58*, 190.
- [163] G. Cassabois, A. Rousseau, C. Elias, T. Pelini, P. Vuong, P. Valvin, B. Gil, *C. R. Phys.* **2021**, *22*, 69.
- [164] A. M. Satawara, G. A. Shaikh, S. K. Gupta, P. Gajjar, *Mater. Today: Proc.* **2021**, *47*, 529.
- [165] B. Huang, X. Cao, H. Jiang, J. Lin, S.-H. Wei, *Phys. Rev. B* **2012**, *86*, 155202.
- [166] D. Li, W. Gao, X. Sun, H. Yu, C. Liu, H. Yin, *Adv. Opt. Mater.* **2021**, *9*, 2100342.

- [167] M. Gao, J. Meng, Y. Chen, S. Ye, Y. Wang, C. Ding, Y. Li, Z. Yin, X. Zeng, J. You, *J. Mater. Chem. C* **2019**, *7*, 14999.
- [168] X. Chen, H. Sun, W. Zhang, C. Tan, X. Liu, J. Zhao, L. Hou, Y. Gao, J. Song, Z. Chen, *Vacuum* **2022**, *199*, 110935.
- [169] J. Chen, G. Wang, J. Meng, Y. Cheng, Z. Yin, Y. Tian, J. Huang, S. Zhang, J. Wu, X. Zhang, *ACS Appl. Mater. Interfaces* **2022**, *14*, 7004.
- [170] Y. Wang, J. Meng, Y. Tian, Y. Chen, G. Wang, Z. Yin, P. Jin, J. You, J. Wu, X. Zhang, *ACS Appl. Mater. Interfaces* **2020**, *12*, 27361.
- [171] B. Tan, Y. Wu, F. Gao, H. Yang, Y. Hu, H. Shang, X. Zhang, J. Zhang, Z. Li, Y. Fu, *ACS Appl. Mater. Interfaces* **2022**, *14*, 16453.
- [172] X. Zhu, L. Chen, X. Tang, H. Wang, Y. Xiao, W. Gao, H. Yin, *Appl. Phys. Lett.* **2022**, *120*.
- [173] E. Österlund, J. Kinnunen, V. Rontu, A. Torkkeli, M. Paulasto-Kröckel, *J. Alloys Compd.* **2019**, *772*, 306.
- [174] L. Song, L. Ci, H. Lu, P. B. Sorokin, C. Jin, J. Ni, A. G. Kvashnin, D. G. Kvashnin, J. Lou, B. I. Yakobson, *Nano Lett.* **2010**, *10*, 3209.
- [175] S. Veeralingam, L. Durai, P. Yadav, S. Badhulika, *ACS Appl. Electron. Mater.* **2021**, *3*, 1162.
- [176] X. Li, M. B. Jordan, T. Ayari, S. Sundaram, Y. El Gmili, S. Alam, M. Alam, G. Patriarche, P. L. Voss, J. Paul Salvestrini, *Sci. Rep.* **2017**, *7*, 786.
- [177] W. Zheng, R. Lin, Z. Zhang, F. Huang, *ACS Appl. Mater. Interfaces* **2018**, *10*, 27116.
- [178] W. Zheng, R. Lin, L. Jia, F. Huang, *ACS Photonics* **2019**, *6*, 1869.
- [179] Y. Li, Z. Lin, W. Zheng, F. Huang, *ACS Appl. Electron. Mater.* **2021**, *3*, 3774.
- [180] T. Low, A. Chaves, J. D. Caldwell, A. Kumar, N. X. Fang, P. Avouris, T. F. Heinz, F. Guinea, L. Martin-Moreno, F. Koppens, *Nat. Mater.* **2017**, *16*, 182.
- [181] J. D. Caldwell, L. Lindsay, V. Giannini, I. Vurgaftman, T. L. Reinecke, S. A. Maier, O. J. Glembocki, *Nanophotonics* **2015**, *4*, 44.
- [182] A. J. Giles, S. Dai, I. Vurgaftman, T. Hoffman, S. Liu, L. Lindsay, C. T. Ellis, N. Assefa, I. Chatzakis, T. L. Reinecke, *Nat. Mater.* **2018**, *17*, 134.
- [183] S. Dai, Z. Fei, Q. Ma, A. Rodin, M. Wagner, A. McLeod, M. Liu, W. Gannett, W. Regan, K. Watanabe, *Science* **2014**, *343*, 1125.
- [184] J. D. Caldwell, A. V. Kretinin, Y. Chen, V. Giannini, M. M. Fogler, Y. Francescato, C. T. Ellis, J. G. Tischler, C. R. Woods, A. J. Giles, *Nat. Commun.* **2014**, *5*, 5221.
- [185] A. J. Giles, S. Dai, O. J. Glembocki, A. V. Kretinin, Z. Sun, C. T. Ellis, J. G. Tischler, T. Taniguchi, K. Watanabe, M. M. Fogler, *Nano Lett.* **2016**, *16*, 3858.
- [186] I.-H. Lee, M. He, X. Zhang, Y. Luo, S. Liu, J. H. Edgar, K. Wang, P. Avouris, T. Low, J. D. Caldwell, *Nat. Commun.* **2020**, *11*, 3649.
- [187] P. Li, M. Lewin, A. V. Kretinin, J. D. Caldwell, K. S. Novoselov, T. Taniguchi, K. Watanabe, F. Gaussmann, T. Taubner, *Nat. Commun.* **2015**, *6*, 7507.
- [188] S. Dai, Q. Ma, T. Andersen, A. Mcleod, Z. Fei, M. Liu, M. Wagner, K. Watanabe, T. Taniguchi, M. Thiemens, *Nat. Commun.* **2015**, *6*, 6963.
- [189] P. Li, I. Dolado, F. J. Alfaro-Mozaz, F. Casanova, L. E. Hueso, S. Liu, J. H. Edgar, A. Y. Nikitin, S. Vélez, R. Hillenbrand, *Science* **2018**, *359*, 892.
- [190] T. G. Folland, A. Fali, S. T. White, J. R. Matson, S. Liu, N. A. Aghamiri, J. H. Edgar, R. F. Haglund, Y. Abate, J. D. Caldwell, *Nat. Commun.* **2018**, *9*, 4371.
- [191] P. Li, I. Dolado, F. J. Alfaro-Mozaz, R. Esteban, A. Atxabal, F. Casanova, L. E. Hueso, P. Alonso-González, J. Aizpurua, A. Y. Nikitin, *Light: Sci. Appl.* **2018**, *7*, 17172.
- [192] A. D. Dunkelberger, C. T. Ellis, D. C. Ratchford, A. J. Giles, M. Kim, C. S. Kim, B. T. Spann, I. Vurgaftman, J. G. Tischler, J. P. Long, *Nat. Photonics* **2018**, *12*, 50.
- [193] B. T. Spann, R. Compton, D. Ratchford, J. P. Long, A. D. Dunkelberger, P. B. Klein, A. J. Giles, J. D. Caldwell, J. C. Owrusky, *Phys. Rev. B* **2016**, *93*, 085205.
- [194] S. Dai, Q. Ma, M. Liu, T. Andersen, Z. Fei, M. Goldflam, M. Wagner, K. Watanabe, T. Taniguchi, M. Thiemens, *Nat. Nanotechnol.* **2015**, *10*, 682.
- [195] J. D. Caldwell, I. Vurgaftman, J. G. Tischler, O. J. Glembocki, J. C. Owrusky, T. L. Reinecke, *Nat. Nanotechnol.* **2016**, *11*, 9.
- [196] S. M. Sze, Y. Li, K. K. Ng, *Physics of Semiconductor Devices*, John Wiley & Sons, New York **2021**.
- [197] D. J. Frank, R. H. Dennard, E. Nowak, P. M. Solomon, Y. Taur, W. Hon-Sum Philip, *Proc. IEEE* **2001**, *89*, 259.
- [198] C. R. Dean, A. F. Young, I. Meric, C. Lee, L. Wang, S. Sorgenfrei, K. Watanabe, T. Taniguchi, P. Kim, K. L. Shepard, J. Hone, *Nat. Nanotechnol.* **2010**, *5*, 722.
- [199] J. S. Ross, P. Klement, A. M. Jones, N. J. Ghimire, J. Yan, D. G. Mandrus, T. Taniguchi, K. Watanabe, K. Kitamura, W. Yao, D. H. Cobden, X. Xu, *Nat. Nanotechnol.* **2014**, *9*, 268.
- [200] G. Nazir, M. A. Rehman, M. F. Khan, G. Dastgeer, S. Aftab, A. M. Afzal, Y. Seo, J. Eom, *ACS Appl. Mater. Interfaces* **2018**, *10*, 32501.
- [201] D. Liu, X. Chen, Y. Yan, Z. Zhang, Z. Jin, K. Yi, C. Zhang, Y. Zheng, Y. Wang, J. Yang, X. Xu, J. Chen, Y. Lu, D. Wei, A. T. S. Wee, D. Wei, *Nat. Commun.* **2019**, *10*, 1188.
- [202] W. Liao, L. Huang, *Phys. Status Solidi RRL* **2021**, *15*, 2100276.
- [203] H. N. Jaiswal, M. Liu, S. Shahi, S. Wei, J. Lee, A. Chakravarty, Y. Guo, R. Wang, J. M. Lee, C. Chang, Y. Fu, R. Dixit, X. Liu, C. Yang, F. Yao, H. Li, *Adv. Mater.* **2020**, *32*, 2002716.
- [204] N. A. N. Phan, H. Noh, J. Kim, Y. Kim, H. Kim, D. Whang, N. Aoki, K. Watanabe, T. Taniguchi, G.-H. Kim, *Small* **2022**, *18*, 2105753.
- [205] *International Roadmap for Devices and Systems (IRDS)*, IEEE, Piscataway, NJ, USA **2021**.
- [206] J.-S. Yoon, T. Rim, J. Kim, M. Meyyappan, C.-K. Baek, Y.-H. Jeong, *Appl. Phys. Lett.* **2014**, *105*, 102105.
- [207] D. Nagy, G. Indalecio, A. J. García-Loureiro, M. A. Elmessary, K. Kalna, N. Seoane, *IEEE J. Electron Devices Soc.* **2018**, *6*, 332.
- [208] Q. Zhang, H. Yin, L. Meng, J. Yao, J. Li, G. Wang, Y. Li, Z. Wu, W. Xiong, H. Yang, H. Tu, J. Li, C. Zhao, W. Wang, T. Ye, *IEEE Electron Device Lett.* **2018**, *39*, 464.
- [209] P. Dasika, D. Samantaray, K. Murali, N. Abraham, K. Watanabe, T. Taniguchi, N. Ravishankar, K. Majumdar, *Adv. Funct. Mater.* **2021**, *31*, 2006278.
- [210] K. J. Kuhn, *IEEE Trans. Electron Devices* **2012**, *59*, 1813.
- [211] A. M. Ionescu, H. Riel, *Nature* **2011**, *479*, 329.
- [212] H. Lu, A. Seabaugh, *IEEE J. Electron Devices Soc.* **2014**, *2*, 44.
- [213] L. Britnell, R. V. Gorbachev, R. Jalil, B. D. Belle, F. Schedin, M. I. Katsnelson, L. Eaves, S. V. Morozov, A. S. Mayorov, N. M. R. Peres, A. H. Castro Neto, J. Leist, A. K. Geim, L. A. Ponomarenko, K. S. Novoselov, *Nano Lett.* **2012**, *12*, 1707.
- [214] L. Britnell, R. V. Gorbachev, R. Jalil, B. D. Belle, F. Schedin, A. Mishchenko, T. Georgiou, M. I. Katsnelson, L. Eaves, S. V. Morozov, N. M. R. Peres, J. Leist, A. K. Geim, K. S. Novoselov, L. A. Ponomarenko, *Science* **2012**, *335*, 947.
- [215] J.-H. Lee, D. H. Shin, H. Yang, N. B. Jeong, D.-H. Park, K. Watanabe, T. Taniguchi, E. Kim, S. W. Lee, S. H. Jhang, B. H. Park, Y. Kuk, H.-J. Chung, *Nat. Commun.* **2021**, *12*, 1000.
- [216] J. Xue, J. Sanchez-Yamagishi, D. Bulmash, P. Jacquod, A. Deshpande, K. Watanabe, T. Taniguchi, P. Jarillo-Herrero, B. J. LeRoy, *Nat. Mater.* **2011**, *10*, 282.
- [217] D. Kahng, *IEEE Trans. Electron Devices* **1976**, *23*, 655.
- [218] L. Wu, A. Wang, J. Shi, J. Yan, Z. Zhou, C. Bian, J. Ma, R. Ma, H. Liu, J. Chen, Y. Huang, W. Zhou, L. Bao, M. Ouyang, S. J. Pennycook, S. T. Pantelides, H.-J. Gao, *Nat. Nanotechnol.* **2021**, *16*, 882.

- [219] L. Liu, C. Liu, L. Jiang, J. Li, Y. Ding, S. Wang, Y.-G. Jiang, Y.-B. Sun, J. Wang, S. Chen, D. W. Zhang, P. Zhou, *Nat. Nanotechnol.* **2021**, 16, 874.
- [220] T. Oku, E. Kawakami, M. Uekubo, K. Takahiro, S. Yamaguchi, M. Murakami, *Appl. Surf. Sci.* **1996**, 99, 265.
- [221] K. H. Min, K. C. Chun, K. B. Kim, *J. Vac. Sci. Technol., B: Microelectron. Nanometer Struct.–Process., Meas., Phenom.* **1996**, 14, 3263.
- [222] M. T. Wang, Y. C. Lin, M. C. Chen, *J. Electrochem. Soc.* **1998**, 145, 2538.
- [223] S. S. Roy, M. S. Arnold, *Adv. Funct. Mater.* **2013**, 23, 3638.
- [224] B.-S. Nguyen, J.-F. Lin, D.-C. Perng, *Appl. Phys. Lett.* **2014**, 104, 082105.
- [225] J. H. Bong, S. J. Yoon, A. Yoon, W. S. Hwang, B. J. Cho, *Appl. Phys. Lett.* **2015**, 106, 063112.
- [226] R. Mehta, S. Chugh, Z. Chen, *Nanoscale* **2017**, 9, 1827.
- [227] D. B. Farmer, P. D. Antunez, M. Hopstaken, O. Gunawan, S.-J. Han, *ACS Appl. Nano Mater.* **2018**, 1, 3068.
- [228] M. Ahmed, Y. Li, W. Chen, E.-P. Li, *Nanotechnology* **2022**, 33, 165201.
- [229] W. K. Morrow, S. J. Pearton, F. Ren, *Small* **2016**, 12, 120.
- [230] J. Hong, S. Lee, S. Lee, H. Han, C. Mahata, H.-W. Yeon, B. Koo, S.-I. Kim, T. Nam, K. Byun, B.-W. Min, Y.-W. Kim, H. Kim, Y.-C. Joo, T. Lee, *Nanoscale* **2014**, 6, 7503.
- [231] Y. Zhao, Z. Liu, T. Sun, L. Zhang, W. Jie, X. Wang, Y. Xie, Y. H. Tsang, H. Long, Y. Chai, *ACS Nano* **2014**, 8, 12601.
- [232] L. Shen, Y. Zhao, Y. Wang, R. Song, Q. Yao, S. Chen, Y. Chai, *J. Mater. Chem. A* **2016**, 4, 5044.
- [233] C. L. Lo, K. K. H. Smithe, R. Mehta, S. Chugh, E. Pop, Z. Chen, in *2017 IEEE Int. Reliability Physics Symp. (IRPS)*, IEEE, Piscataway, NJ, USA **2017**, <https://doi.org/10.1109/IRPS.2017.7936379>.
- [234] C. L. Lo, M. Catalano, K. K. H. Smithe, L. Wang, S. Zhang, E. Pop, M. J. Kim, Z. Chen, *npj 2D Mater. Appl.* **2017**, 1, 42.
- [235] M. Ahmed, Y. Li, W. Chen, E. P. Li, *IEEE Access* **2020**, 8, 210542.
- [236] C. L. Lo, B. A. Helfrecht, Y. He, D. M. Guzman, N. Onofrio, S. Zhang, D. Weinstein, A. Strachan, Z. Chen, *J. Appl. Phys.* **2020**, 128, 080903.
- [237] C. L. Lo, M. Catalano, A. Khosravi, W. Ge, Y. Ji, D. Y. Zemlyanov, L. Wang, R. Addou, Y. Liu, R. M. Wallace, M. J. Kim, Z. Chen, *Adv. Mater.* **2019**, 31, 1902397.
- [238] C. Lo, K. Zhang, R. S. Smith, K. Shah, J. A. Robinson, Z. Chen, *IEEE Electron Device Lett.* **2018**, 39, 873.
- [239] B. A. Helfrecht, D. M. Guzman, N. Onofrio, A. H. Strachan, *Phys. Rev. Mater.* **2017**, 1, 034001.
- [240] W. Cao, J. Jiang, X. Xie, A. Pal, J. H. Chu, J. Kang, K. Banerjee, *IEEE Trans. Electron Devices* **2018**, 65, 4109.
- [241] S. King, J. Plombon, J. Bielefeld, J. Blackwell, S. Vyas, R. Chebiam, C. Naylor, D. Michalak, M. Koprinsky, F. Gstrein, M. Metz, J. Clarke, R. Thapa, M. Paquette, V. Vemuri, N. Strandwitz, Y. Fan, M. Orlowski, in *2020 IEEE Int. Electron Devices Meeting (IEDM)*, IEEE, Piscataway, NJ, USA **2020**, <https://doi.org/10.1109/IEDM13553.2020.9371942>.
- [242] F. Ahmed, S. Heo, Z. Yang, F. Ali, C. H. Ra, H.-I. Lee, T. Taniguchi, J. Hone, B. H. Lee, W. J. Yoo, *Adv. Funct. Mater.* **2018**, 28, 1804235.
- [243] S. Hong, C.-S. Lee, M.-H. Lee, Y. Lee, K. Y. Ma, G. Kim, S. I. Yoon, K. Ihm, K.-J. Kim, T. J. Shin, S. W. Kim, E.-C. Jeon, H. Jeon, J.-Y. Kim, H.-I. Lee, Z. Lee, A. Antidormi, S. Roche, M. Chhowalla, H.-J. Shin, H. S. Shin, *Nature* **2020**, 582, 511.
- [244] I. Sungjun, N. Srivastava, K. Banerjee, K. E. Goodson, *IEEE Trans. Electron Devices* **2005**, 52, 2710.
- [245] D. B. Strukov, G. S. Snider, D. R. Stewart, R. S. Williams, *Nature* **2008**, 453, 80.
- [246] J. Borghetti, G. S. Snider, P. J. Kuekes, J. J. Yang, D. R. Stewart, R. S. Williams, *Nature* **2010**, 464, 873.
- [247] J. J. Yang, M. D. Pickett, X. Li, D. A. A. Ohlberg, D. R. Stewart, R. S. Williams, *Nat. Nanotechnol.* **2008**, 3, 429.
- [248] S. Yu, B. Gao, Z. Fang, H. Yu, J. Kang, H. S. P. Wong, *Adv. Mater.* **2013**, 25, 1774.
- [249] B. Govoreanu, G. S. Kar, Y.-Y. Chen, V. Paraschiv, S. Kubicek, A. Fantini, I. P. Radu, L. Goux, S. Clima, R. Degraeve, N. Jossart, O. Richard, T. Vandeweyer, K. K. Seo, P. Hendrickx, G. Pourtois, H. Bender, L. Altimime, D. J. Wouters, J. A. Kittl, M. Jurczak, in *2011 Int. Electron Devices Meeting*, IEEE, Piscataway, NJ, USA **2011**, <https://doi.org/10.1109/IEDM.2011.6131652>.
- [250] M.-J. Lee, C. B. Lee, D. Lee, S. R. Lee, M. Chang, J. H. Hur, Y.-B. Kim, C.-J. Kim, D. H. Seo, S. Seo, U. I. Chung, I.-K. Yoo, K. Kim, *Nat. Mater.* **2011**, 10, 625.
- [251] B. J. Choi, A. C. Torrezan, J. P. Strachan, P. G. Kotula, A. J. Lohn, M. J. Marinella, Z. Li, R. S. Williams, J. J. Yang, *Adv. Funct. Mater.* **2016**, 26, 5290.
- [252] R. Waser, M. Aono, *Nat. Mater.* **2007**, 6, 833.
- [253] S. Goswami, A. J. Matula, S. P. Rath, S. Hedström, S. Saha, M. Annamalai, D. Sengupta, A. Patra, S. Ghosh, H. Jani, S. Sarkar, M. R. Motapothula, C. A. Nijhuis, J. Martin, S. Goswami, V. S. Batista, T. Venkatesan, *Nat. Mater.* **2017**, 16, 1216.
- [254] Y. Ji, C. Pan, M. Zhang, S. Long, X. Lian, F. Miao, F. Hui, Y. Shi, L. Larcher, E. Wu, M. Lanza, *Appl. Phys. Lett.* **2016**, 108, 012905.
- [255] Y. Zuo, H. Lin, J. Guo, Y. Yuan, H. He, Y. Li, Y. Xiao, X. Li, K. Zhu, T. Wang, X. Jing, C. Wen, M. Lanza, *Adv. Electron. Mater.* **2020**, 6, 1901226.
- [256] S. Slesazeck, T. Mikolajick, *Nanotechnology* **2019**, 30, 352003.
- [257] C. Pan, Y. Ji, N. Xiao, F. Hui, K. Tang, Y. Guo, X. Xie, F. M. Puglisi, L. Larcher, E. Miranda, L. Jiang, Y. Shi, I. Valov, P. C. McIntyre, R. Waser, M. Lanza, *Adv. Funct. Mater.* **2017**, 27, 1604811.
- [258] L. Sun, Y. Zhang, G. Han, G. Hwang, J. Jiang, B. Joo, K. Watanabe, T. Taniguchi, Y.-M. Kim, W. J. Yu, B.-S. Kong, R. Zhao, H. Yang, *Nat. Commun.* **2019**, 10, 3161.
- [259] L. Sun, G. Hwang, W. Choi, G. Han, Y. Zhang, J. Jiang, S. Zheng, K. Watanabe, T. Taniguchi, M. Zhao, R. Zhao, Y.-M. Kim, H. Yang, *Nano Energy* **2020**, 69, 104472.
- [260] S. Chen, M. R. Mahmoodi, Y. Shi, C. Mahata, B. Yuan, X. Liang, C. Wen, F. Hui, D. Akinwande, D. B. Strukov, M. Lanza, *Nat. Electron.* **2020**, 3, 638.
- [261] Y. Wang, Z. Huang, X. Chen, M. Lu, *Nanotechnology* **2021**, 33, 125202.
- [262] F. M. Puglisi, L. Larcher, C. Pan, N. Xiao, Y. Shi, F. Hui, M. Lanza, in *2016 IEEE Int. Electron Devices Meeting (IEDM)*, IEEE, Piscataway, NJ, USA **2016**, <https://doi.org/10.1109/IEDM.2016.7838544>.
- [263] C. H. Wang, C. McClellan, Y. Shi, X. Zheng, V. Chen, M. Lanza, E. Pop, H. S. P. Wong, in *2018 IEEE Int. Electron Devices Meeting (IEDM)*, IEEE, Piscataway, NJ, USA **2018**, <https://doi.org/10.1109/IEDM.2018.8614495>.
- [264] H. Zhao, Z. Dong, H. Tian, D. DiMarzi, M.-G. Han, L. Zhang, X. Yan, F. Liu, L. Shen, S.-J. Han, S. Cronin, W. Wu, J. Tice, J. Guo, H. Wang, *Adv. Mater.* **2017**, 29, 1703232.
- [265] Y. Shi, X. Liang, B. Yuan, V. Chen, H. Li, F. Hui, Z. Yu, F. Yuan, E. Pop, H. S. P. Wong, M. Lanza, *Nat. Electron.* **2018**, 1, 458.
- [266] X. Wu, R. Ge, P.-A. Chen, H. Chou, Z. Zhang, Y. Zhang, S. Banerjee, M.-H. Chiang, J. C. Lee, D. Akinwande, *Adv. Mater.* **2019**, 31, 1806790.
- [267] H. Park, M. A. Mastro, M. J. Tadjer, J. Kim, *Adv. Electron. Mater.* **2019**, 5, 1900333.
- [268] K. Zhu, X. Liang, B. Yuan, M. A. Villena, C. Wen, T. Wang, S. Chen, F. Hui, Y. Shi, M. Lanza, *ACS Appl. Mater. Interfaces* **2019**, 11, 37999.
- [269] H. Jeong, J. Kim, D. Y. Kim, J. Kim, S. Moon, O. F. Ngome Okello, S. Lee, H. Hwang, S.-Y. Choi, J. K. Kim, *ACS Appl. Mater. Interfaces* **2020**, 12, 46288.
- [270] R. D. Nikam, K. G. Rajput, H. Hwang, *Small* **2021**, 17, 2006760.
- [271] X. Jing, F. Puglisi, D. Akinwande, M. Lanza, *2D Mater.* **2019**, 6, 035021.
- [272] Y. Shen, W. Zheng, K. Zhu, Y. Xiao, C. Wen, Y. Liu, X. Jing, M. Lanza, *Adv. Mater.* **2021**, 33, 2103656.

- [273] F. Hui, M. A. Villena, W. Fang, A.-Y. Lu, J. Kong, Y. Shi, X. Jing, K. Zhu, M. Lanza, *2D Mater.* **2018**, *5*, 031011.
- [274] J. Ge, H. Huang, Z. Ma, W. Chen, X. Cao, H. Fang, J. Yan, Z. Liu, W. Wang, S. Pan, *Mater. Des.* **2021**, *198*, 109366.
- [275] P. Zhuang, W. Lin, J. Ahn, M. Catalano, H. Chou, A. Roy, M. Quevedo-Lopez, L. Colombo, W. Cai, S. K. Banerjee, *Adv. Electron. Mater.* **2020**, *6*, 1900979.
- [276] K. Qian, R. Y. Tay, V. C. Nguyen, J. Wang, G. Cai, T. Chen, E. H. T. Teo, P. S. Lee, *Adv. Funct. Mater.* **2016**, *26*, 2176.
- [277] J.-Y. Mao, S. Wu, G. Ding, Z.-P. Wang, F.-S. Qian, J.-Q. Yang, Y. Zhou, S.-T. Han, *Small* **2022**, *18*, 2106253.
- [278] C. Pan, E. Miranda, M. A. Villena, N. Xiao, X. Jing, X. Xie, T. Wu, F. Hui, Y. Shi, M. Lanza, *2D Mater.* **2017**, *4*, 025099.
- [279] K. Qian, R. Y. Tay, M.-F. Lin, J. Chen, H. Li, J. Lin, J. Wang, G. Cai, V. C. Nguyen, E. H. T. Teo, T. Chen, P. S. Lee, *ACS Nano* **2017**, *11*, 1712.
- [280] A. Ranjan, N. Raghavan, S. J. O'Shea, S. Mei, M. Bosman, K. Shubhakar, K. L. Pey, *Sci. Rep.* **2018**, *8*, 2854.
- [281] B. Wang, N. Xiao, C. Pan, Y. Shi, F. Hui, X. Jing, K. Zhu, B. Guo, M. A. Villena, E. Miranda, M. Lanza, *Cryst. Res. Technol.* **2018**, *53*, 1800006.
- [282] M. A. Villena, F. Hui, X. Liang, Y. Shi, B. Yuan, X. Jing, K. Zhu, S. Chen, M. Lanza, *Microelectron. Reliab.* **2019**, *102*, 113410.
- [283] X. Hou, R. Pan, Q. Yu, K. Zhang, G. Huang, Y. Mei, D. W. Zhang, P. Zhou, *Small* **2019**, *15*, 1803876.
- [284] Y.-R. Jeon, Y. Abbas, A. S. Sokolov, S. Kim, B. Ku, C. Choi, *ACS Appl. Mater. Interfaces* **2019**, *11*, 23329.
- [285] H. Liang, Q. Abbas, Y. Chen, J. Shi, X. Xia, A. u. Ahmad, *Mater. Sci. Semicond. Process.* **2019**, *103*, 104614.
- [286] W. Lin, P. Zhuang, D. Akinwande, X.-A. Zhang, W. Cai, *Appl. Phys. Lett.* **2019**, *115*, 073101.
- [287] G. Dastgeer, H. Abbas, D. Y. Kim, J. Eom, C. Choi, *Phys. Status Solidi RRL* **2021**, *15*, 2000473.
- [288] P. Kumar, K. Zhu, X. Gao, S.-D. Wang, M. Lanza, C. S. Thakur, *npj 2D Mater. Appl.* **2022**, *6*, 8.
- [289] S. Pi, M. Ghadiri-Sadrabadi, J. C. Bardin, Q. Xia, *Nat. Commun.* **2015**, *6*, 7519.
- [290] M. Kim, R. Ge, X. Wu, X. Lan, J. Tice, J. C. Lee, D. Akinwande, *Nat. Commun.* **2018**, *9*, 2524.
- [291] M. Kim, E. Pallecchi, R. Ge, X. Wu, G. Ducournau, J. C. Lee, H. Happy, D. Akinwande, *Nat. Electron.* **2020**, *3*, 479.
- [292] W. Zhu, S. Park, M. N. Yogeesh, K. M. McNicholas, S. R. Bank, D. Akinwande, *Nano Lett.* **2016**, *16*, 2301.
- [293] A. Sarycheva, A. Polemi, Y. Liu, K. Dandekar, B. Anasori, Y. Gogotsi, *Sci. Adv.* **2018**, *4*, 0920.
- [294] M. Kim, E. Pallecchi, R. Ge, X. Wu, V. Avramovic, E. Okada, J. C. Lee, H. Happy, D. Akinwande, in *2019 IEEE Int. Electron Devices Meeting (IEDM)*, IEEE, Piscataway, NJ, USA **2019**, <https://doi.org/10.1109/IEDM19573.2019.8993470>.
- [295] N. R. Glavin, C. Muratore, M. Snure, *Oxford Open Mater. Sci.* **2020**, *1*, 002.
- [296] M. Saeed, P. Palacios, M.-D. Wei, E. Baskent, C.-Y. Fan, B. Uzlu, K.-T. Wang, A. Hemmetter, Z. Wang, D. Neumaier, M. C. Lemme, R. Negra, *Adv. Mater.* **2022**, 2108473.
- [297] Y. Wu, Y. M. Lin, A. A. Bol, K. A. Jenkins, F. Xia, D. B. Farmer, Y. Zhu, P. Avouris, *Nature* **2011**, *472*, 74.
- [298] L. Liao, Y. C. Lin, M. Bao, R. Cheng, J. Bai, Y. Liu, Y. Qu, K. L. Wang, Y. Huang, X. Duan, *Nature* **2010**, *467*, 305.
- [299] N. Petrone, I. Meric, T. Chari, K. L. Shepard, J. Hone, *IEEE J. Electron Devices Soc.* **2015**, *3*, 44.
- [300] R. Cheng, S. Jiang, Y. Chen, Y. Liu, N. Weiss, H. C. Cheng, H. Wu, Y. Huang, X. Duan, *Nat. Commun.* **2014**, *5*, 5143.
- [301] H. Y. Chang, M. N. Yogeesh, R. Ghosh, A. Rai, A. Sanne, S. Yang, N. Lu, S. K. Banerjee, D. Akinwande, *Adv. Mater.* **2016**, *28*, 1818.
- [302] S. Park, W. Zhu, H. Y. Chang, M. N. Yogeesh, R. Ghosh, S. K. Banerjee, D. Akinwande, in *2015 IEEE Int. Electron Devices Meeting (IEDM)*, IEEE, Piscataway, NJ, USA **2015**, <https://doi.org/10.1109/IEDM.2015.7409812>.
- [303] H. Wang, X. Wang, F. Xia, L. Wang, H. Jiang, Q. Xia, M. L. Chin, M. Dubey, S. J. Han, *Nano Lett.* **2014**, *14*, 6424.



Seokho Moon received his B.S. degree in the Department of Materials Science and Engineering from Pohang University of Science and Technology in 2017. He is currently a Ph.D. candidate at Pohang University of Science and Technology under the supervision of Prof. Jong Kyu Kim. His research interests include the controlled growth of h-BN via metal–organic chemical vapor deposition and its optoelectronics applications.



Jiye Kim received her B.S. degree in material science and engineering from Chungnam National University, South Korea, in 2018. She is currently a Ph.D. candidate in the department of material science and engineering at the Pohang University of Science and Technology under the supervision of Prof. Jong Kyu Kim. Her main research interests include the controlled growth of h-BN via metal–organic chemical vapor deposition and its application in electronics, especially resistive switching memory devices.



Jeonghyeon Park received her B.S. degree in nanotechnology and advanced materials engineering from Sejong University. She is currently a Ph.D. candidate in the department of materials science and engineering at the Pohang University of Science and Technology. Her research interest is GaN-based micro-light-emitting diodes and h-BN-based light emitters.



Semi Im received her B.S. degree in physics from Kyung Hee University. She is currently a Ph.D. candidate in the department of materials science and engineering at Pohang University of Science and Technology (POSTECH) under the supervision of Prof. Jong Kyu Kim. Her research interest is light emitters based on 2D materials, especially h-BN light emitters and h-BN single-photon emitters.



Jawon Kim received her B.S. degree in physics from Gwangju Institute of Science and Technology. She is now a Ph.D. candidate in the Department of Materials Science and Engineering at Pohang University of Science and Technology with Prof. Jong Kyu Kim as a supervisor. Her research interests are focused on optoelectronics based on 2D materials, especially h-BN DUV photodetectors and h-BN light emitters.



Inyong Hwang received his B.S. degree in the Department of Electronic Materials Engineering at Kwangwoon University. He is currently a Ph.D. candidate in the Department of Materials Science and Engineering at Pohang University of Science and Technology. His research interests are focused on the growth of hexagonal boron nitride and its electronic applications.



Jong Kyu Kim received his Ph.D. degree in the Department of Materials Science and Engineering from Pohang University of Science and Technology in 2002. After postdoctoral study and a position as a research assistant professor at Rensselaer Polytechnic Institute until 2009, he became a professor at Pohang University of Science and Technology. His research currently focuses on the synthesis of h-BN by metal–organic chemical vapor deposition, and photonics and electronics applications of h-BN.